

# Introduction to stochastic geometry

Bruno Figliuzzi

February 12, 2026



# Contents

<b>1</b>	<b>Morphological models</b>	<b>1</b>
1.1	Introduction . . . . .	1
1.2	Basic facts from mathematical morphology . . . . .	2
1.2.1	Dilation and erosion . . . . .	2
1.2.2	Opening and closing . . . . .	5
1.2.3	Granulometry . . . . .	7
1.3	Probabilistic approach and Choquet capacity . . . . .	8
1.3.1	Covariance . . . . .	9
1.4	Measurements on random sets . . . . .	14
1.4.1	Minkowski functionals and intrinsic volumes . . . . .	15
1.4.2	Steiner formulae . . . . .	17
1.4.3	Stereology and Crofton formulae . . . . .	18
1.5	Point processes . . . . .	19
1.5.1	General theory . . . . .	19
1.5.2	Poisson point process . . . . .	23
1.5.3	Marked point processes . . . . .	29
1.6	Germ-grain processes . . . . .	31
1.6.1	Definition and first properties . . . . .	31
1.6.2	Practical implementation . . . . .	36
1.6.3	Statistical analysis for the Boolean model . . . . .	37
1.6.4	Notes . . . . .	42
1.7	Random Tessellations . . . . .	42
1.7.1	General introduction . . . . .	43
1.7.2	Poisson tessellation models . . . . .	46
1.7.3	Poisson-Voronoi tessellations . . . . .	48

<b>2 Morphological models in materials science</b>	<b>51</b>
2.1 Microstructure modelling with morphological models . . . . .	52
2.1.1 Context . . . . .	52
2.1.2 Experimental data . . . . .	53
2.1.3 Morphological model . . . . .	55
2.1.4 Results and discussions . . . . .	57
2.1.5 Conclusion . . . . .	59
2.2 Parameters estimation in morphological models . . . . .	60
2.2.1 Problem statement . . . . .	61
2.2.2 Bayesian formulation . . . . .	62
2.2.3 Sampling from the posterior distribution . . . . .	63
2.2.4 Numerical experiments . . . . .	65
2.2.5 Conclusion . . . . .	73
2.3 Eikonal based tessellations . . . . .	74
2.3.1 Eikonal equation . . . . .	74
2.3.2 Fast marching algorithm . . . . .	75
2.3.3 Applications . . . . .	76
2.3.4 Conclusion . . . . .	80
<b>3 Image segmentation</b>	<b>81</b>
3.1 Eikonal-based superpixels . . . . .	82
3.1.1 Algorithm . . . . .	83
3.1.2 Experiments and discussion . . . . .	88
3.1.3 Conclusion . . . . .	93
3.2 Eikonal-based region merging . . . . .	94
3.2.1 Eikonal equation on an undirected graph . . . . .	94
3.2.2 Application to superpixels merging . . . . .	98
3.2.3 Results and discussion . . . . .	100
3.2.4 Conclusion . . . . .	104

# Chapter 1

## Morphological models

### 1.1 Introduction

The study of heterogeneous materials, ranging from porous media and composite structures to polycrystalline aggregates, relies heavily on understanding their complex internal microstructures. These microstructures, often characterized by intricate spatial arrangements of phases, grains, or inclusions, play a pivotal role in determining the macroscopic physical properties of materials. However, the sheer complexity and variability of real-world microstructures pose significant challenges for their direct analysis and simulation.

To address these challenges, morphological models provide a robust mathematical framework for describing, analyzing, and simulating the geometry of heterogeneous media. Rooted in stochastic geometry and mathematical morphology, these models offer a powerful toolkit for capturing the essential features of microstructures, such as connectivity, size distribution, and spatial correlations, while accounting for their inherent randomness.

This chapter explores the foundational concepts of morphological models, with a focus on their application to materials science. We begin by introducing the core principles of mathematical morphology, including dilation, erosion, opening, and closing operations, which serve as the building blocks for analyzing geometric structures. We then extend these concepts to a probabilistic framework, where random sets and point processes enable the modeling of microstructures as stochastic realizations. Special attention is given to germ-grain models, such as the Boolean model, and random tessel-

lations, including Voronoi and Johnson-Mehl tessellations, which are widely used to simulate realistic material microstructures.

Beyond theoretical developments, this chapter also addresses practical aspects of morphological modeling, such as parameter estimation and statistical analysis. We discuss methods for inferring model parameters from experimental data, including the use of covariance functions, granulometries, and stereological techniques. These tools are essential for bridging the gap between theoretical models and real-world applications, enabling the generation of synthetic microstructures that faithfully reproduce the geometric characteristics of observed materials.

## 1.2 Basic facts from mathematical morphology

Mathematical morphology is a theory for the analysis and processing of geometrical structures. It is most commonly applied to digital images, but it can be employed as well on graphs, surface meshes, solids, and many other spatial structures. Random sets theory makes an extensive use of the concepts of mathematical morphology. It is therefore natural to start this introduction with some concepts of mathematical morphology.

### 1.2.1 Dilation and erosion

The basic idea behind mathematical morphology is to analyze a set  $A$  of some topological space  $E$  by probing it with a compact set  $K$  referred to as structuring element. Hence, mathematical morphology makes extensive use of classical operators of set theory, including for instance union or intersection. We first introduce the two basics bricks of mathematical morphology, namely erosion and dilation.

**Definition 1.2.1.** *Let  $A$  be a closed set in  $E$ . The dilated of the set  $A$  by the structuring element  $K$  is the set*

$$D^K(A) = \{x \in E | K_x \cap A \neq \emptyset\}, \quad (1.1)$$

*where  $K_x$  is the translated of the compact  $K$  at  $x \in E$ . Similarly, the eroded of the set  $A$  by the structuring element  $K$  is the set*

$$E^K(A) = \{x \in E | K_x \subset A\}. \quad (1.2)$$

Dilation and erosion are dual operators with respect to the complement, in the sense that dilating the set  $A$  by the structuring element  $K$  is equivalent to erode  $A^c$  by  $K$ .

We assume now that  $E$  is the euclidean space  $\mathbb{R}^d$  of dimension  $d$ . The vectorial space structure of  $\mathbb{R}^d$  allows us to define new operations on  $\mathcal{P}(\mathbb{R}^d)$ , namely the Minkowski addition and subtraction.

**Definition 1.2.2.** *Let  $A$  and  $B$  be subsets of  $\mathbb{R}^d$ . The Minkowski addition is defined by*

$$A \oplus B = \{a + b, a \in A, b \in B\}. \quad (1.3)$$

The Minkowski addition is an associative and commutative operation. Note that  $(\mathcal{P}(\mathbb{R}^d), \oplus)$  is an abelian semi-group, whose neutral element is  $\{0\}$ .

We introduce some notations at this point. Let  $x$  be a point of  $\mathbb{R}^d$ . We denote by  $A_x$  the set  $A$  translated at point  $x$ :

$$A_x = A \oplus \{x\}. \quad (1.4)$$

Similarly, we denote by  $\check{B}$  the symmetric set of  $B \in \mathcal{P}(E)$  defined by

$$\check{B} = \{-x, x \in B\}. \quad (1.5)$$

**Definition 1.2.3.** *Using these notations, we can define the Minkowski subtraction by duality. Let  $A$  and  $B$  be subsets of  $E$ . The Minkowski subtraction is defined by*

$$A \ominus B = (A^c \oplus B)^c = \cap_{x \in B} A_x. \quad (1.6)$$

We can also express the classical dilation and erosion operators of mathematical morphology as functions of the Minkowski addition and subtraction respectively.

**Definition 1.2.4.** *Let  $A$  and  $B$  be subsets of  $\mathbb{R}^d$ . The erosion of  $A$  by  $B$  yields the set*

$$\{x \in E, B_x \in A\} = A \ominus \check{B}. \quad (1.7)$$

*Similarly, we can check by duality that the dilation of  $A$  by  $B$  yields the set*

$$\{x \in E, B_x \cap A \neq \emptyset\} = A \oplus \check{B}. \quad (1.8)$$

**Proposition 1.2.1.** *Let  $A, B \in \mathcal{P}(\mathbb{R}^d)$  be subsets of  $\mathbb{R}^d$ , and  $K, K_1, K_2$  be compact sets of  $\mathcal{K}(\mathbb{R}^d)$ . Then, we have*

$$(A \ominus \check{K}_1) \ominus \check{K}_2 = A \ominus (\check{K}_1 \oplus \check{K}_2), \quad (1.9)$$

$$(A \cap B) \ominus \check{K} = (A \ominus \check{K}) \cap (B \ominus \check{K}), \quad (1.10)$$

and

$$A \oplus (\check{K}_1 \cup \check{K}_2) = (A \oplus \check{K}_1) \cup (A \oplus \check{K}_2). \quad (1.11)$$

*Proof.* To prove (1.9), we first note that, by definition,

$$A \ominus \check{K}_1 = (A^c \oplus \check{K}_1)^c$$

using the definition of the Minkowski subtraction. Therefore, we have:

$$\begin{aligned} (A \ominus \check{K}_1) \ominus \check{K}_2 &= (A^c \oplus \check{K}_1)^c \ominus \check{K}_2 \\ &= ((A^c \oplus \check{K}_1) \oplus \check{K}_2)^c \quad (\text{def. of Minkowski subtraction}) \\ &= (A^c \oplus (\check{K}_1 \oplus \check{K}_2))^c \quad (\text{associativity of Minkowski addition}) \\ &= A \ominus (\check{K}_1 \oplus \check{K}_2) \quad (\text{def. of Minkowski subtraction}) \end{aligned}$$

The relations (1.10) and (1.11) follow immediately from the definition of Minkowski addition and subtraction.  $\square$

**Proposition 1.2.2** (Minkowski operations and convexity). *Let  $A \in \mathcal{P}(\mathbb{R}^d)$  be a subset of  $\mathbb{R}^d$ , and  $K$  be a compact set of  $\mathcal{K}(\mathbb{R}^d)$ . Then :*

1. *If  $A$  is convex, then  $A \ominus \check{K}$  is convex.*
2. *If  $A$  is convex and  $K$  is convex, then  $A \oplus \check{K}$  is convex.*

*In other words, Minkowski subtraction preserves convexity for any compact  $K$  and Minkowski addition preserves convexity if  $K$  is convex.*

*Proof.* We address each part separately.

1. Convexity of  $A \ominus \check{K}$ : Let  $x_1, x_2 \in A \ominus \check{K}$  and  $\lambda \in [0, 1]$ . We want to show that

$$x_\lambda := \lambda x_1 + (1 - \lambda)x_2 \in A \ominus \check{K}.$$

By definition of Minkowski subtraction, for all  $k \in \check{K}$  we have

$$x_1 + k \in A, \quad x_2 + k \in A.$$

Since  $A$  is convex, it follows that

$$\lambda(x_1 + k) + (1 - \lambda)(x_2 + k) = (\lambda x_1 + (1 - \lambda)x_2) + k = x_\lambda + k \in A.$$

As this holds for all  $k \in \check{K}$ , we conclude that

$$x_\lambda \in A \ominus \check{K}.$$

Hence,  $A \ominus \check{K}$  is convex.

## 2. Convexity of $A \oplus \check{K}$ :

Recall the definition of Minkowski addition:

$$A \oplus \check{K} = \{a + k : a \in A, k \in \check{K}\}.$$

Let  $a_1 + k_1, a_2 + k_2 \in A \oplus \check{K}$  and  $\lambda \in [0, 1]$ . Consider the convex combination:

$$\lambda(a_1 + k_1) + (1 - \lambda)(a_2 + k_2) = (\lambda a_1 + (1 - \lambda)a_2) + (\lambda k_1 + (1 - \lambda)k_2).$$

Since  $A$  is convex, we have  $\lambda a_1 + (1 - \lambda)a_2 \in A$ . Thus, the convex combination belongs to  $A \oplus \check{K}$  if and only if

$$\lambda k_1 + (1 - \lambda)k_2 \in \check{K}.$$

In other words,  $A \oplus \check{K}$  is convex if  $\check{K}$  itself is convex.

□

### 1.2.2 Opening and closing

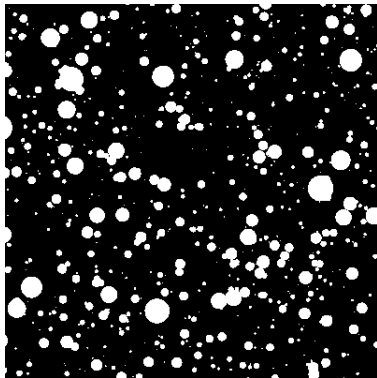
By combining erosion and dilation, we can define two new morphological operators. Let  $A, B \in \mathcal{P}(E)$  be subsets of  $E$ . The *closing*  $A^B$  and the *opening*  $A_B$  of the set  $A$  by  $B$  are defined as follows:

$$A^B = (A \oplus \check{B}) \ominus B, \quad (1.12)$$

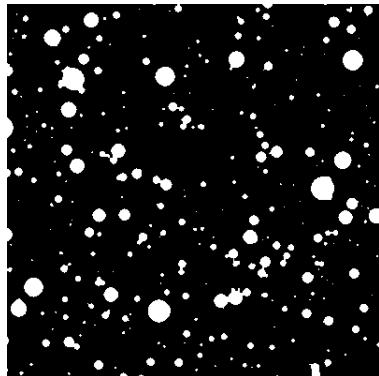
and

$$A_B = (A \ominus \check{B}) \oplus B. \quad (1.13)$$

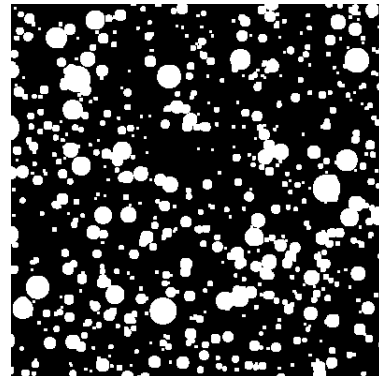
The opening and closing operators are widely used in mathematical morphology. These operator can for instance be used to perform image denoising and are the fundamental bricks upon which builds most of the theory.



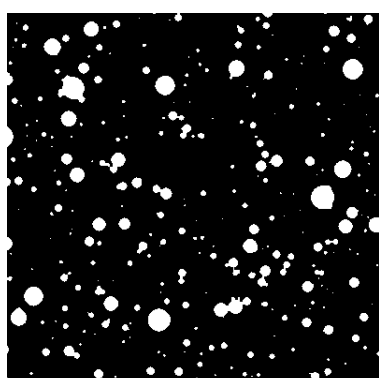
(a) Segmented microstructure simulated with VtkSim [Faessel and Jeulin, 2011].



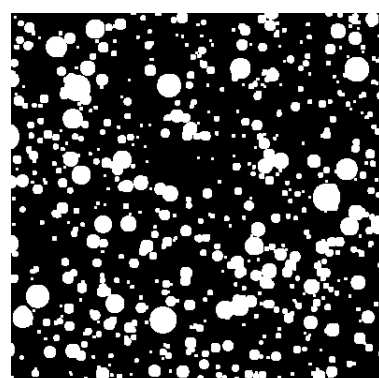
(b) Erosion



(c) Dilation



(d) Opening



(e) Closing

Figure 1.1: Morphological operations applied to a segmented microstructure using a disk of radius one pixel. Erosion removes the smallest components, while dilation expands them.

### 1.2.3 Granulometry

A first application of openings and closings related to the description of random sets are the granulometry operators. Intuitively, a granulometry by closing (resp. by opening) is a family of closings (resp. openings) of increasing sizes, which allows us to characterize the size distribution of the connected components of any random set.

**Definition 1.2.5.** *More formally, a granulometry is a family of set operators  $\Phi_\lambda$  depending on a positive parameter  $\lambda$  satisfying the following properties:*

- For all  $A$  in  $\mathcal{F}(E)$ ,  $\Phi_\lambda(A) \subset A$ :  $\Phi_\lambda$  is anti-extensive.
- If  $A \subset B$ , then  $\Phi_\lambda(A) \subset \Phi_\lambda(B)$ :  $\Phi_\lambda$  is increasing.
- $\Phi_\lambda \circ \Phi_\mu = \Phi_\mu \circ \Phi_\lambda = \Phi_{\max(\mu,\lambda)}$

The axiomatic of granulometries was first formulated in [Matheron, 1975]. Note that an immediate consequence of the last point of the definition is that  $\Phi_\lambda$  is necessarily an idempotent operator, in the sense that  $\Phi_\lambda \circ \Phi_\lambda = \Phi_\lambda$ .

As stated above, the axiomatic of granulometries remains very general. In practice, we will often consider granulometries relying on a family of openings. Let  $K$  be a convex set. We consider the family  $\{K_\lambda, \lambda > 0\}$ , where  $K_\lambda = \lambda K$ . The operator

$$\Phi_\lambda(A) = (A \ominus \check{K}_\lambda) \oplus K_\lambda, \quad (1.14)$$

defined for all closed set  $A$  of  $\mathcal{F}(E)$ , is a granulometry. For a random set  $A$ , a granulometry by openings describes the size distribution of the elements of  $A$  by opening by convex sets.

In a similar manner, we can define a granulometry by closing. To that end, we consider the operator

$$\Phi_\lambda(A) = (A \oplus \check{K}_\lambda) \ominus K_\lambda, \quad (1.15)$$

defined for all closed set  $A$  of  $\mathcal{F}(E)$ . A granulometry by closing describes the size distribution of the elements of  $A$  by closing by convex sets.

### 1.3 Probabilistic approach and Choquet capacity

Concepts of mathematical morphology prove very convenient to study random sets. In particular, it is of interest to translate some compact set  $K$  in an observation window to analyse a random closed set  $A$  of  $\mathbb{R}^n$ . Two elementary events can occur:

- if  $K \cap A = \emptyset$ , the structuring element  $K$  is disjoint from  $A$ ;
- otherwise, if  $K \cap A \neq \emptyset$ , the structuring element  $K$  hits the set  $A$ .

The random closed set  $A$  is completely characterized by the functional  $T(K)$  defined for all compact sets  $K$  by

$$T(K) = P\{A \cap K \neq \emptyset\} = 1 - P\{K \cap A^c\} = 1 - Q(K) \quad (1.16)$$

$T(K)$  is called the Choquet capacity of the random closed set  $A$ . Note that the Choquet capacity is closely related to dilation and erosion operators. For all compact set  $K \subset \mathbb{R}^d$ , we have indeed

$$T(K) = P\{K \cap A \neq \emptyset\} = P\{x \in A \oplus \check{K}\} \quad (1.17)$$

**Proposition 1.3.1.** *The Choquet capacity is related to the Minkowski operators by the following equation :*

$$Q(K) = P\{K \subset A^c\} = P\{x \in A^c \ominus \check{K}\}. \quad (1.18)$$

*Proof.* By definition, the functional  $Q(K)$  is the probability that the compact set  $K$  is entirely contained in the complement of  $A$ :

$$Q(K) := P\{K \subset A^c\}.$$

Recall the definition of Minkowski subtraction (erosion) of a set  $B$  by a compact set  $K$ :

$$B \ominus \check{K} := \{x \in \mathbb{R}^d : x + \check{K} \subset B\}.$$

Let us apply this definition with  $B = A^c$ . Then, for any  $x \in \mathbb{R}^d$ ,

$$x \in A^c \ominus \check{K} \iff x + \check{K} \subset A^c.$$

Now, notice that  $\check{K} = \{-k : k \in K\}$ . If we translate  $\check{K}$  by  $x$ , we get

$$x + \check{K} = \{x - k : k \in K\}.$$

Therefore, the event

$$\{x \in A^c \ominus \check{K}\}$$

is exactly the event that “the translated version of  $K$  by  $x$  lies entirely in  $A^c$ ”, which is equivalent (up to translation) to  $K \subset A^c$ . Hence, taking probabilities, we obtain

$$Q(K) = P\{K \subset A^c\} = P\{x \in A^c \ominus \check{K}\}.$$

This shows that the erosion of  $A^c$  by  $\check{K}$  describes exactly the event that  $K$  is contained in  $A^c$ , and thus

$$Q(K) = P\{x \in A^c \ominus \check{K}\}.$$

□

The structuring element  $K$  can be a single point  $\{x\}$  of  $\mathbb{R}^d$  or any compact set of  $\mathbb{R}^d$ . However, we have to insist on the fact that the choice of structuring element is fundamental. Each compact set  $K$  indeed brings its own information on the studied set  $A$ . For instance, if one chooses  $K$  to be a single point, the choquet capacity yields

$$T(\{x\}) = P\{\{x\} \cap A \neq \emptyset\} = P\{x \in A\}, \quad (1.19)$$

which is the *spatial law* of the set  $A$ . Similarly, if one chooses  $K$  to be the set  $\{x, x + h\}$ , the choquet capacity allows to calculate the *covariance* of the random closed set.

$$T(\{x, x + h\}) = P\{x \in A, x + h \in A\}. \quad (1.20)$$

### 1.3.1 Covariance

The covariance is a - if not *the* - fundamental tool to describe spatial arrangement in a random closed set.

**Definition 1.3.1.** *The covariance of a random set  $A \subset \mathbb{R}^d$  is the function  $C_A$  defined on  $\mathbb{R}^d \times \mathbb{R}^d$  by*

$$C_A(x, x + h) = P\{x \in A, x + h \in A\}, \quad (1.21)$$

where  $h$  is some vector of  $\mathbb{R}^d$ .

The covariance of the set  $A$  at a given point  $x$  and for a distance  $h$  is the probability that  $x$  and  $x + h$  both belong to  $A$ . Note that for a stationary random set, the covariance is a function of the distance  $h$  only:

$$C_A(x, x + h) = C_A(h). \quad (1.22)$$

If in addition the set  $A$  is ergodic, meaning that its spatial averages over a single realization are representative of ensemble averages over many realizations, the covariance  $C(h)$  can be estimated from the volume fraction of  $A \cap A_{-h}$  as

$$C_A(h) = P\{x \in A \cap A_{-h}\} = V(A \cap A_{-h}) = V(A \ominus \check{h}), \quad (1.23)$$

where  $h$  is the set  $\{x, x + h\}$ . In practice, this allows the covariance to be computed from a single experimental sample of the random set using equation (1.23), rather than requiring multiple realizations.

The covariance  $C_A$  provides useful information about the spatial arrangement of the random set  $A$ . In particular, it accounts for the presence of several scales in the studied set or for periodicity. Note that by definition,  $C_A(0)$  simply corresponds to the volumic fraction of the set  $A$ . For any orientation, the covariance  $C(h)$  reaches a sill at the distance or range  $h_\infty$ . At this distance, events  $\{x \in A\}$  and  $\{x + h_\infty\}$  are independent and we have

$$C_A(h_\infty) = p^2. \quad (1.24)$$

These considerations enable us to define a normalized version of the covariance that remains between 0 and 1:

$$\gamma(h) = \frac{C(h) - p^2}{p(1 - p)}. \quad (1.25)$$

For an ergodic experimental sample, the covariance can be estimated with relation (1.23). An alternative approach is to use the Fourier transform:

**Proposition 1.3.2.** *Let  $A$  be a subset of  $\mathbb{R}^d$ . Then, the covariance of  $A$  is*

$$C_A(h) = \frac{1}{(2\pi)^n} \int_{\mathbb{R}^n} |\hat{f}(\xi)|^2 \exp(i\xi h) d\xi. \quad (1.26)$$

*Proof.* Let  $A \subset \mathbb{R}^d$  be a random closed set. Define its indicator function

$$f(x) := \mathbf{1}_A(x) = \begin{cases} 1, & x \in A, \\ 0, & x \notin A. \end{cases}$$

By definition, the covariance of  $A$  at a lag  $h$  is

$$C_A(h) = \mathbb{E}[f(x)f(x+h)].$$

Consider the Fourier transform of  $f$ , denoted by

$$\hat{f}(\xi) = \int_{\mathbb{R}^d} f(x)e^{-i\xi \cdot x} dx.$$

Recall the convolution theorem: for two functions  $f$  and  $g$ ,

$$\mathcal{F}[f * g] = \hat{f} \hat{g}, \quad \text{and} \quad f * g(x) = \int_{\mathbb{R}^d} f(y)g(x-y) dy.$$

The covariance can be expressed as a convolution:

$$C_A(h) = \int_{\mathbb{R}^d} f(x)f(x+h) dx = (f * f^\dagger)(h),$$

where  $f^\dagger(x) := f(-x)$  is the reflection of  $f$ . Applying the Fourier transform, we have

$$\mathcal{F}[C_A](\xi) = \mathcal{F}[f * f^\dagger](\xi) = \hat{f}(\xi) \overline{\hat{f}(\xi)} = |\hat{f}(\xi)|^2,$$

where the overline denotes complex conjugation. Finally, applying the inverse Fourier transform gives

$$C_A(h) = \frac{1}{(2\pi)^n} \int_{\mathbb{R}^d} |\hat{f}(\xi)|^2 e^{i\xi \cdot h} d\xi.$$

□

The covariance of a random set  $A$  generally depends on the orientation of the vector  $h$ . The *isotropised covariance* is defined to be

$$\bar{C}(h) = \int_{S_{d-1}} C(h\mathbf{u})U(d\mathbf{u}), \tag{1.27}$$

where  $\mathbf{u}$  is an unitary vector and  $U(d\mathbf{u})$  denotes the uniform distribution on the unit sphere  $S_{d-1}$ .

Some features of the covariance can easily be expressed analytically. A fundamental example is given by its first derivative.

**Proposition 1.3.3.** *Let  $A$  be a random set on  $\mathbb{R}^d$ . Then, the first derivative of the covariance is*

$$\frac{d}{dh}C_A(h\mathbf{u}) = -\lim_{h \rightarrow 0} \nu_{d-1}((K \cap K_{r\mathbf{u}})|_{\mathbf{u}^\perp}), \quad (1.28)$$

where  $\nu_{d-1}$  is the Lebesgue measure on  $\mathbb{R}^{d-1}$  and  $\mathbf{u}$  is some unit vector.  $(K \cap K_{r\mathbf{u}})|_{\mathbf{u}^\perp}$  denotes the projection of  $(K \cap K_{r\mathbf{u}})$  on the hyperplane that has  $\mathbf{u}$  as normal vector.

*Proof.* Let  $A \subset \mathbb{R}^d$  be a random closed set with covariance

$$C_A(h\mathbf{u}) = P\{x \in A, x + h\mathbf{u} \in A\},$$

where  $\mathbf{u}$  is a unit vector in  $\mathbb{R}^d$ . The proof proceeds in four subsequent steps:

1. *Covariance in terms of volume fractions:*

For a compact observation window  $K \subset \mathbb{R}^d$ , the covariance along the direction  $\mathbf{u}$  can be expressed as

$$C_A(h\mathbf{u}) = V(A \cap A_{h\mathbf{u}}),$$

where  $A_{h\mathbf{u}}$  denotes the translation of  $A$  by  $h\mathbf{u}$ . This follows from ergodicity, as in equation (1.23).

2. *Difference quotient:*

The derivative of the covariance in the direction  $\mathbf{u}$  is formally

$$\frac{d}{dh}C_A(h\mathbf{u}) = \lim_{\Delta h \rightarrow 0} \frac{C_A((h + \Delta h)\mathbf{u}) - C_A(h\mathbf{u})}{\Delta h}.$$

Substituting the volume fraction expression, we get

$$\frac{d}{dh}C_A(h\mathbf{u}) = \lim_{\Delta h \rightarrow 0} \frac{V(A \cap A_{(h + \Delta h)\mathbf{u}}) - V(A \cap A_{h\mathbf{u}})}{\Delta h}.$$

3. *Geometric interpretation for  $h \rightarrow 0$ :*

For small  $\Delta h$ , the difference

$$V(A \cap A_{h\mathbf{u}}) - V(A \cap A_{(h + \Delta h)\mathbf{u}})$$

corresponds to the volume of the “boundary layer” of thickness  $\Delta h$  where  $A$  and  $A_{h\mathbf{u}}$  stop overlapping. By classical results in geometric measure theory (Steiner formula and Crofton formula, see section 1.4), this volume is approximately

$$\Delta h \cdot \nu_{d-1}((A \cap A_{h\mathbf{u}})|_{\mathbf{u}^\perp}) + o(\Delta h),$$

where  $\nu_{d-1}$  is the  $(d-1)$ -dimensional Lebesgue measure on the hyperplane orthogonal to  $\mathbf{u}$ , and  $(A \cap A_{h\mathbf{u}})|_{\mathbf{u}^\perp}$  is the orthogonal projection of  $A \cap A_{h\mathbf{u}}$  onto that hyperplane.

#### 4. Taking the limit:

Dividing by  $\Delta h$  and taking the limit  $\Delta h \rightarrow 0$ , we obtain

$$\frac{d}{dh} C_A(h\mathbf{u}) = -\nu_{d-1}((A \cap A_{h\mathbf{u}})|_{\mathbf{u}^\perp}).$$

Finally, evaluating at  $h \rightarrow 0$ , the derivative of the covariance at zero lag is

$$\left. \frac{d}{dh} C_A(h\mathbf{u}) \right|_{h=0} = -\lim_{h \rightarrow 0} \nu_{d-1}((K \cap K_{h\mathbf{u}})|_{\mathbf{u}^\perp}),$$

where  $K$  is the compact observation window. Thus, the first derivative of the covariance along the direction  $\mathbf{u}$  is given by the negative  $(d-1)$ -dimensional measure of the projection of the overlap region onto the hyperplane perpendicular to  $\mathbf{u}$ , which proves equation (1.28).

□

When  $d = 3$ , for the isotropic case, equation (1.28) simply yields

$$\frac{dC_A}{dh}(0) = -S(A), \quad (1.29)$$

where  $S(A)$  is the surface area of the set  $A$  in  $\mathbb{R}^3$ . Similarly, when  $d = 2$ , equation (1.28) yields

$$\frac{dC_A}{dh}(0) = -\mathcal{P}(A), \quad (1.30)$$

where  $\mathcal{P}(A)$  is the length of the perimeter of  $A$  in  $\mathbb{R}^2$ .

## 1.4 Measurements on random sets

Starting from a material image, it is possible to measure a very large number of parameters. It is, however, essential that these parameters be meaningful with respect to the physics and the geometry of the material. Two families of parameters are usually considered, namely *metric* and *topological* parameters. Intuitively, if we consider inclusions embedded in a matrix, one may be interested in the volume fraction of inclusions. This parameter is metric, in the sense that it is obtained directly through measurement. Conversely, one may also be interested in the number of included particles. This parameter is topological, as it is obtained by counting.

In practice, strict limitations are imposed on admissible measurements. First, one generally requires the measurement to be invariant under isometries. This ensures that a measurement performed on a set  $X$  does not depend on its location or orientation in space. A *homogeneity* condition must also be satisfied: if the same set  $X$  is observed at different scales, the measurement should scale accordingly. This condition yields, for a measurement  $W$  that is homogeneous of degree  $k$ ,

$$W(\lambda X) = \lambda^k W(X), \quad (1.31)$$

where  $\lambda > 0$ .

An additional requirement is *additivity*. In mathematical terms, this condition is expressed through the relation

$$W(X) + W(Y) = W(X \cup Y) + W(X \cap Y), \quad (1.32)$$

whenever the union  $X \cup Y$  is admissible. Finally, the measurement should be *continuous*: small deformations of the measured set must not result in large variations of the measured value.

Finite unions of convex sets play a key role in stochastic geometry. Much of the geometric theory of random sets is built upon results obtained for convex sets and their extensions to finite unions of convex sets. A fundamental result states that all measurements satisfying the conditions listed above can be expressed as linear combinations of a finite number of basic functionals, known as Minkowski functionals. We discuss this result in greater depth in the following sections.

### 1.4.1 Minkowski functionals and intrinsic volumes

**Definition 1.4.1.** A subset  $C$  of  $\mathbb{R}^d$  is said to be convex if, for every pair of points  $x, y \in C$  and every  $c \in [0, 1]$ , we have

$$cx + (1 - c)y \in C. \quad (1.33)$$

Affine linear subspaces provide archetypal examples of convex sets. An affine linear subspace  $L$  of dimension  $k$  in  $\mathbb{R}^d$  is a translation of a  $k$ -dimensional linear subspace and can be characterized as the solution set of  $d - k$  independent affine equations. Such subspaces are commonly referred to as *k-flats* or *k-planes*.

**Definition 1.4.2.** A convex body is a compact, convex subset of  $\mathbb{R}^d$ . We denote by  $\mathcal{C}(\mathbb{R}^d)$  the family of all convex bodies in  $\mathbb{R}^d$ .

**Definition 1.4.3.** A convex body functional is a functional  $h$  defined on  $\mathcal{C}(\mathbb{R}^d)$  that assigns a real value  $h(C)$  to each  $C \in \mathcal{C}(\mathbb{R}^d)$ . Such a functional is said to be:

- isometry-invariant if  $h(\mathcal{G}C) = h(C)$  for every isometry  $\mathcal{G}$ ;
- monotone if  $C_1 \subset C_2$  implies  $h(C_1) \leq h(C_2)$ ;
- $C$ -additive if, for all  $C_1, C_2 \in \mathcal{C}(\mathbb{R}^d)$  such that  $C_1 \cup C_2$  is convex, we have

$$h(C_1) + h(C_2) = h(C_1 \cup C_2) + h(C_1 \cap C_2). \quad (1.34)$$

A fundamental theorem of integral geometry states that all convex body functional that are isometry-invariant, monotone and  $C$ -additive can be expressed as linear combinations of the Minkowski functionals  $W_d$ . The Minkowski functionals are isometry-invariant, monotone,  $C$ -additive convex body functionals, defined directly on  $\mathcal{C}(\mathbb{R}^d)$  by the formula

$$W_k(C) = \frac{b_d}{b_{d-k}} \int_{\mathbb{L}_k} \mu_{d-k}(C|_{E^\perp}) U_k(dE). \quad (1.35)$$

In this expression,  $b_k$  denotes the volume of the unit ball in  $\mathbb{R}^k$ .  $\mu_k$  is the  $k$ -dimensional Lebesgue measure.  $\mathbb{L}_k$  is the set of all  $k$ -subspaces,  $C|_{E^\perp}$  is the orthogonal projection of the convex body  $C$  on  $E^\perp$ ,  $E^\perp$  is the  $(d - k)$ -subspace orthogonal to  $E \in \mathbb{L}_k$ , and  $U_k$  is the uniform probability distribution on  $\mathbb{L}_k$ .

$\forall d > 0$ , for  $k = 0$ , equation (1.35) becomes

$$W_0(C) = \int_{\mathbb{L}_0} \mu_d(C|_{E^\perp}) U_0(dE) = \mu_d(C). \quad (1.36)$$

Hence,  $W_0(C)$  is equal to the volume  $\mu_d(C)$ .

Similarly,  $\forall d > 0$ , for  $k = d$ , we find

$$W_d(C) = b_d \quad (1.37)$$

**Theorem 1.4.1** (Hadwiger's characterization theorem). *Every non-negative, isometry-invariant, monotone, and  $C$ -additive convex body functional  $h$  on  $\mathcal{C}(\mathbb{R}^d)$  can be written uniquely as a linear combination of the Minkowski functionals:*

$$h(C) = \sum_{k=0}^d a_k W_k(C), \quad \forall C \in \mathcal{C}(\mathbb{R}^d), \quad (1.38)$$

where the coefficients  $a_k$  are real constants.

In dimensions  $d = 1, 2, 3$ , the Minkowski functionals admit the following explicit interpretations:

$\mathbf{d = 1}$	$W_0(C) = \mathcal{L}(C), \quad W_1(C) = 2$
$\mathbf{d = 2}$	$W_0(C) = \mathcal{A}(C), \quad W_1(C) = \frac{L(C)}{2},$ $W_2(C) = \pi$
$\mathbf{d = 3}$	$W_0(C) = \mathcal{V}(C), \quad W_1(C) = \frac{S(C)}{3},$ $W_2(C) = \frac{M(C)}{3}, \quad W_3(C) = \frac{4\pi}{3},$

Here  $\mathcal{L}(C)$ ,  $\mathcal{A}(C)$ , and  $\mathcal{V}(C)$  denote the length, area, and volume of  $C$  in dimensions 1, 2, and 3, respectively. The quantity  $L(C)$  denotes the boundary length in two dimensions,  $S(C)$  the surface area in three dimensions, and  $M(C)$  the integral of mean curvature, defined by

$$M(C) = \int_{\partial C} m(x), dS, \quad (1.39)$$

where  $m(x)$  is the mean curvature at  $x \in \partial C$ .

Some authors prefer to work with an equivalent family of functionals known as *intrinsic volumes*. The intrinsic volumes  $V_k$ ,  $k = 0, \dots, d$ , are related to the Minkowski functionals by

$$b_{d-k} V_k(C) = \binom{d}{k} W_{d-k}(C). \quad (1.40)$$

In dimensions  $d = 1, 2, 3$ , the intrinsic volumes take the following form:

---

$\mathbf{d = 1}$	$V_0(C) = 1, \quad V_1(C) = \mathcal{L}(C)$
$\mathbf{d = 2}$	$V_0(C) = 1, \quad V_1(C) = \frac{\mathcal{L}(C)}{2},$ $V_2(C) = \mathcal{A}(C)$
$\mathbf{d = 3}$	$V_0(C) = 1, \quad V_1(C) = \frac{\mathcal{M}(C)}{\pi},$ $V_2(C) = \frac{\mathcal{S}(C)}{2}, \quad V_3(C) = \mathcal{V}(C).$

---

### 1.4.2 Steiner formulae

Convex geometry is closely related to mathematical morphology. In particular, Steiner formulae provide a powerful tool for expressing the volume of a convex body dilated by a ball of radius  $r > 0$  in terms of its Minkowski functionals.

**Definition 1.4.4.** Let  $A \subset \mathbb{R}^d$ . The parallel set of  $A$  at distance  $r$  is defined as

$$A_{\oplus r} = A \oplus B(0, r). \quad (1.41)$$

**Theorem 1.4.2** (Steiner formula). Let  $C \in \mathcal{C}(\mathbb{R}^d)$  and  $r > 0$ . Then

$$\mu_d(C \oplus B(0, r)) = \sum_{k=0}^d \binom{d}{k} W_k(C) r^{d-k}. \quad (1.42)$$

Equivalently, in terms of intrinsic volumes,

$$\mu_d(C \oplus B(0, r)) = \sum_{k=0}^d b_{d-k} V_k(C) r^{d-k}. \quad (1.43)$$

### 1.4.3 Stereology and Crofton formulae

In many experimental situations, observations are obtained from images that provide only a two-dimensional representation of an inherently three-dimensional microstructure. This is notably the case in materials science, where micrographs or polished sections reveal planar cuts through a bulk material. As a consequence, one is often required to estimate geometric or topological characteristics defined in  $\mathbb{R}^3$  from measurements performed in  $\mathbb{R}^2$ .

A parameter is said to be *stereological* if it can be inferred from lower-dimensional observations in an unbiased manner, that is, if its expected value can be recovered from measurements performed on sections, projections, or intersections of the structure with lower-dimensional subspaces. Stereology thus provides a rigorous mathematical framework for linking measurements across dimensions.

A cornerstone of stereological theory is given by the Crofton formulae. These results relate intrinsic volumes of a convex body to mean values of intrinsic volumes of its intersections with affine subspaces of complementary dimension. In essence, Crofton formulae express global geometric quantities in terms of averages of simpler measurements performed on lower-dimensional sections.

Let  $C \subset \mathbb{R}^d$  be a convex body, and let  $A(d, k)$  denote the space of all  $k$ -dimensional affine subspaces of  $\mathbb{R}^d$ , endowed with the motion-invariant Haar measure  $\nu_{d,k}$ . For  $k = 0, 1, \dots, d - 1$ , the Crofton formula states that the intrinsic volume  $V_{d-k}(C)$  can be expressed as

$$V_{d-k}(C) = c_{d,k} \int_{A(d,k)} V_0(C \cap E) \nu_{d,k}(dE), \quad (1.44)$$

where  $V_0$  denotes the Euler characteristic and  $c_{d,k}$  is a dimension-dependent normalization constant. In other words, intrinsic volumes can be obtained by averaging topological characteristics of intersections of  $C$  with randomly oriented affine subspaces.

More generally, Crofton-type relations take the form

$$\int_{A(d,k)} V_j(C \cap E) \nu_{d,k}(dE) = c_{d,k,j} V_{j+d-k}(C), \quad (1.45)$$

for suitable constants  $c_{d,k,j}$  and admissible indices  $j$ . These identities show that quantities such as lengths, areas, surface areas, or Euler characteristics

measured on planar sections carry precise quantitative information about the three-dimensional geometry of the object.

In the practically important case  $d = 3$ , many classical stereological relations follow directly from Crofton formulae. For instance, the volume fraction of a phase equals the expected area fraction observed on planar sections, the surface area density is related to the mean boundary length per unit area, and curvature-related quantities can be estimated from intersection counts with test lines or planes. Crofton formulae therefore constitute the theoretical foundation of a large class of stereological estimators used in practice. When combined with assumptions such as stationarity and ergodicity of the underlying random set, they allow intrinsic volumes of random microstructures to be estimated reliably from a finite number of lower-dimensional observations. For comprehensive treatments of stereology and Crofton formulae, we refer the reader to the monographs by Stoyan, Kendall, and Mecke, and by Schneider and Weil.

## 1.5 Point processes

We present in this section the general theory of random point processes. A random point process  $\mathcal{P}$  is a collection of random points. Point processes can be considered as the basic ingredients of stochastic geometry. A particular role is played by Poisson point processes in the  $d$ -dimensional space  $\mathbb{R}^d$ . In section 1.5.1, we introduce a general framework for the study of point processes. We study more specifically Poisson point processes in section 1.5.2. Marked point processes are then discussed in section 1.5.3.

### 1.5.1 General theory

Let us first introduce a general framework for the study of point processes on locally compact topological spaces. The results of this section are technical and we will only state the most relevant ones, often without proof. We refer the reader to the reference textbooks [Schneider and Weil, 2008] and [Chiu et al., 2013] for a more extensive presentation.

#### Random point processes as counting measures

Let  $E$  be a locally compact space with a countable topological basis. We denote by  $\mathcal{B}(E)$  the Borel  $\sigma$ -algebra of  $E$ . Let  $M(E)$  be the set of all locally

finite measures defined on  $E$ . Recall that a measure  $\eta$  is said to be locally finite if for all compact  $C$  in  $\mathcal{K}(E)$ ,  $\eta(C) < \infty$ . For all borelian set  $A$  in  $\mathcal{B}(E)$ , we define the evaluation map

$$\Phi_A : M \rightarrow \mathbb{R} \cup \{\infty\}. \quad (1.46)$$

When equipped with the  $\sigma$ -algebra  $\mathcal{M}$  generated by all evaluation maps  $\{\Phi_A, A \in \mathcal{B}(E)\}$ ,  $M(E)$  forms a measurable space.

A class of measures of particular interest for the study of point processes is provided by the counting measures.

**Definition 1.5.1.** *A counting measure on  $E$  is a measure  $\eta$  in  $M(E)$  such that for all borelian set  $A$  in  $\mathcal{B}(A)$ ,  $\eta(A) \in \mathbb{N} \cup \{\infty\}$ . We denote by  $N(E)$  the set of all counting measures on  $E$ .*

It can be shown that  $N(E)$  is a measurable subset of  $(M(E), \mathcal{M})$  [Schneider and Weil, 2008]. We denote by  $\mathcal{N}$  the corresponding  $\sigma$ -algebra. A fundamental example of counting measure is given by locally finite sums of Dirac measures:

$$\eta = \sum_{k=1}^n \delta_{x_k}. \quad (1.47)$$

Another example is given by random Poisson counting measures. For all borelien set  $A$  of  $\mathbb{R}^d$ , a random Poisson counting measure follows a Poisson distribution given by

$$\eta(A) = \frac{\Theta(A)^k}{k!} \exp(-\Theta(A)), \quad (1.48)$$

where  $\Theta$  is some(real) measure on the  $\sigma$ -algebra  $\mathcal{B}(\mathbb{R}^d)$ .

Point processes can be apprehended either as random sets of discrete points or as random counting measures giving the number of points contained in any domain of  $E$ . For a counting measure  $\eta \in N(E)$ , the support  $\text{supp } \eta$  is the smallest closed set  $A$  in  $E$  such that  $\eta(E/A) = 0$ . The mapping  $\eta \rightarrow \text{supp } \eta$  identifies a random measure to its corresponding point process. As alluded to earlier, the set of all locally finite measures on  $E$  can be equipped with a  $\sigma$ -algebra. This consideration enables us to define a probability law on  $M(E)$ .

**Definition 1.5.2.** A random measure  $X$  on  $E$  is a measurable map from some probability space  $\{\Omega, \mathcal{A}, \mathbb{P}\}$  into the measurable space  $\{M(E), \mathcal{M}\}$ . The image measure  $\mathbb{P}_X$  is the distribution of  $X$ .

For a random measure  $X$  which is almost surely concentrated on  $N(E)$ , since  $N(E)$  is a measurable subset of  $M(E)$ ,  $\text{supp } X$  is a random point process on  $E$ . Its distribution is defined for all  $Y \in \mathcal{N}$  by the probabilities

$$P(Y) = \mathbb{P}\{X \in Y\} = \mathcal{P}\{\omega \in \Omega, X(\omega) \in Y\}. \quad (1.49)$$

The finite-dimensional distributions are of particular interest. They are defined for any family  $\{B_1, B_2, \dots, B_k\}$  of bounded Borel sets of  $E$  to be the probabilities

$$\mathbb{P}\{X(B_1) = n_1, \dots, X(B_k) = n_k\}, \quad (1.50)$$

where  $n_1, \dots, n_k$  are positive integers.

### Intensity measure

From now on, we will assume  $E$  to be the  $d$ -dimensional Euclidean space  $\mathbb{R}^d$ .

**Definition 1.5.3.** The intensity of the random measure  $X$  is the measure on  $\mathbb{R}^d$  defined for all borelian set  $A$  in  $\mathcal{B}(\mathbb{R}^d)$  by

$$\Theta(A) = \mathbb{E}[X(A)]. \quad (1.51)$$

The intensity measure of a random point process can be seen as the equivalent of the mean of a real-valued random variable. It is of interest to consider the particular case of a stationary point process. A point process is said to be stationary if its distribution is invariant by translation. Hence, for any configuration  $Y$  in  $\mathcal{N}$  and for  $x \in \mathbb{R}^d$ , we have

$$\mathbb{P}\{X \in Y\} = \mathbb{P}\{X + x \in Y\}.$$

For a stationary point process, the intensity measure is necessarily translation-invariant. It implies that

$$\theta(B) = \lambda \mu_D(B), \quad (1.52)$$

where  $\mu_D$  is the  $d$ -dimensional Lebesgue measure on  $\mathbb{R}^d$  and  $\lambda$  some positive real number.

We conclude this section by stating the Campbell theorem, a fundamental result in the theory of random measures and point processes. It shows

that expectations of random integrals with respect to a random measure are completely determined by the intensity measure. As a consequence, many first-order properties of stochastic models driven by random measures can be computed by replacing the random measure with its deterministic intensity. This theorem plays a central role in the study of Poisson random measures, stochastic geometry, and spatial stochastic models.

**Theorem 1.5.1.** *Let  $X$  be a random measure on  $E$  with intensity measure  $\Theta$ , and let  $f : E \rightarrow \mathbb{R}$  be a non-negative, measurable function. Then, we have*

$$\mathbb{E} \left[ \int_E f dX \right] = \int_E f d\Theta. \quad (1.53)$$

*Proof.* Let  $X$  be a random measure on  $E$  with intensity measure  $\Theta$ , that is,

$$\Theta(A) = \mathbb{E}[X(A)] \quad \text{for all measurable } A \subset E.$$

*Step 1.* Assume first that  $f = \mathbf{1}_A$  for some measurable set  $A \subset E$ . Then

$$\int_E f dX = X(A),$$

and therefore

$$\mathbb{E} \left[ \int_E f dX \right] = \mathbb{E}[X(A)] = \Theta(A) = \int_E f d\Theta.$$

*Step 2.* Let  $f$  be a non-negative simple function, i.e.

$$f = \sum_{i=1}^n a_i \mathbf{1}_{A_i},$$

where  $a_i \geq 0$  and the  $A_i$ 's are measurable and disjoint. By linearity of the integral,

$$\int_E f dX = \sum_{i=1}^n a_i X(A_i).$$

Taking expectations and using Step 1,

$$\mathbb{E} \left[ \int_E f dX \right] = \sum_{i=1}^n a_i \mathbb{E}[X(A_i)] = \sum_{i=1}^n a_i \Theta(A_i) = \int_E f d\Theta.$$

*Step 3.* Let  $f$  be a non-negative measurable function. There exists an increasing sequence of non-negative simple functions  $(f_n)_{n \geq 1}$  such that

$$f_n \uparrow f \quad \text{pointwise.}$$

By the monotone convergence theorem,

$$\int_E f_n dX \uparrow \int_E f dX \quad \text{a.s.}$$

and

$$\int_E f_n d\Theta \uparrow \int_E f d\Theta.$$

Applying the monotone convergence theorem to expectations,

$$\mathbb{E}\left[\int_E f dX\right] = \lim_{n \rightarrow \infty} \mathbb{E}\left[\int_E f_n dX\right] = \lim_{n \rightarrow \infty} \int_E f_n d\Theta = \int_E f d\Theta.$$

□

## 1.5.2 Poisson point process

### Definition and characterization

**Definition 1.5.4.** Let  $\theta$  be a locally finite measure on  $\mathbb{R}^d$ . A Poisson point process on  $\mathbb{R}^d$  is a point process such that the number  $N(K)$  of points contained in any compact  $K$  of  $\mathbb{R}^d$  is a Poisson random variable with parameter  $\theta(K)$ :

$$P\{N(K) = k\} = p_k(K) = \frac{\theta(K)^k}{k!} \exp(-\theta(K)), \quad (1.54)$$

where the intensity  $\theta$  is defined by

$$\theta(K) = \int_K \theta(dx). \quad (1.55)$$

**Proposition 1.5.2.** The probability generating function  $G_K(s)$  of the random variable  $N(K)$  is

$$G_K(s) = \sum_{k=0}^{+\infty} p_k(K) s^k = \exp[\theta(K)(s-1)]. \quad (1.56)$$

*Proof.* By definition, the probability generating function of  $N(K)$  is

$$G_K(s) = \mathbb{E}[s^{N(K)}] = \sum_{k=0}^{+\infty} p_k(K) s^k.$$

Using the expression of  $p_k(K)$  for a Poisson random variable with parameter  $\theta(K)$ , we obtain

$$G_K(s) = \sum_{k=0}^{+\infty} \frac{\theta(K)^k}{k!} e^{-\theta(K)} s^k = e^{-\theta(K)} \sum_{k=0}^{+\infty} \frac{(\theta(K)s)^k}{k!}.$$

Recognizing the exponential series, we have

$$\sum_{k=0}^{+\infty} \frac{(\theta(K)s)^k}{k!} = \exp(\theta(K)s).$$

Therefore,

$$G_K(s) = e^{-\theta(K)} \exp(\theta(K)s) = \exp(\theta(K)(s - 1)),$$

which proves the result.  $\square$

An important consequence of definition 1.5.4 is that for any family  $\{K_i, i \in I\}$  of disjoint compact sets, the random variables  $N(K_i)$  are independant. This property is referred to as *complete independance*. In many practical situations, the measure  $\theta$  is proportional to the Lebesgue measure on the  $\sigma$ -algebra of  $\mathbb{R}^d$ . In this case, the Poisson point process is said to be *stationary* and the number  $N(K)$  of points contained in a given compact  $K$  is

$$P\{N(K) = k\} = \frac{(\theta\mu_d(K))^k}{k!} \exp(-\theta\mu_d(K)), \quad (1.57)$$

$\mu_d$  being the Lebesgue measure of  $\mathbb{R}^d$ .

A Poisson point process is easily characterized by its Choquet capacity, as demonstrated below in proposition 1.5.3.

**Proposition 1.5.3.** *The Choquet capacity  $T(K)$  of a Poisson point process is*

$$T(K) = 1 - P\{N(K) = 0\} = 1 - \exp(-\theta(K)). \quad (1.58)$$

If the process is stationary, the Choquet capacity becomes

$$T(K) = 1 - \exp(-\theta\mu_d(K)). \quad (1.59)$$

*Proof.* By definition, the Choquet capacity  $T(K)$  of a Poisson point process is the probability that  $K$  intersects at least one point of the process. According to definition 1.5.4, we have

$$P\{N(K) > 0\} = 1 - P\{N(K) = 0\} = 1 - \exp(-\theta(K)). \quad (1.60)$$

□

For a stationary Poisson point process  $X$ , the intensity can easily be estimated from some experimental dataset by

$$\bar{\theta} = \frac{X(W)}{\mu_d(W)}, \quad (1.61)$$

where  $W$  denotes the observation window in  $\mathbb{R}^d$ . As the size of the window increases, we have  $\bar{\theta} \rightarrow \theta$ .

**Proposition 1.5.4.** *If  $\mathcal{P}_1, \dots, \mathcal{P}_n$  are  $n$  independant Poisson point processes  $\mathcal{P}_k$  with respective intensities  $\theta_1, \dots, \theta_n$ , then the union set  $\mathcal{P} = \bigcup_{k=0}^n \mathcal{P}_k$  is a Poisson point process of intensity  $\theta = \sum_{k=1}^n \theta_k$ .*

*Proof.* Let  $K \subset \mathbb{R}^d$  be a compact set. For each  $k = 1, \dots, n$ , denote by

$$N_k(K)$$

the number of points of the Poisson point process  $\mathcal{P}_k$  contained in  $K$ . Since the point processes  $\mathcal{P}_1, \dots, \mathcal{P}_n$  are independent, the random variables

$$N_1(K), \dots, N_n(K)$$

are independent Poisson random variables with respective parameters  $\theta_1(K), \dots, \theta_n(K)$ .

The number of points of the union process

$$\mathcal{P} = \bigcup_{k=1}^n \mathcal{P}_k$$

contained in  $K$  is

$$N(K) = \sum_{k=1}^n N_k(K).$$

The probability generating function of  $N(K)$  is therefore

$$G_K(s) = \mathbb{E}[s^{N(K)}] = \prod_{k=1}^n \mathbb{E}[s^{N_k(K)}],$$

where we used the independence of the processes. By Proposition 1.5.4, the probability generating function of  $N_k(K)$  is

$$\mathbb{E}[s^{N_k(K)}] = \exp(\theta_k(K)(s-1)).$$

Hence,

$$G_K(s) = \prod_{k=1}^n \exp(\theta_k(K)(s-1)) = \exp\left(\sum_{k=1}^n \theta_k(K)(s-1)\right) = \exp(\theta(K)(s-1)),$$

where

$$\theta(K) = \sum_{k=1}^n \theta_k(K).$$

This is the probability generating function of a Poisson random variable with parameter  $\theta(K)$ . Therefore, for every compact set  $K \subset \mathbb{R}^d$ , the random variable  $N(K)$  is Poisson distributed with parameter  $\theta(K)$ , and the union process  $\mathcal{P}$  is a Poisson point process with intensity measure

$$\theta = \sum_{k=1}^n \theta_k.$$

□

**Proposition 1.5.5** (Nearest-neighbor distance distribution). *Let  $X$  be a stationary Poisson point process. We define the nearest-neighbor distance distribution function  $\Delta$  to be the distribution of the random distance from a typical point  $x$  of  $X$  to the nearest other point in the process. Since  $X$  is stationary, without loss of generality, it suffices to consider the case where the typical point  $x$  is the origin 0. Then, the probability distribution of  $\Delta$  satisfies*

$$\mathbb{P}\{\Delta \leq r\} = 1 - e^{-\theta r^d \mu_d(B^d)},$$

where  $\mu_d(B^d)$  is the Lebesgue measure of the unit ball in  $\mathbb{R}^d$ .

*Proof.* Let  $X$  be a stationary Poisson point process on  $\mathbb{R}^d$  with constant intensity  $\theta$ . By stationarity, we may assume without loss of generality that the typical point is located at the origin 0.

The event  $\{\Delta > r\}$  means that there is no other point of the process within distance  $r$  from the origin. Equivalently,

$$\{\Delta > r\} = \{X(B_r^d \setminus \{0\}) = 0\},$$

where  $B_r^d$  denotes the ball of radius  $r$  centered at the origin. Since the Poisson point process is simple, the probability of having another point exactly at the origin is zero, and we may write

$$\mathbb{P}\{\Delta > r\} = \mathbb{P}\{X(B_r^d) = 0\}.$$

Because  $X$  is a Poisson point process, the number of points in  $B_r^d$  follows a Poisson distribution with parameter

$$\theta \mu_d(B_r^d),$$

where  $\mu_d(B_r^d)$  is the Lebesgue measure of  $B_r^d$ . Hence,

$$\mathbb{P}\{X(B_r^d) = 0\} = \exp(-\theta \mu_d(B_r^d)).$$

Since  $\mu_d(B_r^d) = r^d \mu_d(B^d)$ , where  $B^d$  is the unit ball in  $\mathbb{R}^d$ , we obtain

$$\mathbb{P}\{\Delta > r\} = \exp(-\theta r^d \mu_d(B^d)).$$

Therefore,

$$\mathbb{P}\{\Delta \leq r\} = 1 - \mathbb{P}\{\Delta > r\} = 1 - \exp(-\theta r^d \mu_d(B^d)),$$

which proves the result.  $\square$

### Simulation of a stationary Poisson point process

We describe in this paragraph the practical implementation of a stationary Poisson point process in a domain  $\mathcal{D} \subset \mathbb{R}^d$ . The simulation is carried out in two steps:

- First, one generates a Poisson random variable that determines the number of points located in the domain  $\mathcal{D}$ .

- Second, the corresponding number of points is sampled independently and uniformly over  $\mathcal{D}$ .

Poisson random variables can be generated from uniform random variables. In particular, if  $U$  is a random variable uniformly distributed on  $[0, 1]$ , then the random variable  $-\ln(U)$  follows an exponential distribution, which can be used as a building block in standard algorithms for simulating Poisson random variables.

The second step of the simulation consists in generating points uniformly distributed in the domain  $\mathcal{D}$ . It is straightforward to simulate a random point uniformly distributed in the unit cube  $[0, 1]^d$ . For hypercubic domains, one may therefore generate points in  $[0, 1]^d$  and then apply an appropriate translation and scaling to obtain points uniformly distributed in the desired domain. For more general domains, uniform sampling can be achieved using rejection sampling or approximation techniques:

- Rejection sampling consists in enclosing  $\mathcal{D}$  within a rectangular domain  $\mathcal{R}$ . Independent uniform points are generated in  $\mathcal{R}$  until a point falls inside  $\mathcal{D}$ ; this procedure is repeated until the required number of points in  $\mathcal{D}$  is obtained.
- Approximation methods consist in replacing the domain  $\mathcal{D}$  by a finite union of simple sets, such as open hypercubes, that approximate  $\mathcal{D}$  and from which uniform sampling is straightforward.

### Cox-Poisson point processes

**Definition 1.5.5.** Let  $\theta$  be a locally random finite measure on  $\mathbb{R}^d$ . A Cox-Poisson point process on  $\mathbb{R}^d$  is a point process such that the number  $N(K)$  of points contained in any compact  $K$  of  $\mathbb{R}^d$  is a Poisson random variable with parameter  $\theta(K)$ :

$$P\{N(K) = k\} = p_k(K) = \frac{\theta(K)^k}{k!} \exp(-\theta(K)), \quad (1.62)$$

where the intensity  $\theta$  is the random variable defined by

$$\theta(K) = \int_K \theta(dx). \quad (1.63)$$

Cox-Poisson point processes are an extension of Poisson point processes in the sense that for these processes, the intensity  $\theta$  is a random variable.

A fundamental example of Cox point processes are Poisson point processes restricted to some random closed set. Let  $A$  be a random closed set of  $\mathbb{R}^d$ , an  $\lambda > 0$ . The measure

$$\theta(K) = \int_K \theta 1_A(x) dx, \quad (1.64)$$

where  $1_A$  is the indicative function of the set  $A$  defines a Cox-Poisson point process. This Cox-Poisson point process can be seen as the restriction of a stationary Poisson point process of intensity  $\theta$  to the random closed set  $A$ . Such point processes are often used in stochastic geometry to construct multiscale models. We refer the reader interested by these models to the book [[Jeulin, 2021a](#)].

### Hard-core point processes

A hard-core point process is a point process for which the points cannot lie closer than a specified distance  $D$ . Let  $\mathcal{P}$  be an homogeneous Poisson point process with intensity  $\theta$ . We can obtain a hard-core point process by thinning. Thinning consists in deleting points from the point process according to some rules. In practice, for some domain  $\Omega$ , we first generate the Poisson variable  $N$  that indicates the number of points implanted in the domain. Then, we generate the points of the process sequentially. The thinning procedure occurs at each step of the simulation when a new point is added. If the nearest point is closer than the hard-core distance  $D$ , then the new implanted point is deleted.

Hard-core point processes are widely used in practical applications to model repulsion phenomena.

### 1.5.3 Marked point processes

A marked point process is a point process for which a characteristic is attached to each point. The notion of marked point process is fundamental in stochastic geometry and is used in many applications. We will subsequently use marked point processes to study the general Boolean model in section 1.6.

In mathematical terms, a marked point process on  $\mathbb{R}^d$  is a random sequence  $\{(x_n, m_n)\}$  where the points  $x_n$  constitute a point process (unmarked) called the ground process and the  $m_n$  are the marks corresponding to the respective points. A marked point process can also be seen as a point process on  $\mathbb{R} \times \mathcal{M}$ , where  $\mathcal{M}$  is a locally compact space with countable base. This lead to the rigorous definition

**Definition 1.5.6.** *A marked point process in  $\mathbb{R}^d$  with mark space  $M$  is a simple point process  $X$  in  $\mathbb{R}^d \times \mathcal{M}$  with intensity measure  $\theta$  satisfying  $\theta(C \times \mathcal{M}) < \infty$  for all compact set  $C$  in  $\mathcal{K}(\mathbb{R}^d)$ .*

The marks can be continuous or discrete variables. A marked point process is said to be stationary if its ground process is stationary. Similarly, a marked Poisson point process is simply a marked point process whose ground process is Poisson.

**Definition 1.5.7.** *The intensity measure of a marked point process  $X$  on  $\mathbb{R}^d \times \mathcal{M}$  is*

$$\theta(B \times L) = \mathbb{E}(X(B \times L)), \quad (1.65)$$

where  $B$  is a Borel set of  $\mathbb{R}^d$  and  $L$  a measurable set of  $\mathcal{M}$ .

Intuitively,  $\theta(B \times L)$  is the mean number of points in  $B$  that have their mark in  $L$ . The Campbell formula can be generalized to the case of marked point processes. Hence, let  $X$  denote a marked point process on  $\mathbb{R}^d \times \mathcal{M}$ . Then, we have

$$\mathbb{E}\left\{\sum_{(x,m) \in X} f(x, m)\right\} = \int f(x, m) d\Theta(x, m) \quad (1.66)$$

for any non-negative function  $f$ .

It can be shown (see for instance [Schneider and Weil, 2008]) that the intensity of a marked point process can be decomposed in the following manner

$$d\Theta(x, m) = d\theta(x)dM_x(m), \quad (1.67)$$

where  $\theta$  is the intensity measure of the ground point process and  $M_x$  is a probability measure on  $\mathcal{M}$ . We interpret  $M_x$  as the mark distribution of a point at location  $x$ .

For a stationary marked point process, for all subsets  $L$  of  $\mathcal{M}$ ,  $\Theta(\cdot \times L)$  is a translation-invariant measure, so that, for all Borelian set  $B$  in  $\mathcal{B}(\mathbb{R}^d)$ :

$$\Theta(B \times L) = \theta_L \mu_d(B), \quad (1.68)$$

where  $\mu_d$  is the Lebesgue measure on  $\mathbb{R}$ . The quantity  $\theta_L$  is the intensity of  $\mathcal{P}$  with respect to  $L$ , and can be interpreted as the mean number of points of  $\mathcal{P}$  per unit volume with marks in  $L$ . Obviously, if  $L = \mathcal{M}$ , we have  $\theta_L = \theta$ , where  $\theta$  is the intensity of the ground point process.

**Example** Let  $X$  be a Poisson point process in the plane  $\mathbb{R}^2$  with intensity  $\theta$ . To each point  $x_n \in X$ , we associate a random mark  $m_n$  drawn from the uniform law on  $[0, 1]$ . All marks are drawn independently.  $\{(x_n, m_n)_{x_n \in X}\}$  is a marked point process. The mark space  $\mathcal{M}$  is the  $\sigma$ -algebra  $([0, 1], \mathcal{B}([0, 1]))$ .

## 1.6 Germ-grain processes

### 1.6.1 Definition and first properties

**Definition 1.6.1.** Let  $\Psi = \{x_n; A_n\}$  be a marked point process, where the points  $x_n$  lie in  $\mathbb{R}^d$  and the marks  $A_n$  are random compact subsets of  $\mathbb{R}^d$ . A germ-grain model can be defined from  $\Psi$  by considering the union

$$A = \bigcup_{n=1}^{\infty} (A_n \oplus x_n). \quad (1.69)$$

The points  $x_n$  are called the germs of the process and the compact sets  $A_n$  the grains of the germ-grain model.

In this section, we will restrict ourselves to the study of the Boolean model. The Boolean model is an archetypal example of germ-grain process. It is a grain model which is obtained by implanting independant random primary grains  $A'$  on the germs  $\{x_k\}$  of a Poisson points process  $\mathcal{P}$  with intensity  $\theta$ . Note that primary grains can possibly overlap. The resulting set  $A$  is

$$A = \bigcup_{x_k \in \mathcal{P}} A'_{x_k}, \quad (1.70)$$

where  $A'_{x_k}$  denotes the translated of the primary grain  $A'$  at point  $x_k$ :

$$A'_{x_k} = A' \oplus x_k = \{x_k + y, y \in A'\}. \quad (1.71)$$

Any shape can be used for the primary grains  $A'$ , including convex, non-convex or even non connected sets. In the literature,  $A'$  is commonly referred to as the typical grain of the model.

**Definition 1.6.2.** *A Boolean model is said to be stationary if the intensity of its germ process is stationary.*

### First properties

**Lemma 1.6.1.** *Let  $K$  be a compact set of  $\mathbb{R}^d$  and  $A$  a Boolean model with primary grain  $A'$  and with intensity  $\theta$ . The number  $N(K)$  of primary grains hit by  $K$  follows a Poisson distribution of parameter  $\mathbb{E}\{\theta(\check{A}' \oplus K)\}$ :*

$$P\{N = n\} = \frac{\mathbb{E}\{\theta(\check{A}' \oplus K)\}^n}{n!} \exp(-\mathbb{E}\{\theta(\check{A}' \oplus K)\}) \quad (1.72)$$

*Proof.* We denote by  $\mathcal{P}$  the germ process associated to  $A$ . We can produce a thinned point process  $\mathcal{P}_K$  out of  $\mathcal{P}$  by deleting all points  $x_n$  from  $\mathcal{P}$  such that  $A'_{x_n} \cap K = \emptyset$ . Whether or not a given germ  $x_n$  is deleted by this procedure is independant of thinning of other germs. As a consequence,  $\mathcal{P}_K$  is an inhomogeneous Poisson point process.

We denote by  $\theta_K$  the intensity of the thinned process  $\mathcal{P}_K$ . We have

$$\theta_K(x) = \theta \mathbb{P}\{A_x \cap K \neq \emptyset\}.$$

The total number of points of  $\mathcal{P}_K$  has a Poisson distribution with mean

$$\bar{N}_K = \theta \int_{\mathbb{R}^d} \mathbb{P}\{A_x \cap K \neq \emptyset\} dx.$$

Since  $\mathbb{P}\{A_x \cap K \neq \emptyset\} = \mathbb{P}\{x \in \check{A}_x \oplus K\}$ , we have

$$\bar{N}_K = \theta \int_{\mathbb{R}^d} \mathbb{P}\{x \in \check{A}_x \oplus K\} dx = \theta \mathbb{E}(\mu(\check{A}' \oplus K)),$$

where  $\mu$  is the Lebesgues measure on  $\mathbb{R}^3$ . This establishes formula 1.72.  $\square$

Lemma 1.6.1 guarantees that the number of primary grains in any bounded window remains almost surely finite as long as  $\mathbb{E}[\theta(A')] < \infty$ . We can easily calculate the Choquet capacity of the boolean model to find

$$T(K) = 1 - \exp(-\mathbb{E}\{\theta(\check{A}' \oplus K)\}) \quad (1.73)$$

for any compact set  $K$  in  $\mathcal{K}(E)$ . For the stationnary case, the Choquet capacity becomes

$$T(K) = 1 - \exp(-\theta \bar{\mu}(\check{A}' \oplus K)), \quad (1.74)$$

where  $\bar{\mu}(\check{A}' \oplus K)$  denotes the average Lebesgue measure (i.e the average volume) of a primary grain  $A'$  dilated by the compact set  $K$ .

We can determine the spatial law of the Boolean model by considering the Choquet capacity for the structuring element  $\{x\}$ . For the stationnary case, according to 1.73, we find

$$q = P\{x \in A^c\} = \exp(-\theta \bar{\mu}(\check{A}')). \quad (1.75)$$

Note that we can easily express the Choquet capacity as a function of  $q$ . Hence, we have

$$T(K) = 1 - q \frac{\bar{\mu}(A' \oplus \check{K})}{\bar{\mu}(A')}, \quad (1.76)$$

where we have used the relation  $A' \oplus \check{K} = -\check{A}' \oplus K$ .

Using equation 1.73, it is also possible to calculate the covariance of the Boolean model. Recall that the covariance is defined as a function of vector  $h$  of  $\mathbb{R}^3$  by

$$C(h) = P\{x \in A, x + h \in A\}. \quad (1.77)$$

$C(h)$  is exactly the Choquet capacity for the structuring element  $l_h = \{x\} \cup \{x + h\}$ . Thus, we find

$$C(h) = 1 - \exp(-\mathbb{E}\{\theta(\check{A} \oplus l_h)\}). \quad (1.78)$$

For the stationnary case, the covariance yields

$$C(h) = 1 - \exp(-\theta \bar{\mu}(\check{A} \oplus l_h)). \quad (1.79)$$

**Proposition 1.6.2.** *If  $A$  is a Boolean model with typical grain  $A'$  and intensity  $\theta$ , the covariance of  $A$  is given by*

$$C(h) = 2p - 1 + (1 - p)^2 \exp(\theta \mathbb{E}(\gamma_{A'}(h))), \quad (1.80)$$

where  $\gamma_{A'}(h) = \bar{\mu}(A' \cap A'_{-h})$  is the geometrical covariogram of  $A'$  and  $p = 1 - q$ .

*Proof.* From the probabilistic definition of the covariance, we find

$$C(h) = P\{0 \in A \cap A_{-h}\} \quad (1.81)$$

$$= 1 - P\{0 \notin A\} + P\{0 \notin A_{-h}\} - P\{0 \notin A \cup A_{-h}\} \quad (1.82)$$

$$= 2p - 1 + P\{0 \notin A \cup A_{-h}\} \quad (1.83)$$

In addition, we have

$$P\{0 \notin A \cup A_{-h}\} = \exp(-\theta\bar{\mu}(A \cup A_{-h})) \quad (1.84)$$

$$= (1-p)^2 \exp(-\theta\bar{\mu}(A \cap A_{-h})), \quad (1.85)$$

since  $\bar{\mu}(A \cup A_{-h}) = \bar{\mu}(A) + \bar{\mu}(A_{-h}) - \bar{\mu}(A \cap A_{-h})$ . This establishes formula (1.80).  $\square$

## Examples

To illustrate the use of formula (1.80), we now consider explicit examples of typical grains  $A'$  for which the geometrical covariogram  $\gamma_{A'}(h)$  can be computed analytically. These examples provide concrete expressions for the covariance function  $C(h)$  of the Boolean model and highlight how the shape and size of the grains influence spatial correlations in the model. We first examine the case of circular disks in  $\mathbb{R}^2$ , followed by spherical grains in  $\mathbb{R}^3$ .

**Proposition 1.6.3.** *The geometrical covariogram of a disk with constant radius  $R$  in  $\mathbb{R}^2$  is*

$$\gamma(R) = 2R^2 \left( \arccos\left(\frac{h}{2R}\right) - \frac{h}{2R} \sqrt{1 - \left(\frac{h}{2R}\right)^2} \right). \quad (1.86)$$

*Proof.* The geometrical covariogram  $\gamma(h)$  of a set  $A \subset \mathbb{R}^2$  is defined as the area of the intersection of  $A$  with its translation by a vector of length  $h$ :

$$\gamma(h) = \mu_2(A \cap (A + \mathbf{v})), \quad \|\mathbf{v}\| = h,$$

where  $\mu_2$  denotes the Lebesgue measure in  $\mathbb{R}^2$ .

Let  $A$  be a disk of radius  $R$ . By rotational symmetry, the intersection area depends only on the distance  $h$  between the centers. When  $h \geq 2R$ , the disks do not intersect, so  $\gamma(h) = 0$ . For  $0 \leq h \leq 2R$ , the intersection forms a symmetric lens-shaped region.

The area of the lens formed by two circles of radius  $R$  with centers separated by  $h$  is given by the standard formula:

$$\mu_2(A \cap (A + \mathbf{v})) = 2R^2 \arccos\left(\frac{h}{2R}\right) - \frac{h}{2} \sqrt{4R^2 - h^2}.$$

Factoring the expression slightly differently, we can write

$$\frac{h}{2} \sqrt{4R^2 - h^2} = 2R^2 \frac{h}{2R} \sqrt{1 - \left(\frac{h}{2R}\right)^2}.$$

Substituting this into the previous formula, we obtain

$$\gamma(h) = 2R^2 \left[ \arccos\left(\frac{h}{2R}\right) - \frac{h}{2R} \sqrt{1 - \left(\frac{h}{2R}\right)^2} \right],$$

which proves the proposition.  $\square$

**Proposition 1.6.4.** *The geometrical covariogram of a sphere with constant radius  $R$  in  $\mathbb{R}^3$  is*

$$\gamma(R) = \frac{4\pi R^3}{3} \left( 1 - \frac{3h}{4R} + \frac{h^3}{16R^3} \right). \quad (1.87)$$

*Proof.* The geometrical covariogram  $\gamma(h)$  of a set  $A \subset \mathbb{R}^3$  is defined as the volume of the intersection of  $A$  with its translation by a vector of length  $h$ :

$$\gamma(h) = \mu_3(A \cap (A + \mathbf{v})), \quad \|\mathbf{v}\| = h,$$

where  $\mu_3$  denotes the Lebesgue measure in  $\mathbb{R}^3$ .

Let  $A$  be a sphere of radius  $R$  centered at the origin. By rotational symmetry, the intersection volume depends only on the distance  $h$  between the centers. If  $h \geq 2R$ , the spheres do not intersect, so  $\gamma(h) = 0$ . For  $0 \leq h \leq 2R$ , the intersection forms a lens-shaped region (a spherical cap union).

The volume of intersection can be computed by integrating the areas of circular slices perpendicular to the line connecting the centers. If we place the centers along the  $x$ -axis at 0 and  $h$ , the intersection along  $x \in [\frac{h}{2} - R, R]$

has circular cross-section of radius  $\sqrt{R^2 - x^2}$ . The resulting volume formula is well-known (see, e.g., standard formulas for spherical caps):

$$\gamma(h) = \frac{4\pi R^3}{3} \left( 1 - \frac{3h}{4R} + \frac{h^3}{16R^3} \right).$$

Hence, the geometrical covariogram of a sphere of radius  $R$  in  $\mathbb{R}^3$  is given by the stated expression.  $\square$

### 1.6.2 Practical implementation

Simulations of random structures are generally performed on a grid of points (i.e 2D or 3D images), using primary grains based on combination of pixels. One can however rely on a completely different approach based upon level sets and implicit functions. In this approach, primary grains are described by implicit functions, which are real valued functions defined in the ambient space. The level sets of an implicit function  $\Phi$  are described by an equation of the form  $\Phi(x, y, z) = c$ , for some constant  $c$ . A surface is described as a level set of the function  $\Phi$ , most commonly the set of points for which  $\Phi(x, y, z) = 0$ . In this case, the points for which  $\Phi(x, y, z) < 0$  correspond to the interior of the primary grain associated to the implicit function, the points for which  $\Phi(x, y, z) > 0$  to its complementary and the level set  $\Phi(x, y, z) = 0$  to the boundary of the primary grain. We can use any primary grain, whatever its shape, as long as we can represent it using an implicit function.

In the implicit function approach, complete simulations are generated using Boolean combinations of primary implicit functions: the union and the intersection of two objects  $A_1$  and  $A_2$  are defined to yield the minimum and the maximum, respectively, of their corresponding implicit functions. Thus, we have

$$\Phi(A_1 \cup A_2) = \min\{\Phi(A_1), \Phi(A_2)\}$$

and

$$\Phi(A_1 \cap A_2) = \max\{\Phi(A_1), \Phi(A_2)\}.$$

Similarly, the complementary  $A^c$  of set  $A$  is defined to be the opposite function

$$\Phi(A^c) = -\Phi(A).$$

Overall, using implicit functions to perform the simulation allows us to build complex combinations of simulations that we could not process with a pixel

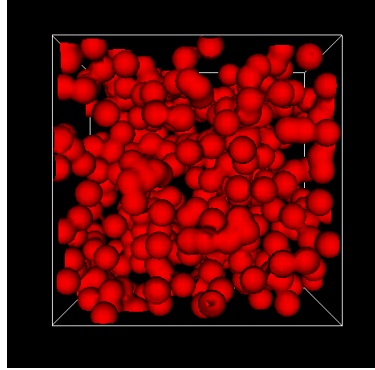


Figure 1.2: 3D Realization of a Boolean model of spheres with constant radius  $R$  and intensity  $\theta$ , realized with the software vtkSim [Faessel and Jeulin, 2011]. The parameters of the model are  $\theta = 5 \times 10^{-2}$  and  $R = 1$ .

based method. Furthermore, vectorial simulations do not require a large amount of computer resources.

### 1.6.3 Statistical analysis for the Boolean model

In this section, we discuss statistical analysis for the Boolean model. For simplicity's sake, we restrict ourselves to the 2D and 3D cases. Our main objective is to determine the parameters of a Boolean model such as its intensity  $\theta$  or its mean intrinsic volumes.

#### Method of densities

The method of densities (or intensities) was developed by Weil in 1984 [Weil and Wieacker, 1984] and Santaló [Santaló] to recover the parameters of a Boolean from a given dataset. The main idea of the method is stated in proposition 1.6.5 below.

**Proposition 1.6.5.** *Let  $A$  be some random closed set in  $\mathbb{R}^d$ . The density of the  $k^{\text{th}}$  intrinsic volume in  $\mathbb{R}^d$  can be estimated from the dataset by relation*

$$v_k = \lim_{r \rightarrow \infty} \frac{\mathbb{E}\{V_k(A \cap B(0, r))\}}{\mu_d(B(0, r))}. \quad (1.88)$$

We recall that for  $d = 2$ , the intrinsic volumes are given by

$$A_A = v_2, \quad (1.89)$$

$$L_A = 2v_1, \quad (1.90)$$

$$N_A = v_0. \quad (1.91)$$

$$(1.92)$$

where  $A_A$  and  $L_A$  are the mean area and perimeter of the typical grain, respectively.  $N_A$  is called specific connectivity number. For  $d = 3$ , the intrinsic volumes are given by

$$V_V = v_3, \quad (1.93)$$

$$S_V = 2v_2, \quad (1.94)$$

$$M_V = \pi v_1, \quad (1.95)$$

$$N_V = v_0, \quad (1.96)$$

$$(1.97)$$

where  $S_V$ ,  $M_V$  and  $N_V$  are the surface area, the specific mean curvature and the specific connectivity number, respectively.

For models with convex grains, it is possible to relate the mean values of the intrinsic volumes of the typical grain to measurements conducted on the global dataset through Miles' formulae [Miles, 1976]. For  $d = 2$ , Miles' formulae yield

$$A_A = p = 1 - \exp(-\theta \bar{A}), \quad (1.98)$$

$$L_A = \theta(1-p)\bar{S} = \theta \exp(-\theta \bar{V})\bar{S}, \quad (1.99)$$

$$N_A = \theta(1-p) \left( 1 - \frac{\theta \bar{L}^2}{4\pi} \right). \quad (1.100)$$

For  $d = 3$ , Miles' formulae yield

$$V_V = p = 1 - \exp(-\theta \bar{V}), \quad (1.101)$$

$$S_V = \theta(1-p)\bar{S} = \theta \exp(-\theta \bar{V})\bar{S}, \quad (1.102)$$

$$M_V = \theta(1-p)\bar{S} \left( \bar{M} - \frac{\pi^2 \theta \bar{S}^2}{32} \right), \quad (1.103)$$

$$N_V = \theta(1-p) \left( 1 - \frac{\theta \bar{M} \bar{S}}{4\pi} + \frac{\pi \theta^2 \bar{S}^3}{384} \right). \quad (1.104)$$

Hence, when estimates of the densities are given, the intensities of the Boolean model can easily be found. We refer the reader interested by a proof of Miles' formulae to the original paper [Miles, 1976] and to the book [Schneider and Weil, 2008].

We can illustrate the methodology for a Boolean model of disks with unknown constant radius  $R$  and intensity  $\theta$ . We suppose that we dispose of a dataset, from which we can estimate a fraction area  $A_A$  and a perimeter  $L_A$ . The area of the typical grain is constant and yields  $\bar{A} = \pi R^2$ . Similarly, the perimeter of the typical grain yields  $\bar{L} = 2\pi R$ . Therefore, Miles' formulae yield

$$A_A = 1 - \exp(-\theta\pi R^2), \quad (1.105)$$

$$L_A = \theta(1 - A_A)2\pi R. \quad (1.106)$$

We can easily solve to find  $R$  and  $\theta$ .

### Minimum contrast method

The minimum contrast is another statistical method which can be employed to perform parameter identification for germ-grain models. It consists in trying to determine the parameters that minimize the distance between some characteristic function measured on the dataset and the corresponding function obtained either from its theoretical expression or from random realization of the model. For Boolean models, covariance is classically used in this purpose, often in combination with granulometry curves. Usually, the grain-germ models are not traceable analytically, and we have to rely on numerical methods to perform the optimization. Nelder-Mead and Levenberg-Marcquart algorithms are often used in this purpose [Jean et al., 2011]. We discuss in chapter 2 an approach for selecting the parameters of the models based on a Bayesian approach.

### Stereological mean-value formulae

In many practical situation, we want to study the microstructure of a 3D material through 2D images that correspond to a slice of the material or to a thick section. Hence, we are left with the following question: how to relate the 2D measurements to intrinsic properties of the material?

Let  $A_v$  be a spatial stationary grain-germ process in  $\mathbb{R}^3$ . We assume that the grains are convex. We consider the intersection of  $A_a$  of  $A_v$  with an arbitrary plane  $P$ :

$$A_a = A_v \cap P. \quad (1.107)$$

We denote  $(x_1, x_2, x_3)$  an orthonormal system of coordinates in  $\mathbb{R}^3$  such that  $x_1 \in P$  and  $x_2 \in P$ . For  $r > 0$ , we consider the disk

$$c_r = \{x = (x_1, x_2), x_1^2 + x_2^2 < r\}.$$

The number of grains hitting  $c_r$  is necessarily the same for  $A_v$  and  $A_a$ . Hence, using Steiner's formula, we find

$$\theta_v \left( \bar{V} + \frac{\pi \bar{S}r}{4} + \pi \bar{b}r^2 \right) = \theta_a \left( \bar{A} + \bar{L}r + \pi r^2 \right). \quad (1.108)$$

This equation must be valid for all  $r > 0$ , which proves proposition 1.6.6.

**Proposition 1.6.6.** *The mean value characteristics of  $A_v$  and  $A_a$  are related through relations*

$$\theta_v \bar{V} = \theta_a \bar{A} \quad (1.109)$$

$$\theta_v \frac{\pi \bar{S}}{4} = \theta_a \bar{L} \quad (1.110)$$

$$\theta_v \bar{b} = \theta_a. \quad (1.111)$$

**Example** Let us consider a stationary Boolean model of spheres in  $\mathbb{R}^3$  with unknown intensity  $\theta_v$  and constant radius  $R$ . The grains are balls of radius  $R$ . Experimental observations consist of planar sections of the material. The intersection of the three-dimensional Boolean model with an arbitrary plane  $P$  yields a two-dimensional Boolean model of disks, denoted by  $A_a$ .

For a sphere of radius  $R$ , the intrinsic volumes are given by

$$\bar{V} = \frac{4}{3}\pi R^3, \quad \bar{S} = 4\pi R^2, \quad \bar{b} = 1.$$

From Proposition 1.6.6, the mean value characteristics of the three-dimensional and planar models satisfy

$$\theta_v \bar{V} = \theta_a \bar{A}, \quad \theta_v \frac{\pi \bar{S}}{4} = \theta_a \bar{L}, \quad \theta_v \bar{b} = \theta_a.$$

Since  $\bar{b} = 1$ , the last relation implies  $\theta_a = \theta_v$ . Substituting the expressions of  $\bar{V}$  and  $\bar{S}$  into the first two relations yields

$$\bar{A} = \frac{4}{3}\pi R^3, \quad \bar{L} = \pi^2 R^2.$$

The planar model  $A_a$  is therefore a Boolean model of disks with intensity  $\theta_a$  and mean area  $\bar{A}$ . Its area fraction  $A_A$  and perimeter density  $L_A$  satisfy

$$A_A = 1 - \exp(-\theta_a \bar{A}), \quad L_A = \theta_a \bar{L} \exp(-\theta_a \bar{A}).$$

From the first equation we obtain

$$\theta_a \bar{A} = -\ln(1 - A_A).$$

Substituting this relation into the expression of  $L_A$  gives

$$L_A = \theta_a \bar{L}(1 - A_A).$$

Replacing  $\bar{A}$  and  $\bar{L}$  by their expressions leads to the system

$$-\ln(1 - A_A) = \theta_v \frac{4}{3}\pi R^3,$$

and

$$L_A = \theta_v \pi^2 R^2 (1 - A_A).$$

Dividing the second equation by the first yields

$$\frac{L_A}{1 - A_A} = \frac{3\pi}{4R} (-\ln(1 - A_A)),$$

from which the radius is obtained as

$$R = \frac{3\pi}{4} \frac{(1 - A_A) \ln\left(\frac{1}{1 - A_A}\right)}{L_A}.$$

Finally, substituting this expression of  $R$  into the first equation gives the intensity

$$\theta_v = \frac{-\ln(1 - A_A)}{\frac{4}{3}\pi R^3}.$$

Hence, the parameters  $\theta$  and  $R$  of the three-dimensional Boolean model of spheres are uniquely determined from the planar measurements  $A_A$  and  $L_A$ .

### 1.6.4 Notes

The Boolean model is an archetypal model of stochastic geometry. Reference textbooks on this topic include [Matheron, 1975], [Serra, 1982], [Chiu et al., 2013] and [Baccelli and Blaszczyszyn, 2009]. We also refer the reader to the lecture notes [Jeulin, 2021a]. For an extensive presentation, we refer the reader to the book [Schneider and Weil, 2008].

Regarding statistical analysis for the Boolean model, we refer the reader to the papers [Weil and Wieacker, 1984] and [Molchanov, 1995]. Miles' formulae were derived by Miles in 1976 [Miles, 1976]. An introduction can be found in the book [Chiu et al., 2013]. This topic is discussed more thoroughly in the book [Schneider and Weil, 2008].

Another topic of interest regarding the Boolean model is percolation. This topic has been studied extensively over the years. We refer the reader interested by this the percolation properties of the Boolean model to the papers [Hall, 1988, Jeulin and Moreaud, 2006, Figliuzzi et al., 2016], and to the book [Torquato, 2002].

In materials engineering, the Boolean model has been employed to simulate a wide range of microstructures. Various examples of the application of the Boolean model in materials science are described in the paper [Hermann, 1991]. In 1992, Quenec'h *et al.* used the Boolean model to study the growth of WC grains in WC-Co cermets [Quenech et al., 1992]. In 2001, Jeulin *et al.* relied on Poisson polyhedra to simulate the microstructure of needle-shaped gypsum crystal grains [Jeulin et al., 2001]. In 2003, Capasso studied the application of the Boolean model to the description of crystallisation in metals and polymers. More recently, Jean *et al.* simulated the microstructure of rubbers by considering a multiscale Cox-Boolean model [Jean et al., 2011]. Using a random walk based model, Altendorf and Jeulin developed a stochastic model for simulating 3D fiber structures [Altendorf and Jeulin, 2011]. Pereyga *et al.* relied on a Boolean model of random cylinders to model a random fibrous network [Peyrega et al., 2011].

## 1.7 Random Tessellations

A *tessellation* or *mosaic* is a division of the  $d$ -dimensional Euclidean space  $\mathbb{R}^d$  into polyhedra. Such geometrical patterns can be observed in many natural situations. Hence, random tessellation models have been widely used in

physics, materials science and chemistry.

### 1.7.1 General introduction

**Definition 1.7.1.** A tessellation in  $\mathbb{R}^d$  is a countable system  $\mathcal{T}$  of subsets satisfying the following conditions:

- $\mathcal{T} \in \mathcal{F}_{lf}(\mathbb{R}^d)$ , meaning that  $\mathcal{T}$  is a locally finite system of nonempty closed sets.
- The sets  $K \in \mathcal{T}$  are compact, convex and have interior points.
- The sets of  $\mathcal{T}$  cover the space,

$$\cup_{K \in \mathcal{T}} K = \mathbb{R}^d \quad (1.112)$$

- If  $K$  and  $K'$  are two sets of  $\mathcal{T}$  then their interiors are disjoint.

We denote by  $\mathbb{T}$  the set of all tessellations.

The faces of a cell  $C$  of the tessellation are the intersections of  $C$  with its supporting hyperplanes. A  $k$ -face is a face of dimension  $k$ . Among all possible  $k$ -faces, the 0-faces, or vertices, and the 1-faces, or edges, are of particular interest. The  $d-1$  dimensional faces of a  $d$ -dimensional polytope will be referred to as its facets.

**Proposition 1.7.1.** The cells of a tessellation  $\mathcal{T}$  are convex polytopes.

*Proof.* Let  $m$  be a mosaic and  $C \in m$ . Since  $m$  is locally finite, there are only a finite number of cells, say  $C_1, C_2, \dots, C_m \in m\{C\}$  that intersect  $C$ . Since a mosaic covers the whole space  $\mathbb{R}^d$ , the boundary  $C$  of  $C$  is found to be

$$C = \cup_{i=1}^m (C_i \cap C).$$

By definition, for each  $i$  between 0 and  $m$ , the relative interiors of  $C$  and  $C_i$  are disjoint. Therefore, the convex bodies  $C$  and  $C_i$  can be separated by a hyperplane  $H_i$ . More precisely, there exists an hyperplane  $H_i$  such that the closed halfspaces  $H_i^+$  and  $H_i^-$  bounded by  $H_i$  satisfy  $C \subset H_i^+$  and  $C_i \subset H_i^-$ . Note that this is only true because we are considering convex bodies. As a consequence, we have

$$C \subset \cap_{i=1}^m H_i^+.$$

Reciprocally, let  $x$  be in  $\cap_{i=1}^m H_i^+$ . We suppose that  $x \notin C$ . Let  $y$  be an interior point of  $C$ . Necessarily,  $y \in \cap_{i=1}^m H_i^+$ . The line segment with end points  $x$  and  $y$  obviously contains a boundary point  $x'$  of the cell  $C$ . On the one hand, since  $x \neq x'$ ,  $x' \in \cap_{i=1}^m H_i^+$ . On the other hand,  $x' \in C_j$  for some  $j \in \{1, \dots, m\}$ . This leads to a contradiction. Therefore, if  $x$  is in  $\cap_{i=1}^m H_i^+$ , then  $x$  is necessarily in  $C$ . We have demonstrated that

$$C = \cap_{i=1}^m H_i^+.$$

Being compact and the finite intersection of closed halfspace,  $C$  is necessarily a convex polytope.  $\square$

### General study

The general study of tessellations is rather technical, and falls beyond the scope of this introductory material. Therefore, in this chapter, we will only try to point out the general ideas behind the theory. We refer the reader interested by a more comprehensive study of general tessellation to the literature.

A fruitful idea to study general tessellations is to rely on the stochastic structures induced by the tessellation on the ambient space. For instance, if we consider a tessellation of the plane  $\mathbb{R}^2$ , the edges of the tessellation can be seen as a segment process. A  $d$ -dimensional tessellation  $\mathcal{T}$  also induces point processes in  $\mathbb{R}^d$ . For instance, the set of vertices of  $\mathcal{T}$ , the set of edges midpoints or the set of all cells centroids are random point processes of  $\mathbb{R}^d$ . By determining mean-value formulae for these point processes, it is possible to characterize some of the geometrical properties of  $\mathcal{T}$ . For instance, the intensity of the random point process constituted by all cells centroid correspond the mean number of cells of the tessellation per volume unit. The number  $n_{d-1,d}(x)$  of edges emanating from the vertex  $x$  or the number of cells containing  $x$  are additional features of interest. Again, mean values for these quantities characterize the geometry of the tessellation. The determination of mean-values formulae for these quantites is a difficult problem, which often builds upon marked point processes theory.

Another common approach is to rely on germ-grain processes theory. Let  $\mathcal{T}$  be a tessellation of  $\mathbb{R}^d$ . If we denote by  $x_n$  the cell centers, then  $\{(x_n, \mathcal{C}_n)\}$  can be seen as a germ-grain process with convex grains. We call typical cell and we note  $\mathcal{C}^0$  the typical grain of the process. In an analogous manner, the

edges midpoints with their cooresponding edges form a germ-grain process. The advantage of this approach is that one can rely on results obtained for germ-grain processes to study a tessellation  $\mathcal{T}$ .

### Random tessellation in the plane

In this section, we try to illustrate the study of random mosaics for a planar tessellation. Thus, let  $\mathcal{T}$  be a tessellation on  $\mathbb{R}^2$ . The following mean values are of particular interest to characterize  $\mathcal{T}$ :

- $\theta_k$  : Intensity of the point process of the centroids of the  $k$ -faces induced by  $\mathcal{T}$  on  $\mathbb{R}^2$ .
- $\bar{\mathcal{A}}$  : Mean area of the typical cell.
- $\bar{\mathcal{P}}$  : Mean perimeter of the typical cell.
- $n_{jk}$  : Mean number of  $k$ -faces adjacent to the typical  $j$ -faces of  $\mathcal{T}$ .

**Proposition 1.7.2.** *The parameters of  $\mathcal{T}$  satisfy*

$$\theta_1 = \theta_0 + \theta_2 \quad (1.113)$$

$$n_{02} = 2 + 2\frac{\theta_2}{\theta_0}, \quad n_{20} = 2 + 2\frac{\theta_0}{\theta_2}, \quad (1.114)$$

$$\bar{\mathcal{A}} = \frac{1}{\theta_2}, \quad \mathcal{P} = 2\frac{\theta_1}{\theta_2}l_1, \quad (1.115)$$

$$n_{21} = n_{20}, \quad n_{01} = 3, \quad n_{10} = 2. \quad (1.116)$$

*In addition, if the tessellation  $\mathcal{T}$  is normal, then we have*

$$n_{02} = 3, \quad n_{20} = 6. \quad (1.117)$$

These relation are derived by considering the topological configuration of random mosaics. Some results are particularly obvious. For instance, it is clear that the number of neighbor vertices for a given edge is  $n_{10} = 2$ . Note that similar relations can be obtained in higher dimensions. We refer the reader to the book [Schneider and Weil, 2008] for a more extensive presentation of the theory and to the book [Chiu et al., 2013] for the case  $d = 3$ .

### 1.7.2 Poisson tessellation models

#### Poisson hyperplanes

A hyperplane is a subspace of one dimension less than its ambient space. For instance, if a space is 3-dimensional then its hyperplanes are the 2-dimensional planes. An affine hyperplane is an affine subspace of codimension 1 in an affine space. In Cartesian coordinates, an affine hyperplane  $H$  can be described with a single linear equation of the following form

$$u_1x_1 + u_2x_2 + \cdots + u_dx_d = r, \quad (1.118)$$

where  $\sum_i^d u_i^2 = 1$  and  $r \in \mathbb{R}$ . The vector  $u = (u_1, \dots, u_d)^T$  is orthogonal to  $H$  and unitary. We denote by  $\mathcal{A}$  the set of all affine hyperplanes of  $\mathbb{R}^d$ . An hyperplane is completely characterized by  $u$  and  $r$ , and can thus be considered as the image of these quantities by the application

$$\Psi : (u, r) \in \frac{1}{2}\mathbb{S} \times \mathbb{R} \rightarrow \mathcal{A} \ni H(u, r), \quad (1.119)$$

where

$$H(u, r) = \{x \in \mathbb{R}^d, u_1x_1 + u_2x_2 + \cdots + u_dx_d = r\}. \quad (1.120)$$

and  $\mathbb{S}$  is the unit semi-sphere of  $\mathbb{R}^d$ .

**Definition 1.7.2.** Let  $\mathcal{P}$  be a Poisson point process in  $\frac{1}{2}\mathbb{S} \times \mathbb{R}$  with intensity  $\theta(d\mathbf{u})dx$ , where  $\theta$  is a positive Radom measure on the semi-sphere  $\frac{1}{2}\mathbb{S}$ . The image of  $\mathcal{P}$  by application  $\Psi$  is the random closed set  $\mathcal{H}$  called Poisson hyperplanes network.

**Remark** One could have thought of relying on a classical Boolean model with lines as grains to construct Poisson hyperplanes. The problem with this approach is that lines are not bounded and therefore not compact.

**Theorem 1.7.3.** Let  $K$  be a compact set of  $\mathbb{R}^d$ . The number of hyperplanes hit by  $K$  is a Poisson random variable with intensity

$$\theta(K) = \int_{\frac{1}{2}\mathbb{S}} \nu_1(K|\mathbf{u})\theta(d\mathbf{u}). \quad (1.121)$$

In this expression,  $\nu_1(K|\mathbf{u})$  denotes the total length of the orthogonal projection of  $K$  on direction  $\mathbf{u}$ .

*Proof.* By construction, the intersection of  $\mathcal{T}$  with every line with unit support vector  $\mathbf{u}$  is a Poisson point process with intensity  $\theta(d\mathbf{u})$ . Hence, the number of hyperplanes hit by  $K$  for a given direction  $\mathbf{u}$  is  $\nu_1(K|_{\mathbf{u}})\theta(d\mathbf{u})$ .  $\square$

Using theorem 1.7.3, we can easily prove the following proposition.

**Proposition 1.7.4.** *The Choquet capacity of a Poisson hyperplanes network  $H$  is given for all compact sets  $K$  in  $\mathbb{R}^d$  by*

$$T(K) = 1 - \exp \left[ - \int_{\frac{1}{2}\mathbb{S}} \nu_1(K|_{\mathbf{u}})\theta(d\mathbf{u}) \right]. \quad (1.122)$$

### Poisson lines tessellations

Poisson hyperplanes can be used to produce random tessellations. In this section, we restrict ourselves to the plane  $\mathbb{R}^2$ .

**Definition 1.7.3.** *Let  $\mathcal{L}$  be a planar motion-invariant line process of intensity  $\theta$ .  $\mathcal{L}$  induces a stationary tessellation on  $\mathbb{R}^2$ , called Poisson line tessellation. The line intersections form the vertices of the tessellation, and segments of line with vertices at both endpoints form the edges.*

To characterize the tessellation, we introduce the quantity

$$\rho = \frac{2\theta}{\pi}, \quad (1.123)$$

which corresponds to the mean number of lines intersected by a test line segment of unit length. Let  $g$  be a fixed line of  $\mathcal{L}$ . Then, the intensity of the point process of intersection points on  $g$  is given by  $\rho$ . As a consequence, the mean edge length is

$$l_1 = \frac{1}{\rho} \quad (1.124)$$

With probability one, there are no triplets of lines that meet at the same vertex. Hence, we have

$$n_{02} = 4 \quad (1.125)$$

almost surely. Therefore, using proposition, we find

$$\theta_0 = \frac{\pi\rho^2}{4}, \quad (1.126)$$

$$\theta_1 = \frac{\pi\rho^2}{2}, \quad (1.127)$$

$$\theta_2 = \frac{\pi\rho^2}{4}. \quad (1.128)$$

**Definition 1.7.4.** *The typical cell of the Poisson hyperplane tessellation is called Poisson polygon.*

The first moments of Poisson polygon can easily be calculated with proposition, to find

$$\bar{\mathcal{A}} = \frac{4}{\pi\rho^2}, \quad (1.129)$$

$$\bar{\mathcal{L}} = \frac{4}{\rho}. \quad (1.130)$$

### 1.7.3 Poisson-Voronoi tessellations

We present in this section the Poisson-Voronoi tessellation model. This model has been studied extensively and is a classical model in stochastic geometry.

#### Definition

Let  $\Omega$  denote a given volume in  $\mathbb{R}^3$ . A Voronoi tessellation is a tessellation built from a Poisson point process  $\mathcal{P}$  in the space  $\mathbb{R}^3$ . Every point  $x$  of  $\mathbb{R}^3$  is associated to the class  $\mathcal{C}_i$  containing all points of  $\mathbb{R}^3$  closer from the point  $x_i$  of  $\mathcal{P}$  than from any other point of  $\mathcal{P}$ . Hence, the classes  $C_i, i = 1, \dots, N$  are defined by

$$C_i = \left\{ y \in \mathbb{R}^3, \forall j \neq i, \|x_i - y\| \leq \|x_j - y\| \right\}. \quad (1.131)$$

It can be shown that with probability one, Voronoi tessellations are normal and face-to-face. Voronoi tessellations are characterized by one single parameter, namely the intensity of the underlying point process. Thus, according to proposition, for a Voronoi tessellation in the plane, we have

$$\theta_2 = \theta, \quad (1.132)$$

$$\theta_0 = 2\theta, \quad (1.133)$$

$$\theta_1 = 3\theta, \quad (1.134)$$

where  $\theta_0$ ,  $\theta_1$  and  $\theta_2$  denote the intensities of the point processes constituted by the vertices, the edges center and the cell centers, respectively. Similarly, the mean area of a cell of the tessellation is

$$\bar{\mathcal{A}} = \frac{1}{\theta}. \quad (1.135)$$

These relations can be generalized for  $d > 2$ .

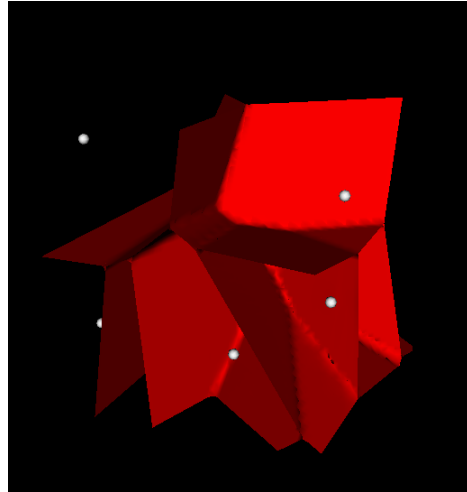


Figure 1.3: Voronoï tessellation in  $\mathbb{R}^3$ . The simulation has been obtained with the software VtkSim [Faessel and Jeulin, 2011]. The center of the Voronoï cells are represented in grey.

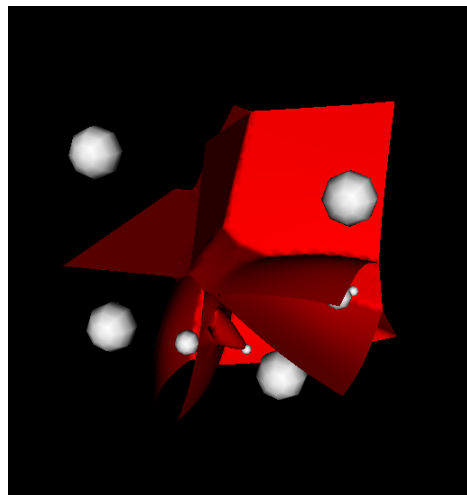


Figure 1.4: Voronoï tessellation in  $\mathbb{R}^3$ . The simulation has been obtained with the software VtkSim [Faessel and Jeulin, 2011]. The center of the tessellation cells are represented in grey. The first germs are represented with larger radii.

### Johnson-Mehl Tessellations

Johnson-Mehl tessellations can be seen as a sequential version of the Voronoï model, where the Poisson points are implanted sequentially with time. All classes grow then isotropically with the same rate, and the growth of crystal boundaries is stopped when they meet. All Poisson points falling in an existing crystal are removed. From a mathematical perspective, a Johnson-Mehl tessellation is constructed from a sequential Poisson point process where the points  $x_i, i = 1, \dots, N$  are implanted sequentially at a time  $t_i, i = 1, \dots, N$ . The classes  $C_i, i = 1, \dots, N$  corresponding to the points  $x_i, i = 1, \dots, N$  are defined by

$$C_i = \left\{ y \in \mathbb{R}^3, \forall j \neq i, t_i + \frac{\|x_i - y\|}{v} \leq t_j + \frac{\|x_j - y\|}{} \right\}. \quad (1.136)$$

Note that when all times are set to zero, we recover the classical Poisson-Voronoï tessellation model.

### Notes

Random tessellations constitute an active topic in stochastic geometry. Reference textbooks on this topic include [Matheron, 1975], [Chiu et al., 2013]. For an extensive presentation, we refer the reader to the book [Schneider and Weil, 2008], where a proof is given for almost all results. The mean-value relationships given in section 1.7.1 are mostly due to the studies [Mecke, 1980] and [Møller, 1989].

Poisson hyperplanes tessellations and Poisson polyhedra have been extensively studied in [Matheron, 1975], [Serra, 1982] and Miles [Miles, 1972]. We also refer the reader to the paper [Mecke, 1995].

The Voronoï tessellation is a classical model in stochastic geometry. A general description of Poisson-Voronoï tessellations in  $\mathbb{R}^d$  can be found in [Møller, 1989, 1994]. The Johnson-Mehl tessellation model was introduced by Johnson and Mehl to describe crystallization processes [Johnson and Mehl, 1939, Avrami, 1939, Gilbert, 1962]. Their model can be seen as a variation of the Voronoï model. The paper [Møller, 1992] provides a unified exposition of Random Johnson-Mehl tessellations.

# Chapter 2

## Morphological models in materials science

Most materials encountered in contemporary life and industrial applications are heterogeneous and characterized by complex internal microstructures. These microstructures play a central role in determining their macroscopic physical and mechanical properties [Torquato, 2002]. As a result, accurately modeling and reproducing material microstructures is a crucial step toward understanding and predicting material behavior at larger scales.

In this context, the generation of random microstructures that faithfully reproduce the geometrical characteristics of real materials has attracted considerable attention [Capasso, 2003, Ohser and Schladitz, 2009, Jeulin, 2021b, Torquato, 2002, Redenbach, 2009, Redenbach and Vecchio, 2011]. Such synthetic microstructures provide a powerful framework for investigating the physical and mechanical properties of heterogeneous materials through large-scale numerical simulations [Altendorf and Jeulin, 2011, Peyrega et al., 2011, Jeulin and Moreaud, 2006, Moreaud et al., 2012, Liebscher and Redenbach, 2013]. By enabling controlled variations of geometric features, this approach offers valuable insights into the relationship between microstructure and macroscopic material properties, with strong potential for both fundamental research and industrial applications.

This chapter presents selected research topics related to the simulation of material microstructures and, more broadly, to morphological modeling. Section 2.1 focuses on the development of microstructure models for a copper coating produced by the cold spray process, with the aim of investigating how the substrate microstructure influences electrical conduction at the macro-

scopic scale. We then address in section 2.2 a fundamental issue common to morphological models: once a model has been defined, how can its parameters be selected in a statistically consistent manner? To tackle this problem, we present an approach based on Markov Chain Monte Carlo algorithms, which provides an effective framework for parameter estimation in complex microstructural models. Finally, we discuss in section 2.3 an approach based on the resolution of the Eikonal equation to efficiently generate random tessellations.

## 2.1 Microstructure modelling with morphological models

We present in this section the development of a morphological model used for studying the electrical characteristics of a bi-phased coating produced through thermal spraying [Beauvais et al., 2008, Amsellem et al., 2008, Delloro et al., 2014]. This coating is specifically designed to shield recent commercial aircraft bodies from lightning strikes by providing a conductive surface that can effectively dissipate electrical charges. To our knowledge, this study represents one of the earliest efforts to model the electrical properties of coldspray deposits based on their microstructure. This research work was carried out in collaboration with Vincent Bortolussi, Michel Jeandin (Centre des matériaux, Mines Paris), François Willot and Matthieu Faessel (Centre de morphologie mathématique, Mines Paris) and was partially funded by a grant from Air Force Office of Scientific Research (AFOSR). It led to several publications related to the morphological model itself [Bortolussi et al., 2018] and to its exploitation to study the electric conductivity of冷spray coatings [Bortolussi et al., 2020].

### 2.1.1 Context

Modern commercial aircraft are constructed using carbon fiber-reinforced polymers, which provide excellent mechanical properties while being significantly lighter than traditional aluminum alloys. However, the polymer matrix in these materials is generally highly electrically insulating, which poses security concerns in the event of lightning strikes. Advanced aerospace composites are typically fabricated using a matrix of PEEK (Poly-Ether-Ether-Ketone), a thermoplastic polymer that offers good mechanical and thermal

properties while being an excellent insulator. To address the need for electrical charge dissipation in the event of lightning strikes, a layer of copper mesh is typically applied to the composite body. Copper is an easily machinable and corrosion-resistant electrical conductor with low electrical resistivity.

### 2.1.2 Experimental data

To simplify the manufacturing and assembly of copper meshing, a new coating method was developed, which relies on copper powder being thermally sprayed onto composite parts. Specifically, an adherent and electrically conductive layer is achieved by using a powder mixture containing 80% volumetric of spherical copper powder (10-35 microns) and 20% of irregular PEEK particles (35-65 microns). The mixture is applied using the cold-gas dynamic spraying or “cold spray” process.

In our work, we relied on microscopic images of the coating to study the resulting microstructure. Prior to observation, the cold spray coatings underwent cross-sectioning and polishing. To do this, the coating samples were cut in two directions: along the spraying path and orthogonal to it. Unfortunately, cutting and polishing caused debonding of the copper particles due to poor mechanical anchorage in the matrix. This resulted in dark holes at the surface. It should be noted that manual polishing can have a significant impact on the debonding phenomenon. To counteract this, the samples were metallized with a layer of Gold-Palladium that was only 2 nm thick, using a Cressington sputter coater. This was a crucial step as the layer modified the color of the PEEK matrix, greatly enhancing the color gradient between phases. To observe the cross-sections, we used a Leica optical microscope at  $\times 20$  magnification in bright field. The microscope had a resolution of 0.2428 microns per pixel. We selected this observation scale to obtain a representative fraction of copper while also highlighting PEEK interstices.

The microstructure of the cold spray coating can be observed in Fig. 2.1, where yellow copper particles are embedded in a grey PEEK matrix that contains dark footprints. The matrix is made up of irregular PEEK particles that become highly deformed upon high speed impact, resulting in a dense structure with no visible pores at this scale. The copper particles deform only upon impact with each other, resulting in limited plastic strain and forming a network of copper clusters. In typical cold spraying of metal particles onto a metal substrate, chemical bonding and inter-diffusion occur at the interfaces between particles and substrate. However, in our case,

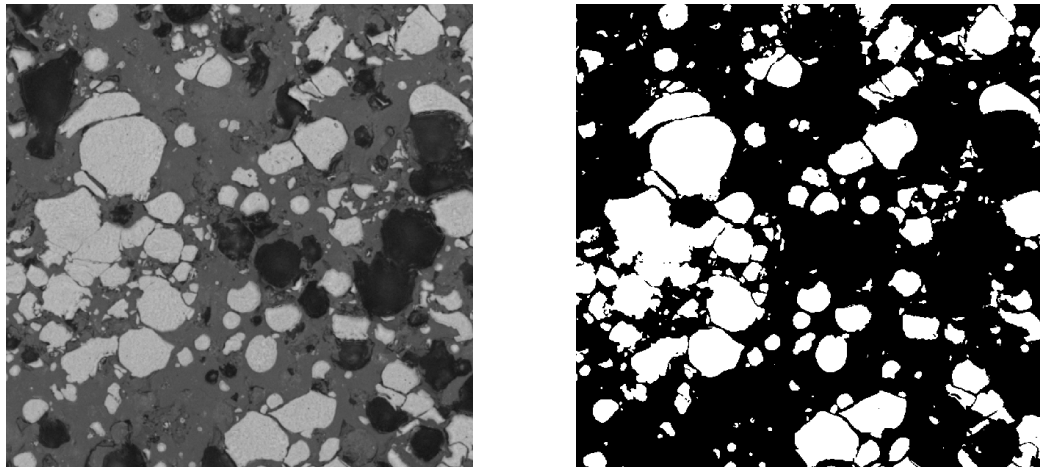


Figure 2.1: Original image and corresponding segmentation mask.

optical observation at a larger scale highlights thin PEEK layers are lying between deformed copper particles, as shown in Fig. 2.1. These interstices prevent direct contact between copper particles and are filled with electrically insulating PEEK, allegedly increasing resistivity and thus lowering the conductivity of the coating. Fig. 2.2 is an optical microscope cross-section of the coating microstructure with debonded particles appearing in black. The image comprises  $2560 \times 1920$  pixels representing a surface area of  $620 \times 476 \mu\text{m}^2$ . Fig. 2.2 is a magnified optical microscope cross-section of the coating's microstructure, with the image comprising  $2560 \times 1920$  pixels representing a surface area of  $248 \times 186 \mu\text{m}^2$ .

The first step of our study consisted in developing a segmentation algorithm of the experimental images in order to identify the copper particles within the microstructures as well as the interstices separating these particles. We refer the reader seeking additional details on the segmentation algorithm to the original article [Bortolussi et al., 2018]. Segmentation results are displayed in Fig. 2.1. Overall, we performed the segmentation of  $K = 13$  large images of the microstructure, and we used these images to compute experimental covariance and granulometry curves that characterize the coating microstructure.

### 2.1.3 Morphological model

We present in this section the multi-scale morphological model [Jeulin, 2012] developed for describing the microstructure geometry. To construct the model, we make the assumption that the microstructure consists of copper spheres embedded in a PEEK matrix, separated by thin PEEK interstices. The covariance, copper fraction, granulometry, and interstice thickness are measured on 2D slices of the coating. Therefore, the parameters of the 3D model need to be inferred from this 2D information. The final two-scale model is based on a two-step simulation process:

1. The first step of the simulation process corresponds to the generation of a Boolean model of spheres with intensity  $\theta$ . The radii of the spheres follow a Gamma distribution law with parameters  $\lambda$  and  $a$ . This first scale of the model intends to represent the set of copper particles, which form aggregates due to interpenetration.
2. The second step involves interstice implantation based on a modified Johnson-Mehl tessellation. This two-scale model provides a representation of the 3D microstructure of the coating based on the 2D information obtained from the slices.

**Aggregates simulation** We assume that the copper particles aggregates can be represented by a Boolean model of spheres and that the distribution of the radii of the spheres is described by a Gamma law. The probability density function of the Gamma law is given by

$$p(r, \lambda, a) = \frac{r^{a-1}}{\Gamma(a)\lambda^a} \exp\left(-\frac{r}{\lambda}\right), \quad (2.1)$$

where  $\Gamma$  denotes the Gamma function. The average radius of the typical sphere is  $a\lambda$ . Its variance is  $a\lambda^2$ . The average surface of the typical grain is

$$S_v = \int_0^{+\infty} \frac{4\pi r^{a+1}}{\Gamma(a)\lambda^a} \exp\left(-\frac{r}{\lambda}\right) dr = 4\pi\lambda^2 a(a+1). \quad (2.2)$$

Similarly, its average volume is

$$V_v = \int_0^{+\infty} \frac{4\pi r^{a+2}}{3\Gamma(a)\lambda^a} \exp\left(-\frac{r}{\lambda}\right) dr = \frac{4\pi}{3}\lambda^3 a(a+1)(a+2). \quad (2.3)$$

To determine the 3D parameters of the model using 2D measurements, we use the stereological formulae

$$\theta_3 V_v = \theta_2 \bar{A}, \quad \theta_3 S_v = \frac{4}{\pi} \theta_2 \bar{L}, \quad (2.4)$$

where  $\bar{A}$  is the mean area of the sliced spheres,  $\bar{L}$  their perimeter,  $\theta_3$  the 3-dimensional intensity parameter and  $\theta_2$  the intensity of the disk process on sections. We need to relate the 2D measurements to the parameters of the Boolean model. To that end, we rely on Miles' formulae [Miles, 1972, Chiu et al., 2013, Schneider and Weil, 2008], discussed in chapter 1:

$$A_a = 1 - e^{(-\theta_2 \bar{A})}, \quad L_a = \theta_2 \bar{L}(1 - A_a), \quad (2.5)$$

where  $A_a$  is the mean surface fraction of copper on segmented images and  $L_a$  is the mean perimeter of the copper phase on segmented images divided by the total surface. Using Miles' formulae in conjunction with stereological formulae [Chiu et al., 2013, Schneider and Weil, 2008], we find, for the Boolean model

$$\mathcal{A}_a = 1 - \exp(-\theta V_v), \quad \mathcal{L}_a = \theta \frac{\pi}{4} S_v \exp(-\theta V_v). \quad (2.6)$$

Overall, there are three unknowns in the model, namely the intensity  $\theta$  of the Boolean model and the parameters  $a$  and  $\lambda$  of the Gamma distribution. Hence, we can express all parameters as functions of  $a$ . Using (2.6), we find

$$\theta = -\frac{3}{4\pi\lambda^3 a(a+1)(a+2)} \ln(1 - \mathcal{A}_a), \quad (2.7)$$

and

$$\lambda = -\frac{3\pi}{4(a+2)\mathcal{L}_a} (1 - \mathcal{A}_a) \ln(1 - \mathcal{A}_a). \quad (2.8)$$

To determine the parameters of the stochastic model, we rely on a maximum likelihood approach to find the parameters that minimize the least-square distance between the covariance of the simulated microstructure and the covariance that is measured on the available experimental dataset. However  $\mathcal{L}_a$  is highly influenced by interconnection between particles. As many particles remain in contact due to interstices segmentation, computing  $\theta$  only from  $\lambda$  and  $a$  provides a more robust algorithm.

**Interstices implantation** To simulate the interstices between the particles of the same aggregate, we use a random Johnson-Mehl tessellations restricted to each aggregate, or connected component of the first scale of the microstructure. For each connected aggregate  $\mathcal{A}$  of the first scale of the simulation, we consider  $n$  germs and we simulate a random number  $\zeta_n$  according to an exponential law with some mean  $k$ , which will parameterize the thickness of the boundary between cells. The cells of the tessellation are then defined by

$$C_i = \left\{ y \in \mathcal{A}, \forall j \neq i, t_i + \frac{\|x_i - y\|_G}{v} + \zeta_i \leq t_j + \frac{\|x_j - y\|_G}{v} \right\}. \quad (2.9)$$

In this relation,  $\|\cdot\|_G$  denotes the geodesic distance with respect to the realization of the Boolean model and  $t_i$  is the implantation time of the  $i$ -th grain. With this definition, we note that some points of the aggregates do not belong to any class of the Johnson-Mehl tessellation. We consider that these points form the interstices between the grains of the microstructure.

A significant question remains, which is how to select the initial germs of the tessellation and the germination times. While selecting the germs, our aim is to preserve the geometrical shape of the grains of the microstructure. Hence, we seek to set the germs in the center of connected components to simulate a granular microstructure. To the end, we rely on the *h-maxima* [Serra, 1982] of the distance function to generate the germs. The *h-maxima* of the distance function form connected components. For each component, we select its barycentre to be the location of a germ. The threshold for the *h-maxima* is selected after an optimization procedure that aims at minimizing the distance between the granulometries. For each germ  $n$ , we denote by  $d_n$  the value of the Euclidean distance function at the location of the germ. The germination time associated to germ  $n$  is defined to be

$$t_n = (\max_m d_m) - d_n. \quad (2.10)$$

With this choice of germination time, the cells border of bigger spheres are kept close from the edges of the spheres and we are able to preserve the geometrical shape of the grains constituting the microstructure.

#### 2.1.4 Results and discussions

To assess the relevance of the proposed stochastic model, we compared several morphological descriptors between experimental and simulated microstruc-

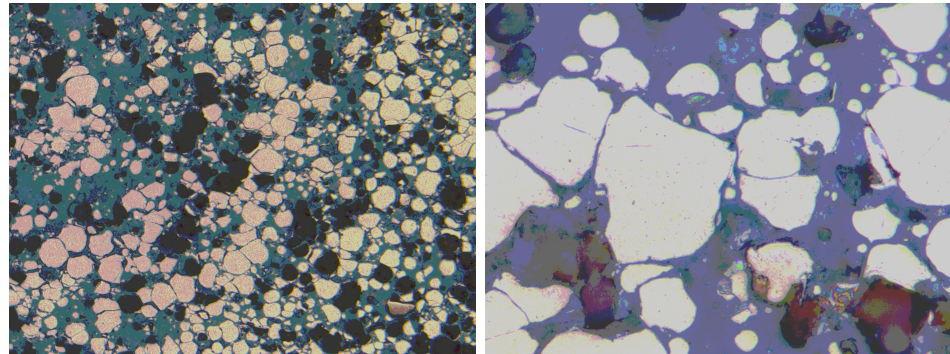


Figure 2.2: Optical microscope cross-section of the coating ( $2560 \times 1920$  pixels representing a surface area of  $248 \times 186 \mu\text{m}^2$ ).

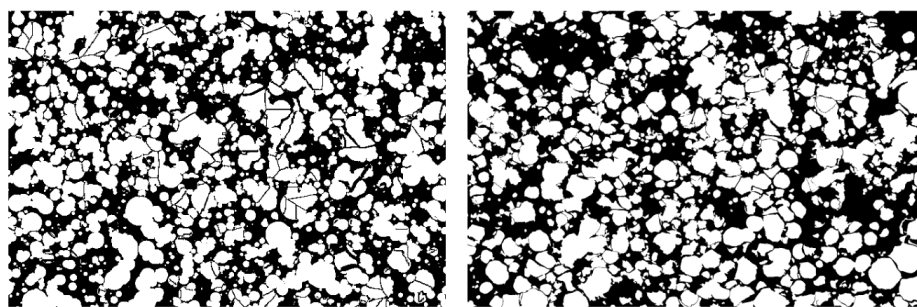


Figure 2.3: Simulation of the microstructure with the optimized parameters.

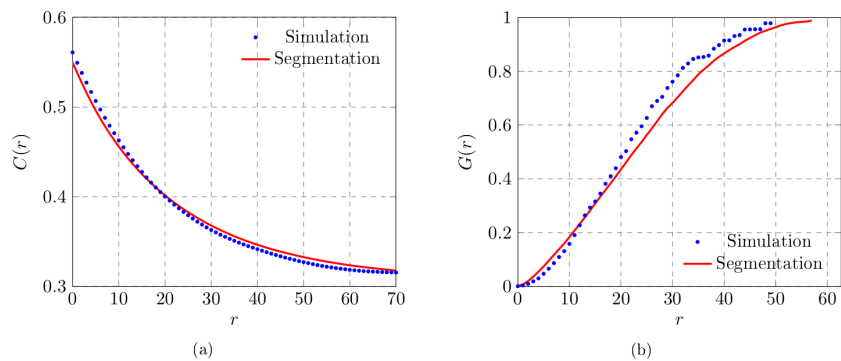


Figure 2.4: Simulated and experimental microstructures comparisons between covariances (a) and granulometries (b).

tures. These descriptors include the covariance function, the granulometry, and the interstice thickness distribution. The combined use of covariance and granulometry is common in morphological modeling, as the granulometry characterizes object size distributions while the covariance provides second-order statistics related to spatial organization and scale superposition. The interstice thickness distribution is a key feature specific to the present study. Owing to the strong electrical resistivity contrast between copper and PEEK, even small variations in interstice size can significantly affect the macroscopic electrical conductivity of the coating.

Table 2.1: Model parameters.

$A_a$	$\theta (\mu\text{m}^{-3})$	$\lambda (\mu\text{m})$	$a$	$k (\mu\text{m})$	$h (\mu\text{m})$	$p$
63%	$4.8 \times 10^{-3}$	2.3	0.8	1.2	7.26	0.5

Figure 2.3 presents a two-dimensional slice of a simulated microstructure obtained using parameters estimated through the maximum likelihood procedure. The corresponding parameter values are reported in Table 2.1, where  $A_a$  denotes the copper surface fraction measured on segmented images,  $\theta$  the intensity of the Poisson point process,  $\lambda$  and  $a$  the parameters of the Gamma distribution governing particle radii,  $h$  the threshold used to extract distance-function maxima, and  $p$  the proportion of selected maxima.

Comparisons between experimental and simulated covariances and granulometries are shown in Fig.2.4. We can note that a small discrepancy, on the order of 0.01, appears in the covariance for distances between 10  $\mu\text{m}$  and 40  $\mu\text{m}$ . This difference is attributed to the presence of a few relatively large polymer-rich regions devoid of copper particles, which can be observed in Fig. 2.2.

### 2.1.5 Conclusion

In this section, we developed a two-scale stochastic morphological model to describe the three-dimensional microstructure of cold spray copper-PEEK coatings from two-dimensional experimental observations. The model combines a Boolean model of spheres with Gamma-distributed radii to represent copper particle aggregates, and a modified Johnson-Mehl tessellation to account for the thin PEEK interstices separating particles within aggregates. Model parameters were inferred from stereological relations and optimized by

matching covariance and granulometry descriptors measured on segmented experimental images.

Comparisons between simulated and experimental microstructures show good agreement in terms of covariance and granulometry, indicating that the proposed model successfully captures both the spatial organization and the size distribution of copper particles. The inclusion of interstice implantation proves essential for reproducing realistic microstructural features that strongly influence electrical transport properties. This morphological framework therefore provides a consistent and physically grounded basis for subsequent numerical simulations of the effective electrical conductivity of cold spray coatings.

## 2.2 Parameters estimation in morphological models

We presented in the previous section a morphological model designed to reproduce the microstructure of cold-spray-deposited materials from experimental imaging data. Morphological models typically rely on a set of parameters, denoted by  $\Theta$ , which must be carefully selected to ensure consistency with experimental observations. A common strategy for determining these parameters consists in minimizing an objective function, usually defined as a measure of discrepancy between quantities obtained from numerical simulations and those measured experimentally. Numerous approaches have been proposed in the literature to address this optimization problem.

A classical technique involves minimizing the objective function using a gradient descent algorithm. Gradient descent methods are first-order iterative optimization algorithms that aim to locate a local minimum of a differentiable function by iteratively moving in the direction of the negative gradient in parameter space. While these algorithms are highly effective for strongly convex problems, their application to morphological models raises several difficulties. First, the gradient of the objective function is often analytically intractable and must be approximated using finite-difference schemes. This approximation requires at least  $D + 1$  evaluations of the objective function, where  $D$  denotes the dimension of the parameter space, and is further affected by the intrinsic statistical variability of morphological models, which typically leads to noisy gradient estimates. Second, the objective function is

## 2.2. PARAMETERS ESTIMATION IN MORPHOLOGICAL MODELS 61

generally non-convex, so gradient-based methods are prone to converging to local minima.

Several alternatives to gradient descent have been proposed in the literature. In particular, in [Wang et al., 2015, 2017, 2018, Figliuzzi et al., 2016], the authors advocate the use of the Nelder-Mead algorithm, a heuristic optimization method for locating extrema of an objective function in a multidimensional space. As a direct search method based solely on iterative evaluations of the objective function, it is well suited to situations in which gradient information is unavailable or unreliable.

In this section, we address the relatively underexplored problem of parameter estimation for morphological models. We introduce an approach based on a Bayesian formulation of the problem, originally proposed in [Figliuzzi et al., 2021]. This framework yields a posterior distribution for the model parameters conditioned on the experimental observations. Samples from this posterior distribution are generated using a Markov Chain Monte Carlo (MCMC) algorithm. Compared to deterministic optimization methods, this approach offers several advantages: in particular, MCMC sampling provides a faithful representation of the posterior distribution, enables the identification of correlations between model parameters, and allows for a quantitative assessment of their respective influences.

### 2.2.1 Problem statement

Let us consider a set of previously segmented experimental images of a material's microstructure, which we denote as the observations  $\mathcal{O}$ . The geometry of the microstructure can be characterized by computing several statistical features, including the covariance, the granulometry, or the granulometry of the complementary image.

The covariance of a random set  $A$  was defined in Chapter 1 as the function  $C_A$  on  $\mathbb{R}^d \times \mathbb{R}^d$  given by

$$C_A(x, x + h) = P(x \in A, x + h \in A), \quad (2.11)$$

where  $h \in \mathbb{R}^d$ . For a stationary random set, the covariance depends only on the displacement  $h$ :

$$C_A(x, x + h) = C_A(h). \quad (2.12)$$

Next, we consider the granulometry of the microstructure. Let  $K$  be a convex set, and let  $(K_\lambda, \lambda > 0)$  denote a family of scaled structuring elements,

where  $K_\lambda = \lambda K$ . For any closed set  $A \subset \mathbb{R}^d$ , the operator

$$\Phi_\lambda(A) = (A \ominus \check{K}_\lambda) \oplus K_\lambda, \quad (2.13)$$

defines a granulometry, where  $\ominus$  denotes morphological erosion and  $\oplus$  denotes morphological dilation.

The granulometry obtained by openings characterizes the size distribution of the elements of  $A$ . Specifically, for distinct values of  $\lambda$ , one can record the volume fraction of the residual set

$$A \setminus \Phi_\lambda(A),$$

to quantify the size distribution. In this work, granulometry measurements are computed both on the set  $A$  and on its complement  $A^c$ .

In the remainder of this section, we denote by  $m_{\mathcal{O}}$  the statistical measurements derived from the observations and by  $m_{\Theta}$  those obtained from simulated microstructures. The model parameters  $\Theta$  are typically chosen to minimize the discrepancy between  $m_{\mathcal{O}}$  and  $m_{\Theta}$ . This parameter estimation can be formulated as the following constrained optimization problem:

$$\hat{\Theta} := \arg \min_{\Theta} \|m_{\mathcal{O}} - m_{\Theta}\|_2^2 \quad \text{subject to } \Theta \in \mathcal{D}, \quad (2.14)$$

where  $\mathcal{D}$  denotes the set of admissible model parameters.

### 2.2.2 Bayesian formulation

Starting from measurements obtained from a morphological model and from experimental observations of the studied microstructure, we use a Bayesian approach to determine the parameters of the model. The likelihood that the observations were obtained with the set of parameters  $\Theta$  can be defined as follows:

$$p(\mathcal{O}|\Theta) = \frac{1}{\sqrt{2\pi|\Lambda|}} \exp\left(-\frac{1}{2}(m_{\mathcal{O}} - m_{\Theta})^T \Lambda^{-1} (m_{\mathcal{O}} - m_{\Theta})\right), \quad (2.15)$$

In Eq. (2.15), we usually consider a diagonal covariance matrix  $\Lambda$  and we assign a weight to the parameters corresponding to their respective importance. The arbitrary choice of a Gaussian distribution is motivated by its simplicity, but other distributions could potentially be considered for the likelihood.

We resort to physical considerations to define a prior distribution on the parameters  $\Theta$ . Usually, we are able to define a range of variation for all parameters of the model based on their physical validity:

$$\Theta_{\min} \preceq \Theta \preceq \Theta_{\max}, \quad (2.16)$$

where  $\preceq$  is a component-wise inequality. We simply consider a uniform distribution between the lower and the upper bound for each parameter as prior distribution:

$$p(\Theta) := \mathcal{U}_{\Theta_{\min}, \Theta_{\max}}. \quad (2.17)$$

Thanks to Bayes formula, we obtain an expression for the posterior distribution of the parameters  $\Theta$  knowing the observations:

$$p(\Theta|\mathcal{O})p(\mathcal{O}) = p(\mathcal{O}|\Theta)p(\Theta). \quad (2.18)$$

Since the (unknown) probability law for the observation is independent from  $\Theta$ , the posterior distribution is proportional to the product of the likelihood and of the prior distribution:

$$p(\Theta|\mathcal{O}) \propto p(\mathcal{O}|\Theta)p(\Theta). \quad (2.19)$$

The problem of the model parameterization becomes the determination of a set of parameters maximizing the posterior probability  $p(\Theta|\mathcal{O})$ :

$$\hat{\Theta} = \operatorname{argmax}_{\Theta} p(\Theta|\mathcal{O}). \quad (2.20)$$

### 2.2.3 Sampling from the posterior distribution

A question now arises, which is how to solve the optimization problem from Eq. (2.20) in practice? An obvious solution could be to use a gradient ascent algorithm to find local maxima in the parameters space. In this section, we propose a distinct approach consisting in using a Monte Carlo Markov Chains (MCMC) algorithm to generate samples from the posterior distribution [Robert et al., 1999, Andrieu et al., 2003]. This approach offers several benefits compared to gradient ascent. Computing the gradient of the measurements with respect to the parameters is often challenging due to two primary factors. Firstly, there is usually no readily available analytical formula to calculate the gradient. Secondly, the function  $m_\Theta$  is a stochastic function dependent on the parameter set  $\Theta$ , making it difficult to estimate the

gradient using a finite difference scheme. Moreover, the MCMC approach possesses an additional advantage as it enables the generation of samples that accurately represent the posterior distribution. This capability allows for the capture of noteworthy characteristics of the microstructure, including parameter correlations and characteristic ranges of parameter variation. The algorithm that we propose works as follows:

- *Initialization:* At initialization, we first generate a set of parameters from the prior distribution:

$$\Theta_1 \sim \mathcal{U}_{\Theta_{\min}, \Theta_{\max}}. \quad (2.21)$$

- *n-th iteration:* At each iteration, we repeat the following steps:

1. *Parameters sampling* we generate a set of parameters  $\hat{\Theta}$  from the current state  $\Theta_n$  according to a proposal distribution  $q$ :

$$\hat{\Theta} \sim q(\hat{\Theta}|\Theta_n) \quad (2.22)$$

2. *Simulation* We compute a simulation of the morphological model with this set of parameters, and perform measurements on the computed microstructure. The measurements  $m_{\hat{\Theta}}$  are used to compute the posterior distribution, up to the constant factor  $p(\mathcal{O})$ :

$$p(\hat{\Theta}|\mathcal{O}) \propto p(\mathcal{O}|\hat{\Theta})p(\hat{\Theta}). \quad (2.23)$$

3. *Accept/reject step* We compute the so-called Hastings ratio  $r$ , defined by:

$$r = \min \left( 1, \frac{p(\hat{\Theta}|\mathcal{O})q(\Theta_n|\hat{\Theta})}{p(\Theta_n|\mathcal{O})q(\hat{\Theta}|\Theta_n)} \right) \quad (2.24)$$

Noteworthy, the Hastings ratio  $r$  is independent of the quantity  $p(\mathcal{O})$ . The new set of parameters  $\hat{\Theta}$  is accepted or rejected with probability  $r$ :

$$\Theta_{n+1} = \begin{cases} \hat{\Theta} & \text{if } u < r \\ \Theta_n & \text{otherwise} \end{cases} \quad (2.25)$$

where  $u$  is a random variable sampled from the uniform distribution  $\mathcal{U}(0, 1)$ .

### 2.2.4 Numerical experiments

#### Experiments on synthesized random sets

To illustrate our methodology, we consider two examples of microstructures generated with morphological models. Our objective is to recover the parameterization of these models from statistical measurements conducted on realizations of the models. To that end, for each example, we generate a set of  $N = 10$  random microstructures in a domain of size 30 by 30 in  $\mathbb{R}^2$ .

- The first model corresponds to a Boolean model of disks with constant radii  $R = 0.5$  and with intensity  $\theta = 0.45$ .
- The second model corresponds to a Cox-Boolean model of disks corresponding to a two scales microstructure, with the first scale consisting in exclusion zones that remain empty of any inclusions, modeled by a Boolean model of disk with constant radii  $R_e = 1$  and intensity  $\theta_e = 0.1$ . The second scale simulates inclusions located in the complementary of the exclusion zones. The inclusions are described by a Boolean model of disks with intensity  $\theta = 0.45$  and radii sampled according to a normal distribution with mean  $R = 0.5$  and standard deviation 0.1.

Realizations of both morphological models are displayed in Fig. 2.5. To obtain a set of measurements  $m_{\mathcal{O}}$  for each morphological model, we averaged the covariance, the granulometry and the granulometry of the complementary as computed on 10 model realizations.

The upper and lower bounds for the parameters used to define the prior distribution are indicated in table 2.2 for the Boolean model and in table 2.3 for the Cox-Boolean model. We consider the same diagonal covariance matrix  $\Lambda$  in the likelihood function (2.15) for both morphological models. To put more emphasis on the correlations at the smallest scales, we employ the following expression for the diagonal coefficients of  $\Lambda$ :

$$\Lambda_{n,n} = \lambda \left(1 + \frac{1}{n}\right)^{-1}, \quad (2.26)$$

where  $\lambda = 0.1$ . Next, we initialize the Metropolis-Hastings algorithm by sampling a first set of parameters  $\Theta_1 := (\theta_1, R_1)$  from the prior distribution. At each step of the algorithm, the proposal distribution for each parameter is the truncated normal distribution:

$$q(\theta|\theta_n) = \mathcal{N}_{tr}(\theta_n, \sigma_\theta, \theta_{min}, \theta_{max}), \quad (2.27)$$

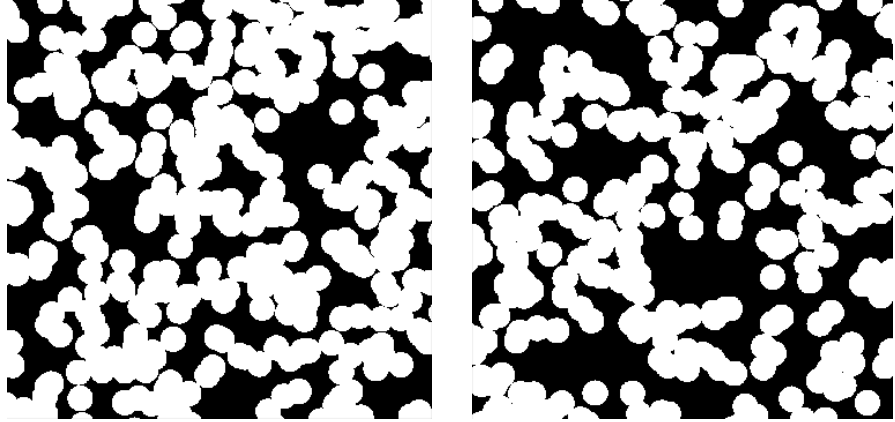


Figure 2.5: Sample of the microstructure generated with the Boolean model of disks (left) and with the Cox-Boolean model (right).

where  $\theta_{min}$  (resp.  $\theta_{max}$ ) is the minimal (resp. maximal) possible value of the parameter as established for defining the prior distribution, and the standard deviation  $\sigma$  is set to:

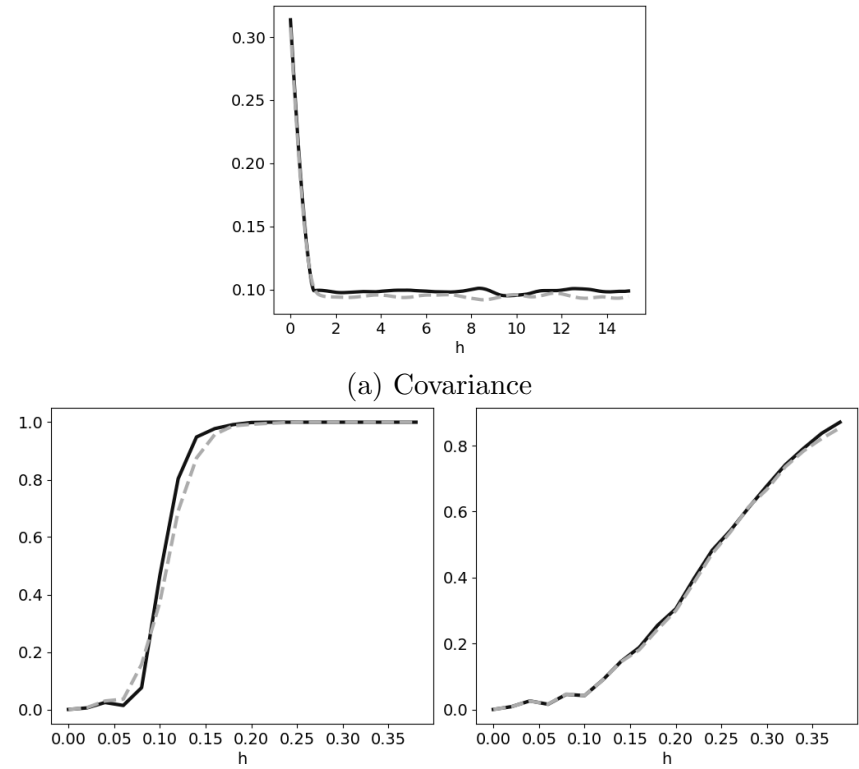
$$\sigma_\theta = \frac{\theta_{max} - \theta_{min}}{\Delta}. \quad (2.28)$$

We fix  $\Delta = 20$  to get an acceptance rate of 0.3 in the algorithm.

We stop the algorithm after 500 iterations, and we discard the first 100 parameters sampled by the algorithm, as they remain highly dependent on the initial conditions. Finally, we estimate the set of optimal parameters for the microstructure by considering the maximal a posteriori (MAP) value found for the sampled parameters:

$$\hat{\Theta} := \arg \max_{n=100, \dots, 500} p(\Theta_n | \mathcal{O}). \quad (2.29)$$

**Results and discussion** The optimal set of parameters  $\hat{\Theta}$  found by the Metropolis-Hastings algorithm are displayed in Tab. 2.2 for the Boolean model of disks, along with the standard deviation of the sampled parameters, and in Tab. 2.3 for the Cox-Boolean model. The standard deviation provides valuable information about the sensitivity of the parameters: if a parameter has experienced only minor variations throughout the iterations of the algorithm, it implies that when this parameter deviates from its optimal value, there is a substantial deviation from the targeted measurements. In



(b) Granulometry measurements of the microstructure (left) and of the complementary (right)

Figure 2.6: Comparison between the experimental measurements and the measurements obtained with simulations conducted with the MAP parameters identified by the MCMC algorithm for the Boolean model of disks .

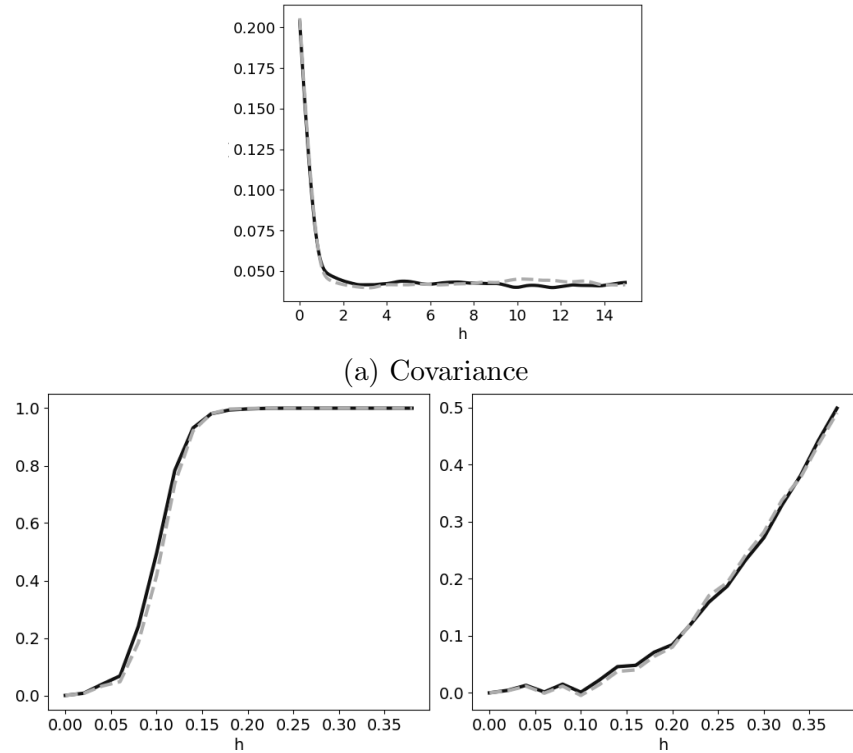


Figure 2.7: Comparison between the experimental measurements and the measurements obtained with simulations conducted with the MAP parameters identified by the MCMC algorithm for the Cox-Boolean model of disks.

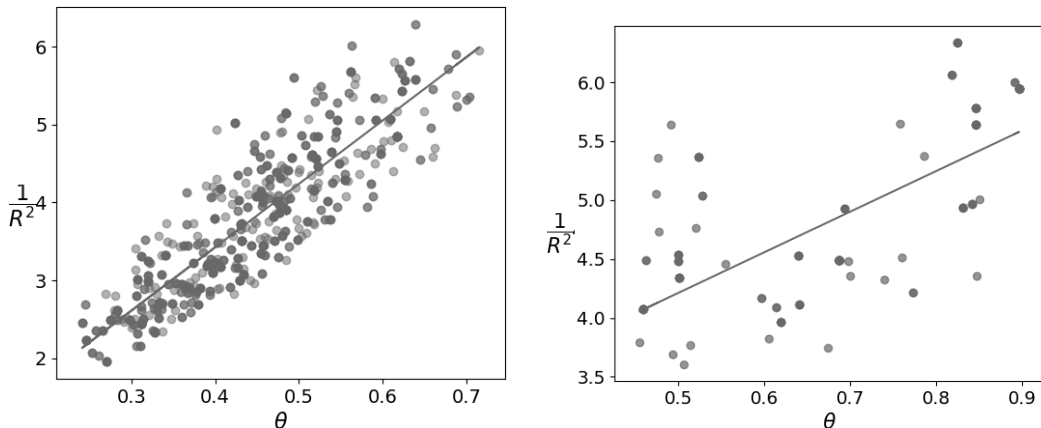


Figure 2.8: Scatterplot of the parameters  $1/R^2$  and  $\theta$  sampled by the Metropolis-Hastings algorithm for the Boolean model of disks (left) and for the Cox-Boolean model (right). The color intensity of each point corresponds to the frequency of the corresponding parameters within the samples.

	$\theta [L^{-1}]$	$R [L]$
Target	0.45	0.5
$\hat{\Theta}$	$0.44 \pm 0.05$	$0.52 \pm 0.025$
Min. Val.	0.2	0.15
Max. val.	0.9	1.05

Table 2.2: Optimal parameters found by the Metropolis-Hastings algorithm for the Boolean model of disks.

other words, even small changes in the parameter can have a significant impact on the agreement between the predicted measurements and the desired outcome. Overall, we can note that there is a good agreement between the parameters identified by the algorithm and the ones corresponding to the experimental microstructure. A comparison between the measurements as conducted on the target microstructures simulated with both morphological models and as obtained with the optimal set of parameters  $\hat{\Theta}$  is displayed in Fig. 2.6 and 2.7. Again, we note a fairly good agreement between the measurements.

Fig. 2.8 displays a scatterplot of the parameters sampled by the Metropolis-Hastings algorithm for both morphological models. Interestingly, we note that the parameters  $\theta$  and  $R$  sampled by the algorithm are strongly cor-

	$\theta_e [L^{-1}]$	$R_e [L]$	$\theta [L^{-1}]$	$R$
Target	0.1	1.	0.45	0.5
$\hat{\Theta}$	0.13	0.85	0.45	0.5
Std. Dev.	0.03	0.25	0.05	0.04
Min. Val.	0.05	0.5	0.2	0.15
Max. val.	0.2	2.	0.9	1.05

Table 2.3: Optimal parameters found by the Metropolis-Hastings algorithm for the Cox-Boolean model of disks.

related in the case of the Boolean model of disks. We performed a linear regression between the parameters  $\theta$  and  $1/R^2$ , to find a coefficient of determination equal to 0.81. For a Boolean model of disks, the volume fraction  $v$  is known to be given by

$$v = 1 - \exp(\pi R^2 \theta). \quad (2.30)$$

This leads to the linear relationship

$$\frac{1}{R^2} = -\frac{\pi}{\log(1-v)} \theta. \quad (2.31)$$

The covariance measurements are highly sensitive to the volume fraction. Hence, by construction, the Metropolis-Hastings will usually select a set of parameters that allows to obtain a volume fraction similar to the one measured on the experimental samples. As evidenced in Fig. 2.8 , the parameters are indeed distributed around a straight line. For the Cox-Boolean model, we note that the parameters  $\theta$  and  $R$  sampled by the algorithm remain correlated, but the correlation is less obvious than for the Boolean model. A linear regression performed between the parameters  $\theta$  and  $1/R^2$  yields a coefficient of determination equal to 0.51. Due to the presence of exclusion zones in the microstructure, Eq. (2.31) is not valid anymore, which explains this reduced correlation.

### Experiments on experimental materials

In this section, we demonstrate the application of our proposed optimization approach to investigate an experimental microstructure. The microstructure under examination consists of pigments embedded in a matrix, forming a

## 2.2. PARAMETERS ESTIMATION IN MORPHOLOGICAL MODELS 71

colloid film. These pigments possess an elongated ellipsoidal shape similar to that of a needle. To capture the microstructure for analysis, a dataset of experimental images was acquired using transmission electron microscopy (TEM) imaging. Figure 2.10 provides an illustrative example of one such TEM image. The analysis of the experimental TEM images reveals a noticeable tendency of the pigments to aggregate within the microstructure, resulting in the formation of clusters. These clusters exhibit a characteristic size that significantly exceeds the individual pigment size.

To describe the microstructure, we use a two-scale model as follows:

- The first scale of the simulation describes the pigments aggregates through a Boolean model of inclusion spheres characterized by two parameters, namely the intensity  $\theta_i$  of the Poisson point  $\mathcal{P}$  process used to construct the Boolean model and the radii  $R_i$  of the spheres.
- The second scale of the model simulates the pigments within the aggregates using a Boolean model of ellipsoids whose largest semi-axis follows a normal law with mean  $L$  and standard deviation  $\sigma_L$ , and whose smallest semi-axes follow a normal law with mean  $l$  and standard deviation  $\sigma_l$ . A hardcore distance  $h$  is introduced in the underlying point process. Ellipsoids are implanted at locations sampled from a Poisson point process with intensity  $\theta$  restricted to the set constituted by the spheres constitutive of the first scale of the model. Ellipsoids belonging to the same inclusion sphere share the same orientation, sampled uniformly from Euler's angles.

$\theta_i$ ( $\mu\text{m}^{-3}$ )	$R_i$ ( $\mu\text{m}$ )	$\theta$ ( $\mu\text{m}^{-3}$ )	$L$ ( $\mu\text{m}$ )	$l$ ( $\mu\text{m}$ )	$h$ ( $\mu\text{m}$ )
0.56	0.54	45.	$0.56 \pm 0.08$	$0.07 \pm 0.01$	0.2

Table 2.4: Optimal parameters for the "needles" microstructure.

The description of the microstructure model requires eight parameters. These parameters include the intensity  $\theta_i$  of the Poisson point process for the aggregates, their radius  $R_i$ , the lengths of the semi-axes  $L$  and  $l$  of the pigments, along with their corresponding standard variations  $\sigma_L$  and  $\sigma_l$ , the intensity  $\theta$  of the point process used for the pigments and the hardcore distance  $h$ .

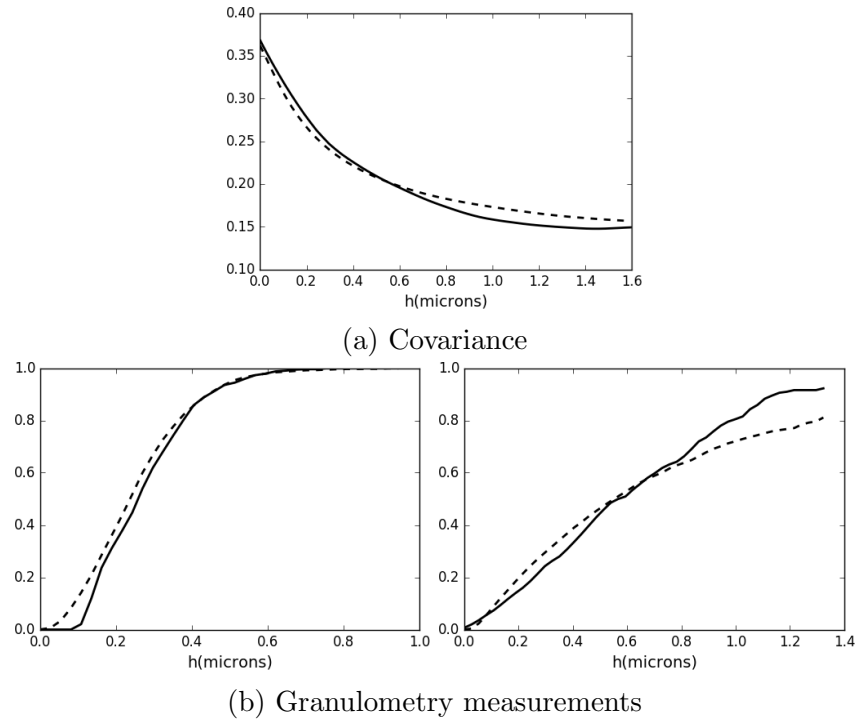


Figure 2.9: Comparison between the covariance and the granulometries as obtained on the experimental TEM images (dashed lines) and on the simulated TEM images for the "needles" microstructure [Figliuzzi et al., 2021].

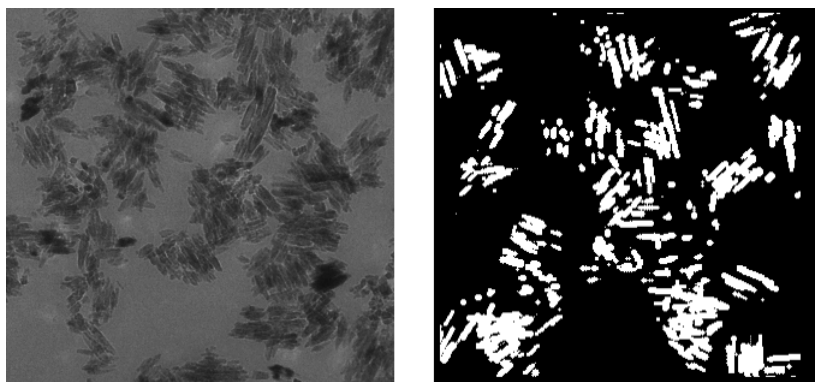


Figure 2.10: Needles microstructure: experimental TEM image (left) and binary image simulated with the morphological model using the optimal set of parameters identified by the Bayesian approach [Figliuzzi et al., 2021].

To determine the model parameters, we employ the Bayesian approach explained in the preceding section. We initiate the Metropolis-Hastings algorithm by setting  $\lambda$  to 1 during the simulation, and we terminate the algorithm after 200 iterations. Similar to before, we estimate the optimal parameter set for the microstructure by selecting the sample that exhibits the highest posterior probability among all the sampled parameters. Throughout the MCMC run, we generate TEM images of the microstructure by first creating a 3D sample of the model, then extracting a thick slice from the 3D volume that matches the thickness of the experimental slices used for obtaining the TEM images, and finally projecting the thick slice onto a single plane. An illustrative example of the microstructure generated using this approach is presented in Figure 2.10. Covariance and granulometry measurements are subsequently performed on both the experimental and simulated TEM images.

The optimal set of parameters  $\hat{\Theta}$  determined by the Metropolis-Hastings algorithm for the morphological model is shown in Table 2.4. A comparison is presented in Figure 2.9 between the measurements conducted on the experimental microstructure and those obtained using the optimal set of parameters. We observe that the optimal parameter set enables us to achieve a good agreement between the experimental measurements and the measurements performed on simulations of the morphological models.

### 2.2.5 Conclusion

In this section, we presented a Bayesian approach for determining the parameters of morphological models of microstructure using measurements obtained from experimental microstructure images. Through various examples, we demonstrated that this approach effectively identifies the optimal parameters for different morphological models and detects potential correlations among the model parameters. Our proposed methodology offers several advantages compared to other parameter determination approaches. Specifically, it eliminates the need for computing the gradient of the model with respect to the parameters and provides a sequence of parameter samples, enabling the quantification of the parameters sensitivity and the identification of potential correlations between them.

## 2.3 Eikonal based tessellations

We present in this section a research work that establishes a link between the Johnson-Mehl and Voronoi tessellation models and the Eikonal equation on a domain. A direct incentive for this study was the development of efficient algorithms for generating the tessellations used to simulate the interstices of the coldspray microstructure considered in section 2.1. We base the writing of this section on the article [Figliuzzi, 2019] published in 2019 in Image Analysis & Stereology and related to this research study. The analogy established between the Voronoi tessellation and the Eikonal equation has two direct applications: the generation of images of the tessellation in an efficient manner, and the generation of tessellations with rough boundaries.

### 2.3.1 Eikonal equation

The Eikonal equation describes the propagation of a wave on an open domain  $\Omega$  through the non-linear partial differential equation:

$$\forall x \in \Omega, \quad \nabla t(x) = \frac{1}{u(x)}. \quad (2.32)$$

In Eq. (2.32),  $\nabla$  denotes the gradient operator, and  $t(x)$  and  $u(x)$  represent the first arrival time of the wave at point  $x$  and the velocity of the wave at location  $x$ , respectively.

In order to compute the image of a Johnson-Mehl tessellation on a domain  $\Omega$ , let us consider the specific version of the Eikonal equation. Given a Poisson point process  $\mathcal{P}$  with realizations  $(x_i)_{i=1,\dots,N}$  and corresponding germination times  $(\tau_i)_{i=1,\dots,N}$ , we consider the problem:

$$\begin{cases} \nabla t(x) = \frac{1}{u(x)} \\ t(x_i) = \tau_i, \forall i = 1, \dots, N. \end{cases} \quad (2.33)$$

If the velocity  $u(x)$  is constant, then we can use the following proposition (see [Sethian, 1996]):

**Proposition 2.3.1.** *On the domain  $\Omega$ , the solution  $t$  of problem (2.33) satisfies, for all  $x \in \Omega$ ,*

$$t(x) = \inf_{i=1,\dots,N} (t_i + \|x - x_i\|^2). \quad (2.34)$$

Proposition 2.3.1 states that solving the Eikonal equation is an efficient way to compute the Johnson-Mehl distance on a grid of points, as it precisely matches the distance used for constructing the Johnson-Mehl tessellation. Efficient algorithms are available for this task, including the fast marching algorithm described in the next section [Sethian, 1996, Dejnozkov and Dokladal, 2003].

### 2.3.2 Fast marching algorithm

The fast marching (FM) algorithm compute the arrival times in the domain iteratively by following the propagation of the waves coming from the germs. Here, we present a slightly adapted version of the fast marching algorithm that keeps track of the labels of the initial germs during the propagation, in order to facilitate the generation of the Johnson-Mehl tessellation. We restrict ourselves to the 2D framework to keep notations simple. We initialize the algorithm as follows:

1. We initialize the map of *arrival times* by setting the arrival at each voxel  $x_i$  equal to  $t_i = \infty$ , except if the considered voxel contains a germ from  $\mathcal{P}$ . In this case, the arrival time at  $x_i$  is set to be the germination time  $\tau_j$ .
2. We initialize a map of *labels* that keeps tracks of the wave that has arrived at each location first. We affect the label  $j$  to the voxels  $x_i$  containing one of the germs  $(g_j)_{1 \leq j \leq N}$  are associated the label  $j$ . We affect the label 0 to the other voxels.
3. Finally, we group all voxels containing one of the germ in a set referred to as the *narrow band*.

At each iteration, we extract the voxel  $(X, Y)$  of the narrow band with smallest arrival time and we affect it to the *frozen set*. Next, we compute the arrival times of the wave at all neighboring voxels and we add these voxels to the narrow band. At each neighbor location  $(x, y)$  of  $(X, Y)$ , we compute the arrival time by solving Eikonal equation

$$\|\nabla T\|(x, y)u(x, y) = 1. \quad (2.35)$$

The main difficulty at this point is to propose a discretization for the gradient term. Following the work [Sethian, 1996], we discretize Eikonal equation in

the following manner

$$(t_{x,y} - \min(t_{x,y+1}, t_{x,y-1}))^2 + \\ (t_{x,y} - \min(t_{x+1,y}, t_{x-1,y}))^2 = \frac{1}{u(x, y)^2} \quad (2.36)$$

In Eq. (2.36), the use of the min operator ensures that the information propagates from the already computed neighbors, which is essential for the stability of the fast marching method. Equation (2.36) is quadratic in  $t_{x,y}$  and admits two solutions. To respect the causality principle, we select the largest solution of (2.36). This choice guarantees that the wave propagates forward in time and maintains the consistency of the numerical scheme.

Once the arrival time  $t(x, y)$  has been computed, we can encounter two distinct situations:

- When the neighbor point  $(x, y)$  is in the narrow band, it means that it has already been affected an arrival time  $t^{old}(x, y)$ . If  $t(x, y) < t_{old}(x, y)$ , then we affect the arrival time  $t(x, y)$  to  $(x, y)$  as well as the label of point  $(X, Y)$ . On the contrary, if  $t(x, y) > t_{old}(x, y)$ , the label and the arrival time at  $(x, y)$  remain unchanged.
- When the neighbor point  $(x, y)$  is not in the narrow band, we affect to it the arrival time  $t(x, y)$  as well as the label of  $(X, Y)$ , and we add it to the narrow band.

At each iteration of the algorithm, it is necessary to extract the element of the narrow band with the smallest arrival time. To sort the elements of the narrow band in an efficient manner, we use a binary heap to store them. We refer the reader interested by more details on the fast marching algorithm implementation to the original articles [Malladi et al., 1995, Sethian, 1996, 1999].

### 2.3.3 Applications

We describe in this section two potential applications of the proposed approach for generating a tessellation: the first application describes a computationally efficient method for generating an image of a Voronoï or Johnson-Mehl tessellation from a set of germs. The second application is related to the generation of tessellation with rough boundaries that it is made possible by the use of Eikonal equation.

### Generation of images from vectorial simulations

For materials engineering applications, it is often necessary to simulate images of a generated Voronoï or Johnson-Mehl tessellation. In practice, the tessellation is entirely characterized by the location of its germs and by the corresponding implantation times in the case of the Johnson-Mehl tessellation. The image generation is achieved by discretizing the domain  $\Omega$  and by evaluating the implicit functions associated with the tessellation's cells at each voxel location. However, this approach can be computationally expensive, particularly when high resolution is required. If we denote the number of voxels used to discretize  $\Omega$  as  $P$ , the average number of Poisson points in  $\mathcal{P}$  is proportional to  $P$ . As a result, the image generation algorithm's complexity is  $O(P^2)$ , which can represent a significant amount of computation when using this method for a vectorial simulation. By contrast, using the approach based on the Eikonal equation yields a complexity in  $O(N \log N)$ , which is particularly appealing for large values of  $N$ .

### Tessellation with rough boundaries

We have considered so far a constant velocity field  $u$  in the Eikonal equation (2.33) for constructing the Johnson-Mehl tessellation. However, when using the Eikonal equation to build the mosaic, it is possible to use any velocity fields on the domain  $\Omega$ , as long as  $u(x) > 0$  for all  $x \in \Omega$ . This observation opens the way to the development of tessellation models that cannot be directly obtained with classical approaches including the Voronoï and the Johnson-Mehl tessellations described previously. A potential application is for instance the generation of tessellations of space with rough boundaries between adjacent cells.

Let  $\mathcal{P}$  be the realization of a marked point process with intensity  $\theta$  on an open domain  $\Omega$ , for which the marks are drawn according to the uniform distribution  $\mathcal{U}([0, L])$  on an interval  $[0, L] \subset \mathbb{R}_+$ . The points in  $\mathcal{P}$  as well as their respective marks allow to compute a Johnson-Mehl tessellation on the domain  $\Omega$  by solving problem (2.33). We construct a random velocity field  $u$  on domain  $\Omega$  by

1. computing a Voronoï tessellation of  $\Omega$  based upon a Poisson point process  $\mathcal{P}_v$  with intensity  $\theta_v$ , and
2. setting a random velocity drawn according to some distribution  $\mathcal{D}$  in each cell of the Voronoï tessellation.

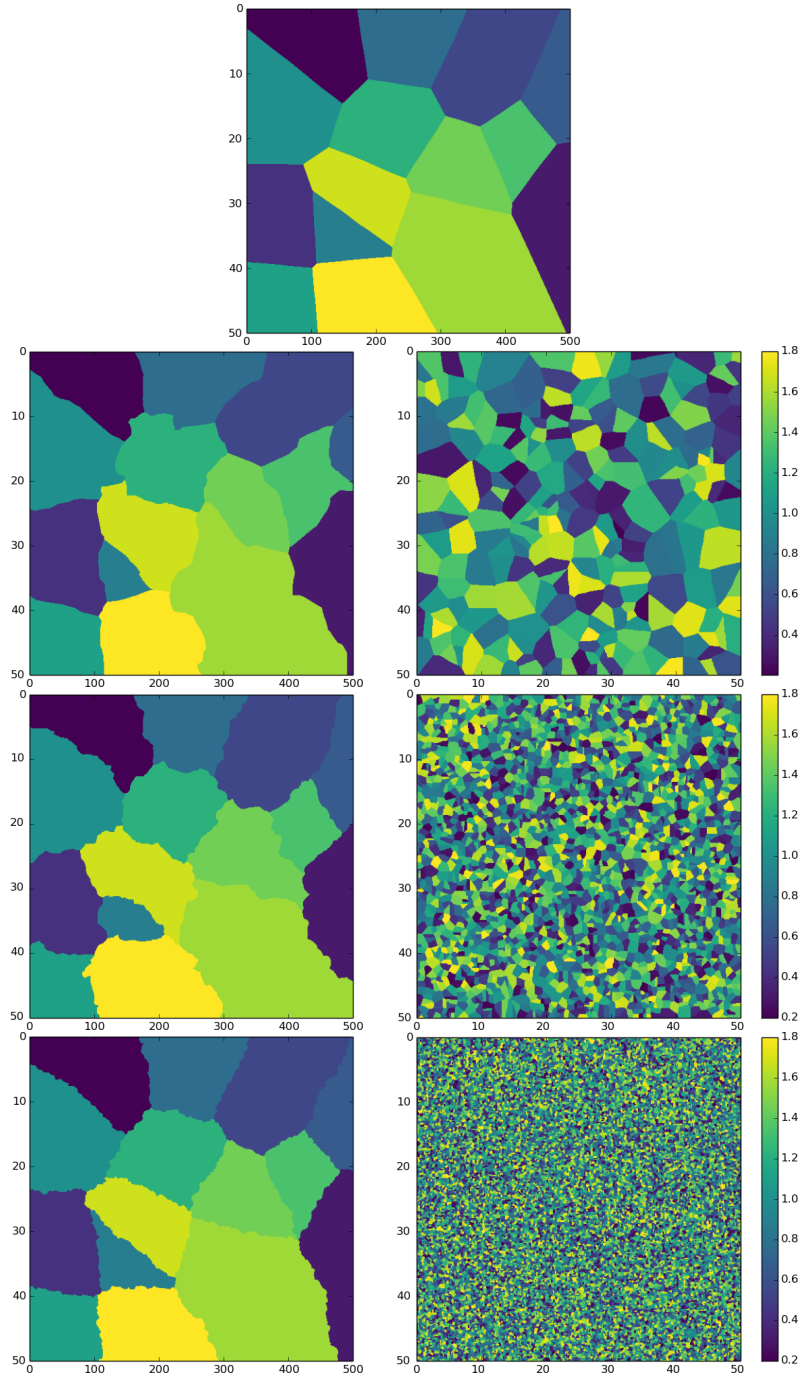


Figure 2.11: Rough Voronoï tessellations (left) and corresponding local velocity field (right). The tessellations were generated with the same set of germs  $\mathcal{P}$  on a  $50 \times 50$  domain, discretized on a  $500 \times 500$  regular grid. The local velocity fields are realizations of Voronoï tessellations with respective intensities  $\theta = 0$ ,  $\theta = 0.1$ ,  $\theta = 1$  and  $\theta = 10$ .

By solving the problem

$$\begin{cases} \nabla t(x) = \frac{1}{u(x)} \\ t(x_i) = \tau_i, \forall i = 1, \dots, N \end{cases} \quad (2.37)$$

we obtain a tessellation of the domain  $\Omega$  resembling the Johnson-Mehl tessellation generated by solving (2.33), but with rough boundaries between adjacent cells. It is worth noting that the roughness observed at the boundaries is closely linked to the characteristic length of the fluctuations in the velocity field. This characteristic length is dependent on the intensity of the Voronoï tessellation, denoted by  $\theta_v$ , which is used to compute the velocity field. A larger value of  $\theta_v$  results in a greater number of smaller Voronoï cells, leading to velocity variations over shorter distances. As a result, the generated Johnson-Mehl tessellation displays boundaries with a high concentration of roughness patterns with relatively small amplitudes. In contrast, Johnson-Mehl tessellations generated from velocity fields constructed with a smaller value of  $\theta_v$  exhibit boundaries with a lower density of roughness patterns with larger amplitudes. In the original article [Figliuzzi, 2019], we developed a multi-scale tortuosity descriptor, which is able to characterize the tortuosity of the boundary between two adjacent cells by iteratively computing the tortuosity of smoothed versions of the boundary. This descriptor allowed us to establish a direct correlation between the value of  $\theta_v$  and the tortuosity of the boundaries at distinct scales. We refer the reader interested by additional details to the original article [Figliuzzi, 2019].

To illustrate our algorithm, we present in figure 2.11 simulations of Voronoï tessellations with rough boundaries computed with different values of velocity parameter  $\theta_v$ . In this figure, we generated four distinct Voronoï tessellations on a domain with size  $50 \times 50$  discretized on a  $500 \times 500$  regular grid. To generate the tessellation, we started from the same realization of a Poisson point process  $\mathcal{P}$  with intensity  $\theta = 5 \times 10^{-2}$ . We generated a random velocity field for each one of the tessellations by first constructing a Voronoï tessellation of the domain, and then selecting a random velocity drawn from the uniform distribution  $\mathcal{U}$  on the interval  $[0.2, 1.8]$  for each cell of the tessellation. The characteristic length  $\lambda_v$  of the velocity variation can be related to the intensity  $\theta_v$  of the point process used to construct the germs of the tessellation through the relationship

$$\lambda_v \simeq \sqrt{\frac{1}{\theta_v}}.$$

We note that when  $\lambda_v$  is small, it leads to the obtaining of small roughness patterns at the cell boundaries. Conversely, large values of  $\lambda_v$  lead to larger sizes of roughness pattern. The proposed method therefore allows to control, at least qualitatively, the amplitude and the size of the roughness patterns observed at the boundaries.

### 2.3.4 Conclusion

In this section, we established a direct connection between Johnson-Mehl and Voronoï tessellations and the Eikonal equation, showing that the construction of such tessellations can be reformulated as a wave propagation problem. This interpretation provides both theoretical insight and practical advantages. In particular, solving the Eikonal equation with appropriate initial conditions enables an efficient computation of tessellations through the fast marching algorithm, significantly reducing computational complexity compared to classical voxel-wise evaluation methods.

Beyond computational efficiency, the Eikonal framework also offers increased modeling flexibility. By introducing spatially varying velocity fields, we demonstrated that it is possible to generate tessellations with controlled boundary roughness, extending classical Voronoï and Johnson-Mehl models. The characteristic length of the velocity fluctuations directly governs the amplitude and scale of boundary irregularities, providing a simple and intuitive way to tune geometric complexity.

Overall, the Eikonal-based formulation constitutes a powerful and versatile approach for the simulation of tessellated microstructures, with direct applications to morphological modeling and materials science.

# Chapter 3

## Image segmentation

In materials science, experimental campaigns can generate large databases of images that require automatic processing for being efficiently exploited. Supervised learning algorithms based on convolutional neural networks constitute the state-of-the-art approaches for performing image segmentation. However, training these architectures depends upon the availability of images segmented manually, which are often not available in sufficient quantity. This challenge is further compounded by the fact that images from materials science experiments are markedly different from the natural images that are typically used for training convolutional neural networks. Consequently, transfer learning techniques alone are insufficient to address the lack of training data. As a result, the development of segmentation methods that can effectively handle limited amounts of data remains a crucial area of research. The applicability of the most effective segmentation methods to actual industrial problems is dependent on overcoming this challenge. This can be done in two manners: first, by pursuing the development of segmentation techniques that require minimal training data; second, by relying on data augmentation and image generation techniques to obtain sufficiently large training datasets for the task at hand. This part of the manuscript presents my main contributions to these two lines of research.

My main contribution to the development of segmentation techniques is related to the work conducted during the PhD thesis of Kaiwen Chang between 2016 and 2019, which I co-directed along with Jesús Angulo at the Centre for Mathematical Morphology [[Chang, 2019](#)]. During the course of this PhD thesis, we developed an algorithm based on the Eikonal equation to generate the superpixel segmentation of a given image based on color

and texture information [Chang and Figliuzzi, 2019, 2020]. Any superpixel segmentation can be represented by a graph whose nodes represent the superpixels of the image and whose edges represent the adjacency relations between superpixels. Using different features extracted from each superpixel, we showed that it was possible to learn a distance characterizing the dissimilarity between neighboring superpixels with a limited number of images. We finally relied on a generalization of the Eikonal equation to graph structures to merge the superpixels of the image into an actual segmentation. I describe these researches in chapters ?? and ?. In chapter ??, I present a study conducted in collaboration with the Institut de Physique de Nice, which explores the second line of research mentioned previously, and aims to segment images in a supervised way from a dataset of images synthesized with a morphological model.

### 3.1 Eikonal-based superpixels

Superpixel algorithms are a class of techniques that seek to divide an image into smaller regions consisting of similar pixels, providing more meaningful and analyzable representations than raw pixels. One major advantage of superpixels is that they significantly reduce the amount of calculations required for further processing, as their number is much lower than that of the original pixels. Moreover, due to their homogeneous nature, superpixels form subregions of the image that are particularly relevant for feature computation. As a result, superpixel algorithms are frequently used as a pre-processing step in various applications such as object classification, image segmentation, or depth estimation, as demonstrated by studies like [Zitnick and Kang, 2007] and [Fulkerson et al., 2009].

A significant amount of literature in computer vision and image analysis is dedicated to the topic of superpixels [Achanta et al., 2012, Stutz et al., 2018, Li and Chen, 2015]. Graph based methods rely on a graph representation of the image. These methods include the normalized cut algorithm (NC) of Shi and Malik [Malik et al., 2001, Shi and Malik, 2000] or the efficient graph-based segmentation algorithm (GS) of Felzenswalb and Huttenlocher [Felzenszwab and Huttenlocher, 2004]. By contrast, clustering based methods proceed by iteratively refining clusters of pixels until some convergence criterion is met. These methods notably include mean shift [Comaniciu and Meer, 2002], watershed [Beucher and Lantuéjoul, 1979, Beucher

and Meyer, 1992, Figliuzzi et al., 2017, Vincent and Soille, 1991, Meyer and Beucher, 1990], turbopixel [Levinshtein et al., 2009] or waterpixel [Cettour-Janet et al., 2019, Machairas et al., 2015] algorithms, respectively.

This section provides a detailed overview of a superpixel-based segmentation approach directly inspired by the Eikonal based tessellation algorithm described in chapter 2. The presentation provided here draws upon the articles [Chang and Figliuzzi, 2019, 2020]. The core motivation was to employ superpixels as a foundational over-segmentation phase, facilitating full image reconstruction through subsequent region-merging methods. Our findings highlighted a critical dependency: the success of the final segmentation is intrinsically linked to the precision of the initial superpixel boundaries. Consequently, a significant portion of our research focused on engineering a robust, clustering-based partitioning method designated as the Fast-Marching Superpixels (FMS) algorithm. Drawing inspiration from the Eikonal-based Region Growing for Efficient Clustering (ERGC) approach by Buyssens *et al.* [Buyssens et al., 2014a,b,c], the FMS algorithm utilizes the Eikonal equation to solve for optimal image partitions.

### 3.1.1 Algorithm

The FMS algorithm operates by likening the growth of regions on an image to waves propagating through a non-uniform medium, where the growth rate depends on the local color and texture. The wave propagation is governed by the stationary Eikonal equation. Hence, the task of constructing the superpixel partition essentially involves solving the Eikonal equation on the image domain using a velocity field that is determined by the local color and texture. A similar approach was introduced by Buyssens *et al.* in 2014 [Buyssens et al., 2014c,b,a], but there are notable differences between the two methods, such as the expression for the local velocity as a function of the image content, the use of texture features, and the region update mechanism during propagation.

#### The Eikonal equation on a bounded domain

We recall in this paragraph the basic notions related to the stationary Eikonal equation, previously introduced in Section 2.2 of Chapter 2. Let  $\Omega$  be a bounded domain in  $\mathbb{R}^2$ . We consider a wavefront originating from a subset of points in the domain and propagating with velocity  $u := u(x)$  prescribed at

each location  $x \in \Omega$ . We denote by  $T : x \mapsto T(x)$  the function that associates to each point  $x \in \Omega$  the first arrival time of the wavefront.

It can be shown [Sethian, 1996] that  $T$  satisfies the stationary Eikonal equation

$$\|\nabla T(x)\| = \frac{1}{u(x)}, \quad \forall x \in \Omega. \quad (3.1)$$

The stationary Eikonal equation (3.1) must be supplemented with boundary conditions prescribed on  $\partial\Omega$ . Typically, a function  $g$  is defined on  $\partial\Omega$  such that  $T(x) = g(x)$  for all  $x \in \partial\Omega$ . In many applications,  $g$  is taken to be identically zero. In this case, the stationary Eikonal problem reads

$$\begin{cases} \|\nabla T(x)\| = \frac{1}{u(x)}, & \forall x \in \Omega, \\ T(x) = 0, & \forall x \in \partial\Omega. \end{cases} \quad (3.2)$$

For any  $x \in \Omega$ , the solution  $T(x)$  of (3.2) can be interpreted as the minimal time required to travel from  $x$  to the boundary  $\partial\Omega$ . Equivalently, the Eikonal equation provides the geodesic distance from  $x$  to  $\partial\Omega$  with respect to the metric induced by the slowness  $1/u(x)$ .

Efficient numerical methods have been developed to solve the Eikonal equation. Among them, the fast marching method, originally introduced by Sethian *et al.*, is one of the most widely used. This method tracks the evolution of the wavefront in a monotone fashion and computes the first arrival times iteratively [Sethian, 1996].

## Region growing

In this section, we describe the practical implementation of the proposed superpixel generation algorithm. Let us first introduce some notation. A pixel in the image  $\mathcal{I}$  is denoted by  $p$ , with spatial coordinates  $(x, y)$ . We denote by  $\mathbf{C}(p)$  the color of pixel  $p$  in the CIELAB color space. Similarly,  $\mathbf{T}(p)$  denotes a feature vector characterizing the local texture at pixel  $p$ . The proposed algorithm amounts to solving the stationary Eikonal equation on the image domain using the fast marching method, with a velocity field that depends on the local image content.

Let  $K$  be the desired number of superpixels. The algorithm is initialized by selecting  $K$  seeds placed on a regular grid. To avoid positioning a seed on an image boundary, and following [Achanta et al., 2012], each seed is moved

to the location corresponding to the minimum gradient magnitude within a  $3 \times 3$  neighborhood centered at the grid node.

For each seed  $s_i$ , we define a velocity field  $u_i(p)$  that depends on both the color and texture features of the seed and those of the pixel  $p := (x, y)$ . The seed labels are then progressively propagated from labeled to unlabeled pixels according to the local velocities  $(u_i(p))_{i=1,\dots,K}$ . This propagation process is governed by the Eikonal equation

$$\begin{cases} \|\nabla T(p)\| = \frac{1}{u(p)}, & \forall p \in \mathcal{I}, \\ T(p) = 0, & \forall p \in \partial\mathcal{I}, \end{cases} \quad (3.3)$$

where  $u(p)$  denotes the local velocity at pixel  $p$ ,  $\partial\mathcal{I}$  represents the set of seeds  $\{s_1, s_2, \dots, s_K\}$ , and  $T(p)$  corresponds to the minimal travel time from  $\partial\mathcal{I}$  to  $p$ .

Once the seeds have been initialized, Eq. (3.3) is solved using the fast marching algorithm. Its computational complexity is  $O(N \log N)$  [Sethian, 1996, 1999], where  $N$  denotes the total number of pixels in the image.

### Local velocity model

The algorithm described in the previous paragraph can be applied with any non-negative velocity model  $u(p)$ . One of the main challenges in superpixel segmentation arises from highly textured regions. In such areas, the colorimetric distance between two pixels does not necessarily indicate whether they belong to the same cluster. To account for this limitation, we adopt a velocity model that incorporates both local color and texture information. This model relies on a distance  $D$  between a pixel  $p$  and a seed  $s_i$ , defined as

$$D(p, s_i) = w_0 \|\mathbf{C}_p - \mathbf{C}_i\|_2 + w_1 d(\mathbf{T}_p, \mathbf{T}_i), \quad (3.4)$$

where  $\mathbf{T}_p$  is a feature vector characterizing the local texture at pixel  $p$ ,  $\mathbf{T}_i$  is the corresponding feature vector associated with the  $i$ -th cluster center  $s_i$ ,  $d(\mathbf{T}_p, \mathbf{T}_i)$  denotes a texture distance between  $p$  and  $s_i$ , and  $w_0, w_1$  are positive weights controlling the respective contributions of color and texture.

Several approaches can be used to construct the feature vector  $\mathbf{T}_p$ . In our study, we built a texton map using a texture classifier and associated with each pixel a histogram of textons computed over a local window of fixed size. The texture distance between two pixels is then defined as the  $\chi^2$  distance between their corresponding texton histograms.

The local velocity  $u_i(p)$  governing the propagation of region  $i$  is defined using an exponential kernel:

$$u_i(p) = \exp(-w_0\|\mathbf{C}_p - \mathbf{C}_i\|_2 - w_1 d(\mathbf{T}_p, \mathbf{T}_i)). \quad (3.5)$$

Within the fast marching scheme, the velocity reaches its maximum value, equal to 1, when the pixel and the associated cluster center have identical color and texture features.

The weighting parameters  $w_0$  and  $w_1$  must be chosen carefully. Increasing their values improves adherence to image boundaries, since the propagation velocity becomes more sensitive to variations in color and texture. However, excessively large values (e.g.,  $w_0, w_1 > 8$ ) may cause the local velocity to become very small, leading to the formation of numerous small and isolated superpixels, particularly in low-contrast regions. This effect can deteriorate the compactness and regularity of the final superpixel partition. Consequently, selecting these parameters involves a trade-off between boundary adherence and topological regularity.

## Refinement

Images often contain regions of interest with widely varying spatial scales, which makes the selection of seeds on a uniform grid suboptimal for superpixel segmentation. To improve boundary adherence, we introduce a refinement strategy based on the map of arrival times.

The map  $T(p)$  obtained at the end of the superpixel generation process encodes the arrival time at each pixel  $p$ . This information can be exploited to refine the superpixel partition by inserting additional seeds. When the arrival time at a pixel  $p$  within a region  $\mathcal{R}_i$  associated with seed  $s_i$  is large, it indicates that the front propagating from  $s_i$  has traversed pixels that are significantly dissimilar from the seed. Consequently, the distribution of arrival times within each region  $\mathcal{R}_i$  provides a natural criterion to decide whether the region should be further subdivided. A related refinement strategy based on a distance map is proposed in [Buyssens et al., 2014b], where new superpixels are generated at the end of the over-segmentation process.

The refinement procedure is defined as follows. Let  $\mathcal{B}$  denote the set of pixels belonging to superpixel boundaries, and let  $\delta(\mathcal{B})$  be the dilation of  $\mathcal{B}$  by a disk of radius 2 pixels. The maximal arrival time within region  $\mathcal{R}_i$  is defined by

$$t_i = \max_{p \in \mathcal{R}_i \cap \delta(\mathcal{B})^c} T(p), \quad (3.6)$$

where  $\delta(\mathcal{B})^c$  denotes the complement of  $\delta(\mathcal{B})$ .

To refine the segmentation, we select the  $k$  regions with the largest values of  $t_i$  and insert new seeds at the corresponding locations, before performing a new propagation step. The parameter  $k$  is fixed by the user. Pixels belonging to  $\delta(\mathcal{B})$  are excluded in order to prevent placing a seed directly on a boundary. This procedure is repeated iteratively until the desired number of superpixels is reached. In practice, this refinement significantly improves boundary adherence. However, it generally reduces the compactness of the segmentation, as it increases the superpixel density in selected regions of the image.

### Comparison with other algorithms

It is instructive to highlight the main differences between the proposed FMS algorithm and the ERGC method [Buyssens et al., 2014a,b,c]. Although both approaches rely on the Eikonal equation to generate superpixel partitions, they differ substantially in their modeling choices and practical implementation.

ERGC is a clustering-based algorithm that formulates superpixel segmentation through the resolution of an Eikonal equation driven by a color-based velocity model. In ERGC, the local velocity associated with seed  $s_i$  is defined as

$$u_i(p) = \frac{1}{\|\mathbf{C}_p - \mathbf{C}_i\|_2}. \quad (3.7)$$

With this formulation, the propagation speed becomes very large when the color of pixel  $p$  is close to that of the seed  $s_i$ , and decreases as the color distance increases. As a result, the front expands rapidly within homogeneous color regions and slows down near strong color transitions, promoting boundary adherence. However, since the velocity depends solely on color information, ERGC may struggle in highly textured regions where color similarity alone is not sufficient to characterize perceptual homogeneity.

In contrast, the FMS algorithm incorporates both color and texture information into the velocity model. This allows the propagation process to better account for complex image content, particularly in textured areas where purely color-based distances are ambiguous. Moreover, the exponential formulation adopted in FMS ensures that the velocity remains bounded and smoothly decreases as feature dissimilarity increases, leading to a more

stable and controlled propagation behavior compared to the reciprocal form used in ERGC.

FMS is also closely related to the Iterative Spanning Forest (ISF) algorithm [Vargas-Muñoz et al., 2019]. ISF constructs superpixels by iteratively growing regions from a set of seeds and merging pixels according to a path-cost function designed to maximize intra-cluster similarity in terms of color and spatial proximity. This optimization is performed through a greedy strategy. Although ISF is not explicitly formulated in terms of wave propagation governed by the stationary Eikonal equation, its region-growing mechanism shares conceptual similarities with the fast marching procedure used in both FMS and ERGC. In all cases, labels are propagated from seeds to neighboring pixels according to a local optimality criterion.

Overall, the proposed approach differs from ERGC primarily in the definition of the velocity model and the integration of texture features into the clustering process. Compared to ISF, the main distinctions lie in the explicit Eikonal-based formulation, the continuous propagation framework underlying the fast marching scheme, and the incorporation of a refinement strategy based on arrival times. Additionally, the proposed method includes a specific seed initialization and refinement procedure that are not part of the standard ISF and ERGC formulations. These differences collectively contribute to improved boundary adherence and greater flexibility in handling complex image content.

### 3.1.2 Experiments and discussion

In this section, we evaluate the performance of the FMS algorithm and compare it with several state-of-the-art superpixel methods, including SLIC [Achanta et al., 2012], ERGC [Buyssens et al., 2014a,b,c], and ISF [Vargas-Muñoz et al., 2019]. These approaches share a common principle: superpixels are generated through clustering-based strategies. More precisely, SLIC relies on a variant of the  $K$ -means algorithm in a joint color–spatial feature space, whereas ERGC, ISF, and FMS adopt iterative region-growing or agglomerative procedures driven by local similarity measures.

For the quantitative evaluation, we use the Berkeley Segmentation Dataset 500 (BSDS500) [Martin et al., 2001, Arbelaez et al., 2011]. This benchmark dataset contains 500 natural images, each accompanied by multiple human-annotated ground truth segmentations. The availability of several manual segmentations per image makes BSDS500 particularly suitable for assessing

superpixel algorithms, as it allows the comparison of the generated partitions with perceptually meaningful boundaries.

In addition, we previously reported in [Chang, 2019, Chang and Figliuzzi, 2020] an evaluation of FMS on a dedicated texture-oriented dataset introduced by Giraud *et al.* [Giraud et al., 2019]. This dataset is composed of synthetic images obtained by recombining texture patches extracted from striped patterns and was specifically designed to assess the performance of superpixel methods in highly textured scenarios. These complementary experiments highlight the ability of FMS to handle complex texture variations in comparison with competing approaches.

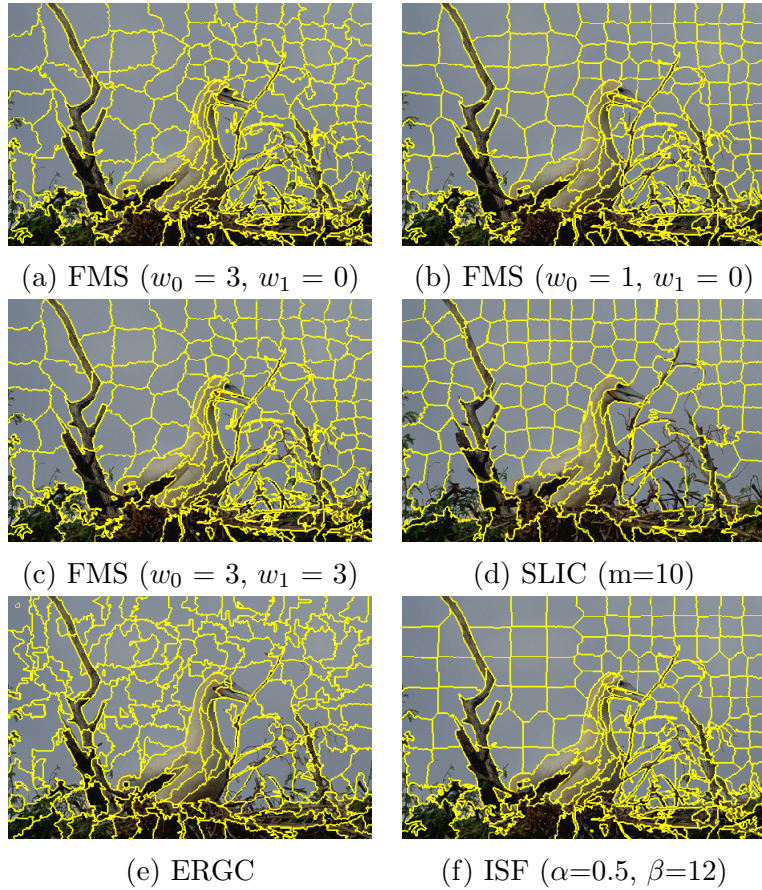


Figure 3.1: Illustration of the superpixel segmentation on an image of the BSDS500, for  $K = 200$  superpixels.

### Experiments on the BSD500 dataset

To evaluate the performance of the algorithms, we considered the following metrics: boundary recall, undersegmentation error, compactness and contour density [Schick et al., 2012].

**Boundary Recall.** Boundary recall (BR) measures how well superpixel boundaries align with the ground-truth object boundaries. Let  $B_{GT}$  denote the set of ground-truth boundary pixels and  $B_{SP}$  the set of superpixel boundary pixels. Given a tolerance distance  $\epsilon > 0$ , boundary recall is defined as

$$\text{BR} = \frac{|\{p \in B_{GT} \mid \exists q \in B_{SP} \text{ such that } \|p - q\| \leq \epsilon\}|}{|B_{GT}|}. \quad (3.8)$$

It corresponds to the fraction of ground-truth boundary pixels that are correctly detected (within tolerance) by the superpixel boundaries. Higher values indicate better adherence to perceptually meaningful contours.

**Undersegmentation Error.** Undersegmentation error (UE) quantifies the extent to which superpixels overlap multiple ground-truth regions. Let  $\{S_k\}_{k=1}^K$  be the set of superpixels and  $\{G_j\}_{j=1}^J$  the set of ground-truth regions. A common formulation is

$$\text{UE} = \frac{1}{N} \sum_{k=1}^K \left( \sum_{j=1}^J \min(|S_k \cap G_j|, |S_k \setminus G_j|) \right), \quad (3.9)$$

where  $N$  is the total number of pixels. This metric penalizes superpixels that span across multiple ground-truth regions. Lower values indicate better segmentation purity.

**Compactness.** Compactness measures the regularity of superpixel shapes. For each superpixel  $S_k$ , let  $A_k = |S_k|$  be its area and  $P_k$  its perimeter. A common compactness measure is based on the isoperimetric ratio:

$$\text{Compactness}(S_k) = \frac{4\pi A_k}{P_k^2}. \quad (3.10)$$

The global compactness score is then obtained by averaging over all superpixels:

$$\text{CO} = \frac{1}{K} \sum_{k=1}^K \frac{4\pi A_k}{P_k^2}. \quad (3.11)$$

This quantity lies in  $(0, 1]$ , with values closer to 1 corresponding to more regular (circular) shapes.

**Contour Density.** Contour density (CD) measures the proportion of boundary pixels relative to the image size. Let  $B_{SP}$  denote the set of superpixel boundary pixels and  $N$  the total number of pixels. It is defined as

$$\text{CD} = \frac{|B_{SP}|}{N}. \quad (3.12)$$

Higher contour density corresponds to finer segmentations (more superpixels), while lower values indicate coarser partitions. This metric provides a normalized measure of segmentation granularity.

Figure 3.2 displays the recall, undersegmentation error, compactness and density metrics of FMS, SLIC, ISF and ERGC averaged over the 500 images of the BSDS500. These metrics are represented for a number  $K$  of superpixels ranging from 100 to 600. We also display in Fig. 3.1 superpixel partitions obtained with these algorithms on an image of the BSDS500. In our results, we present several versions of the FMS algorithm: two versions using only color information, and a third one incorporating texture information through an additional texton channel computed with a bank of Gabor filters [Jain and Farrokhnia, 1991]. We selected the parameter  $w_0 = 3$  for the color term in the velocity expression (3.5) by relying on a grid search to maximize boundary adherence while keeping a reasonable compactness for the superpixel partition. To illustrate the trade-off between compactness and boundary recall controlled by the parameter  $w_0$ , we also displayed the metrics as obtained with the set of parameters  $w_0 = 1$  and  $w_1 = 0$ . Finally, we computed the superpixel partition using the parameters  $w_0 = 3$  and  $w_1 = 3$  to evaluate the texture influence. Additional experiments aiming at characterizing the influence of the refinement and of the seeds initialization are also presented in the original article [Chang and Figliuzzi, 2019, 2020] related to the present work.

In terms of recall, we can note that the FMS algorithm yields better results than SLIC and ERGC algorithms, and performs slightly better than ISF

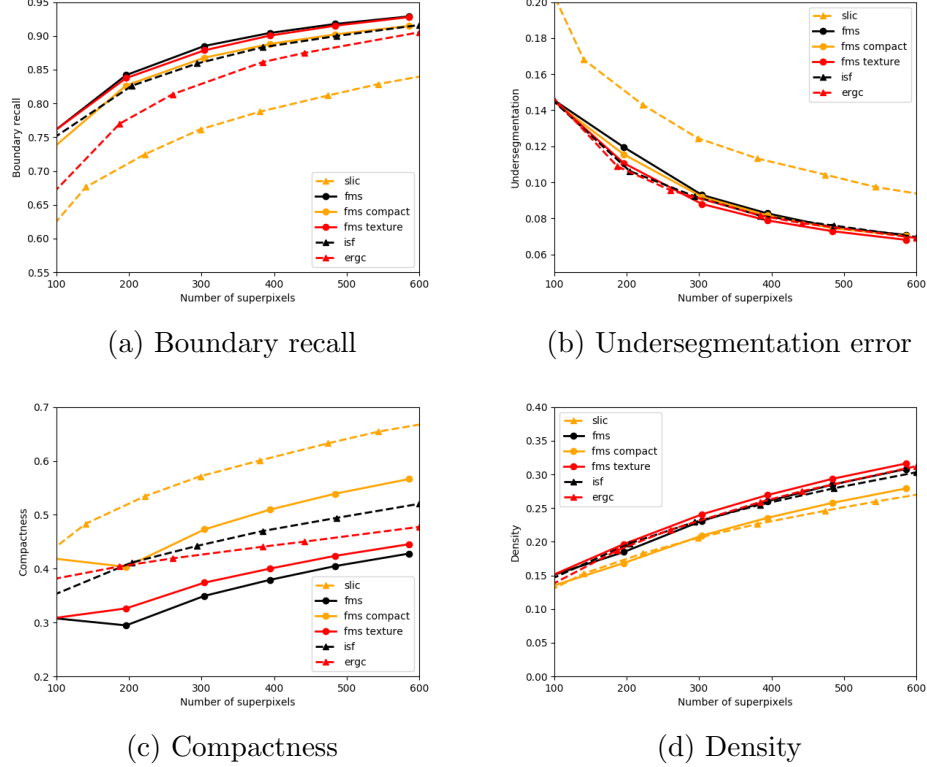


Figure 3.2: Comparison between SLIC, ERGC, IFS and FMS algorithms on BSDS500.

when  $w_0 = 3$ . However, the boundary recall should be considered along with compactness, and we can note that the compactness of the FMS algorithm is significantly lower than the one of ISF when  $w_0 = 3$ . Interestingly, when specifying  $w_0 = 1$  and therefore favoring the construction of compact superpixels, we are able to obtain a similar boundary recall than the one reached by ISF, but with higher compactness. The gain in terms of superpixel compactness is also clearly visible in Fig. 3.1. The compact FMS algorithm also exhibits a smaller density when compared to all other algorithms except SLIC. The performances of SLIC appear to be significantly below the ones of the other algorithms. Regarding the compactness, we can note that the compactness decreases between  $K = 100$  and  $K = 200$  for the FMS algorithm. This is caused by the fact that no refinement steps are applied when computing the partition with  $K = 100$  superpixels. Due to the refinement

procedure, the size of the superpixels constructed with the FMS algorithm is locally adapted depending on the content of the image. Therefore, the refinement is performed at the expense of the superpixels uniformity: the refinement yields superpixels that are heterogeneous in scale and size. We can finally note that in terms of undersegmentation, all considered superpixel algorithms are relatively similar.

### 3.1.3 Conclusion

During Kaiwen Chang’s PhD thesis research [Chang, 2019], we developed a fast-marching based algorithm for generating superpixel partitions of images, building upon an idea initially used in the ERGC algorithm by Buyssens *et al.* [Buyssens et al., 2014a,b,c]. The significant contribution of this study was the introduction of a new expression for the velocity term, which allowed for texture information to be incorporated into the computation of the superpixel partition. In addition, different strategies were also proposed to refine the segmentation.

We evaluated the FMS algorithm on the Berkeley Segmentation Database 500 and we found that it constructs superpixel partitions with slightly higher recall and similar undersegmentation error compared to similar superpixel algorithms such as ERGC, ISF, and SLIC. Moreover, we demonstrated that the inclusion of texture information improved the compactness of the partition without compromising boundary recall.

One potential extension of this work could involve incorporating gradient information into the local velocity model to better account for contours and image discontinuities. It would also be interesting to attempt to automatically estimate optimal parameters, such as  $w_0$  and  $w_1$ , based on the processed image, a strategy that has been successfully employed in several other superpixel algorithms [Achanta and Susstrunk, 2017, Giraud et al., 2019]. Additionally, developing a multiscale version of the algorithm, where superpixels are computed and refined at different scales using a pyramid representation of the image, could be useful. This multiscale approach could generate a hierarchy of superpixel partitions and a corresponding saliency map, which could be utilized as a criterion for superpixel merging.

## 3.2 Eikonal-based region merging

In chapter ??, we presented a superpixel algorithm using the Eikonal equation to compute the superpixel partition of an image. We go one step further in this chapter and present a generalization of this algorithm to the framework of graphs, which allows to merge image regions into an actual segmentation of the image. The chapter is organized as follows: in section 3.2.1, we introduce a generalization of the Eikonal equation to the setting of graphs. In section 3.2.2, we explain how the Eikonal equation can be leveraged to perform region merging in the image. We present finally in section 3.2.3 the results obtained with our algorithm on the Berkeley Segmentation Dataset and compare these results to the ones obtained with a classical algorithm for performing graph clustering: the normalized cut [Shi and Malik, 2000]. The research works presented in this chapter was conducted during the PhD thesis of Kaiwen Chang between 2016 an 2019 [Chang, 2019].

### 3.2.1 Eikonal equation on an undirected graph

We describe in this section how to extend the continuous Eikonal equation to the setting of graphs. A graph is a structure employed to depict a collection of objects, wherein certain objects are connected. The objects are denoted by *vertices* or *nodes*, while the connections between pairs of vertices are represented by *edges*.

#### Eikonal equation

In what follows, we consider an undirected, path-connected graph  $\mathcal{G} := (V, E)$ . We assume that each edge  $(i, j)$  in  $E$  connecting vertices  $V_i$  and  $V_j$  carries a weight  $w_{ij}$  that describes the similarity between nodes  $V_i$  and  $V_j$ , and that  $t : V \rightarrow \mathbb{R}$  is some function defined on the set  $V$  of all vertices of the graph. To keep notations simple, we note  $t_u$  the value of the function  $t$  at vertice  $u$ .

**Definition 3.2.1.** *Let  $v$  be some vertex of the graph. We denote by  $\mathcal{N}_v$  the set of all neighbor vertices of  $v$  i.e. the set of all vertices that are connected to  $v$ . For all vertices  $u$  in  $\mathcal{N}_v$ , the morphological derivative of  $t$  at  $v$  with respect to  $u$  is:*

$$Dt(u, v) := w_{uv}(t_u - t_v)^+, \quad (3.13)$$

*where the quantity  $(t_u - t_v)^+$  is defined by  $(t_u - t_v)^+ = \max(0, t_u - t_v)$ .*

Definition 3.2.1 allows us to define the gradient of  $t$  in the following manner:

**Definition 3.2.2.** *The gradient of  $t$  at vertex  $v$  is the vector*

$$\nabla t(v) := (Dt(u, v))_{u \in \mathcal{N}_v}. \quad (3.14)$$

Based on definitions 3.2.1 and 3.2.2, we can propose a formulation of the Eikonal equation adapted to graph structures by using an analogy with the continuous setting. In the continuous setting, the Eikonal equation relates the  $L^p$  norm of the local gradient to the local velocity  $u$  in the open domain  $\Omega$ :

$$u(x)\|\nabla t(x)\|_p = 1, \quad \forall x \in \Omega. \quad (3.15)$$

For a graph structure, the equivalent formulation is therefore

$$u(v)\|\nabla t(v)\|_p = 1, \quad \forall v \in V, \quad (3.16)$$

where  $u(v)$  denotes a local velocity associated to node  $v$ .

Here, we focus on the case where  $p = \infty$ . In this case, the Eikonal equation is given at each vertex  $v$  of  $\mathcal{G}$  by

$$u(v) \max_{u \in \mathcal{N}_v} w_{uv}(t_u - t_v)_+ = 1. \quad (3.17)$$

The choices of  $p = \infty$  and of the morphological derivative in Eq. (3.2.1) are not accidental and expression (3.17) arises naturally if we consider a wave propagating on the entire graph  $\mathcal{G}$  and arriving at a given vertice  $v \in \mathcal{G}$ . For all neighbor vertices  $u \in \mathcal{N}_v$ , we have necessarily

$$t_v \leq t_u + \frac{1}{w_{uv}}, \quad (3.18)$$

and there exists a particular neighbor  $\hat{u}$  of  $v$  such that

$$t_u = t_{\hat{u}} + \frac{1}{w_{\hat{u}v}}. \quad (3.19)$$

If we put these requirements together, we obtain the single equation

$$\|\nabla t(v)\| := \max_{u \in \mathcal{N}_v} w_{uv}(t_v - t_u)^+. \quad (3.20)$$

It is finally straightforward to define boundary conditions for the Eikonal equation, by simply selecting a subset  $\partial\mathcal{G} = (v_i)_{1 \leq i \leq k}$  of  $k$  vertices in  $V$  and specifying that  $\forall i = 1, \dots, k$ ,  $t_{v_i} = 0$ .

### Eikonal equation and shortest path distance between two vertices

**Definition 3.2.3** (Shortest path distance between two vertices). *Let us denote by  $\mathcal{P}(u, v)$  the set of all paths in  $\mathcal{G}$  that connect vertices  $u$  and  $v$ . Since  $\mathcal{G}$  is path-connected,  $\mathcal{P}(u, v)$  contains at least one element. A path  $p$  in  $\mathcal{G}(V, E)$  is a collection of edges in  $E$ . The distance  $D(p)$  associated to path  $p$  is simply the sum of the weights of the edges constitutive of  $p$ . The shortest path distance between two vertices  $u$  and  $v$  in  $\mathcal{G}$  is:*

$$\hat{D}(u, v) = \min_{p \in \mathcal{P}(u, v)} D(p) \quad (3.21)$$

Building upon this definition, we can define the distance function between any vertex  $v$  of the graph and the subset  $\partial\mathcal{G} = (v_i)_{1 \leq i \leq k}$  to be

$$d(v, \partial\mathcal{G}) = \inf_{i=1, \dots, k} \hat{D}(v, v_i). \quad (3.22)$$

Proposition 3.2.1 relates the distance function to the solution of the Eikonal equation:

**Proposition 3.2.1.** *Let  $\mathcal{G}$  be an undirected, weighted graph. Then, the gradient of the distance function  $d(\cdot, \partial\mathcal{G})$  satisfies the Eikonal equation*

$$\|\nabla t(v)\| = 1$$

with boundary conditions  $t(v_i) = 0, \forall i = 1, \dots, k$ .

### Fast marching algorithm on graphs

We present in this section the generalization of the fast marching algorithm already encountered in chapters ?? and ?? to undirected graph structures. To that end, let us consider an undirected, path-connected graph  $\mathcal{G} := (V, E)$  such that each edge  $(i, j)$  in  $E$  carries a weight  $w_{ij}$ . The fast marching algorithm seeks to determine the solution of the Eikonal equation. However, instead of iteratively solving this equation for each vertex of  $\mathcal{G}$  until convergence, it works by following the front propagation within the graph to compute the arrival times. During the procedure, the vertices of  $\mathcal{G}$  are divided into three distinct subsets:

- The *frozen* set groups all vertices already reached by the propagation front.

- Vertices adjacent to the frozen points but not reached by the front yet are grouped in the *narrow band*.
- The remaining vertices constitute a subset referred to as the *far away* set.

### Initialization

1. We affect the arrival time  $t = 0$  to all vertices in  $\partial\mathcal{G}$  and we add them to the narrow band.
2. We label all other vertices as *far away* and we affect them the arrival time  $\infty$ . The frozen set is initially empty.
3. In order to keep track of the shortest paths between each vertex in  $\mathcal{G}$  and the boundary  $\partial\mathcal{G}$ , we affect the label  $i$  to each vertex in  $\{v_i, i = 1, \dots, k\}$ . All other vertices are labelled 0.

**Iteration** At each iteration, we extract the vertex  $v$  of the narrow band with the smallest arrival time and we label it as *frozen*. Next, we compute the arrival times for each neighbor  $u$  of  $v$  not belonging to the frozen set, by solving equation (3.17) and by considering that the arrival times at the neighbor nodes  $w$  of  $u$  are  $t_w$  if  $w \in \mathcal{C}_i$  and  $\infty$  otherwise, where  $\mathcal{C}_i$  is the subset of  $\mathcal{G}$  containing the points reached by the front that emerged from the  $i$ -th vertex in  $\partial\mathcal{G}$ . We assume obviously that  $v \in \mathcal{C}_i$ . Once the arrival time  $t$  of a neighbor point  $u$  has been computed, two situations can be encountered:

- When  $u$  is in the narrow band, it has already been affected an arrival time and it is affected to one of the subsets  $\mathcal{C}_j, j = 1, \dots, k$ . If the new arrival time is smaller than the current one, the arrival time is updated and the vertex  $u$  is affected to the subset  $\mathcal{C}_i$ .
- When the neighbor vertex  $u$  is in the *far away* set, we add it to the narrow band with the computed arrival time and to the subset  $\mathcal{C}_i$ .

**Stopping condition** The fast marching algorithm stops when the narrow band is empty.

### 3.2.2 Application to superpixels merging

We describe in this section an algorithm that allows to perform the clustering of a similarity graph based on the resolution of the Eikonal equation in order to perform the segmentation of color images. A similar idea was proposed in 2014 in [Buyssens et al., 2014c].

Let  $I$  be a color image. We denote by  $I(p, q)$  the color of the pixel located at position  $(p, q)$  in the image. In what follows, we assume that  $I$  is represented as the union of  $N$  disjoint superpixels  $(\mathcal{S}_i)_{i=1,\dots,N}$ :

$$I = \bigcup_{1 \leq i \leq N} \mathcal{S}_i, \quad (3.23)$$

with  $\mathcal{S}_i \cap \mathcal{S}_j = \emptyset$  if  $i \neq j$ .

**Region adjacency graph** We can associate to the superpixel partition of  $I$  a graph referred to as its region adjacency graph  $\mathcal{G}$ . This region adjacency graph is a representation of the image  $I$  as an undirected graph, whose vertices  $(V_i)_{i=1,\dots,N}$  are associated with the superpixels  $(\mathcal{S}_i)_{i=1,\dots,N}$ . Two vertices  $V_i$  and  $V_j$  are linked by an edge of the graph if and only if the corresponding superpixels  $\mathcal{S}_i$  and  $\mathcal{S}_j$  share a common boundary in the image. In the following, we will adopt the notation  $\mathcal{G} := (V, E)$  when referring to the region adjacency graph, where  $V$  is the set of all vertices (superpixels) in  $\mathcal{G}$  and  $E$  the set of all edges.

We can specify a weight for each edge in  $E$  by defining a function  $w : E \rightarrow [0, 1]$  which associates to the edge  $e_{ij}$  joining vertices  $v_i$  and  $v_j$  a quantity  $w_{ij} \in [0, 1]$ , interpreted as a dissimilarity measure between superpixels  $\mathcal{S}_i$  and  $\mathcal{S}_j$ . Several approaches have been considered in the literature to compute the dissimilarity weights  $w_{ij}$ , including the color distance between  $\mathcal{S}_i$  and  $\mathcal{S}_j$  or the strength of the gradient at the boundary. Here, we will assume that, for each pair  $(\mathcal{S}_i, \mathcal{S}_j)$  of adjacent superpixels, we were able to estimate the probability  $p_{ij}$  that  $\mathcal{S}_i$  and  $\mathcal{S}_j$  belong to the same segment of the image. It is clear that the quantity

$$w_{ij} = \exp(-p_{ij}), \quad (3.24)$$

then defines a dissimilarity measure between vertices  $V_i$  and  $V_j$  of  $\mathcal{G}$ .

**Graph clustering** According to proposition 3.2.1, it is possible to partition a graph  $\mathcal{G}$  into  $K \geq 1$  subgraphs by relying on the Eikonal equation. To that end, we start by selecting  $K$  vertices  $(v_k)_{1 \leq k \leq K}$  of  $\mathcal{G}$ . Then, solving the

Eikonal equation on  $\mathcal{G}$  with boundary conditions set to be  $t(v_k) = 0, \forall k = 1, \dots, K$  allows to compute the distance  $w(v, \partial\mathcal{G})$  of the shortest path linking each vertex  $v \in V$  to the closest vertex in the subset  $\partial\mathcal{G} := (v_k)_{1 \leq k \leq K}$ . Since the graph  $\mathcal{G}$  is path-connected, for  $k = 1, \dots, K$ , the subsets

$$\mathcal{C}_k = \{v \in V, w(v, v_k) = w(v, \partial\mathcal{G})\} \quad (3.25)$$

constitute a partition of  $\mathcal{G}$  into  $K$  connected subgraphs. We can use this approach to compute a partition of the region adjacency graph associated to a superpixel segmentation and therefore coarsen the segmentation.

**Algorithm** The merging algorithm that we proposed works by iteratively solving the Eikonal equation on the region adjacency graph of the superpixel segmentation  $\mathcal{S}$  of  $I$  and adapting the boundary conditions. The algorithm start with an initial segmentation  $\mathcal{S}^0$  containing  $N$  superpixels. Typical values for  $N$  are in the order of 500 to 800 superpixels. Our objective is to significantly reduce the number of segments in the image to a value around 50 – 100. The superpixel merging is conducted as follows:

1. To initialize the algorithm,  $K$  vertices  $(v_k)_{1 \leq k \leq K}$  are chosen randomly in the region adjacency graph.
2. The Eikonal equation is solved for the region adjacency graph with boundary conditions  $t(v_k) = 0, \forall k = 1, \dots, K$ . After this step, the graph is clustered into  $K$  separated subgraphs  $(\mathcal{G}_k)_{k=1,\dots,K}$ . For  $k = 1, \dots, K$ , we denote by  $V_k$  and  $E_k$  the set of the vertices and of the edges of  $\mathcal{G}_i$ , respectively.
3. For each subgraph  $(\mathcal{G}_k)_{k=1,\dots,K}$ , we search for the edge  $e_k$  in  $E_k$  with maximal weight  $w_k$ . We denote by  $n_{0,k}$  and  $n_{1,k}$  the vertices in  $V_k$  linked by  $e_k$ . Then, we select the subgraph  $\mathcal{G}_j$  whose maximal internal weight is the highest and we add the nodes  $n_{0,j}$  and  $n_{1,j}$  to the boundary conditions. This step allows to refine the previously obtained segmentation.
4. We solve the Eikonal equation for the region adjacency graph with the updated boundary conditions  $t(v_k) = 0, \forall k = 1, \dots, K + 2$ , where  $v_{k+1} = n_{0,j}$  and  $v_{k+2} = n_{1,j}$ .
5. We iterate between steps 3 and 4 until some stopping criterion is met.

Two distinct stopping criteria can be used in the algorithm. A first stopping criterion consists in stopping the algorithm iterations when a specified number of segments are obtained, the advantage of this approach being that it enables to control the number of segments obtained in the final segmentation. However, this approach can potentially yield a segmentation with segments still containing highly dissimilar superpixels. A second stopping criterion consists in specifying a probability threshold  $t$  and in iterating between steps 3 and 4 until no subgraph contains weights higher than this threshold.

### 3.2.3 Results and discussion

We present in this section results obtained on the Berkeley Segmentation Dataset (BSDS500) with the proposed merging approach. Starting from a superpixel partition with roughly 500 superpixels, our objective is to reduce the number of superpixels to around  $60 - 80$  by merging them. The oversegmentation that results from this process contains a “reasonable” number of segments and can serve as a solid foundation for implementing a classification algorithm depending on higher-level features to accomplish the segmentation.

## Experiments

Our proposed merging method is agnostic to the choice of superpixel generation algorithm. In our experiments, we started from an image partition containing  $K = 500$  superpixels computed with the fast marching based algorithm described in Chapter ??, and we used this initial partition to construct a region adjacency graph (RAG) on the image. The merging procedure was completed in two steps. The first step allows to reduce the number of superpixels from  $N = 500$  to  $N = 100 - 200$ . After the first step, the weights of the RAG are updated and a second merging procedure is conducted in order to obtain an oversegmentation with  $N = 50 - 100$  regions.

**Dissimilarity measure** The edges of the RAG must carry a dissimilarity measure constructed through Eq. (3.24) from the probability that the adjacent regions associated with the edge belong to the same segment. To compute the dissimilarity measure, we learned the similarity measure between regions by using a regression algorithm, which takes as input features extracted from the pair of adjacent superpixels and returns a score that can

be interpreted as the probability of merging each pair of adjacent regions. These features incorporate in particular various color and texture distances between the adjacent superpixels and information on the gradient strength at the boundary separating the superpixels. We refer the reader interested by additional details on the selected features to the manuscript [Chang, 2019].

To train the classifier, we use Berkeley Segmentation Dataset 500 (BSDS500) [Martin et al., 2001] in the following manner. For each training image in the BSDS500, we dispose of  $K$  distinct manual segmentation. Let  $\mathcal{T}^k := (T_i^k)_{i=1,\dots,K_k}$  be the  $k$ -th segmentation mask in the ground truth, which contains  $K_k$  segments. We can associate each superpixel  $\mathcal{S} := (S_i)_{i=1,\dots,N}$  to the region  $\mathcal{T}^k = (T_i^k)_{i=1,\dots,K_k}$  that it intersects the most:

$$A_i^k = \arg \max_{j=1,\dots,K_n} \mathcal{A}(S_i \cap T_j^k), \quad (3.26)$$

where  $\mathcal{A}(S_i \cap T_j^k)$  is the area of the intersection and  $A_i^k$  denotes the index of the region associated with  $S_i$  in the  $k$ -th manual segmentation. For a given edge  $(S_i, S_j)$  of the RAG, we define the target similarity measure  $\hat{w}_{ij}$  to be:

$$\hat{w}_{ij} = \exp \left( -\frac{1}{K} \sum_{k=1}^K \mathbf{1}_{\{A_i^k = A_j^k\}} \right).$$

## Results and discussion

To evaluate the performance of our algorithm, we compared it to a classical approach for performing graph clustering, the normalized cut algorithm (Ncut) [Shi and Malik, 2000]. In addition to classical metrics including boundary recall and precision, we also report the results in terms of the segmentation covering metrics. Segmentation covering provides a measures of the average matching between a segmentation and a given ground truth. It is defined by

$$SC(S, S_g) = \sum_{s_i \in S} \frac{|s_i|}{|\mathcal{P}|} \max_{s_j \in S_g} \frac{|s_i \cap s_j|}{|s_i \cup s_j|}. \quad (3.27)$$

In this expression,  $S$  and  $S_g$  are the segmentation and the ground truth segmentation, respectively.  $\mathcal{P}$  is the set of pixels, so that  $|\mathcal{P}|$  corresponds to the total number of pixels in the image. The segmentation covering metric computes, for each segment  $s_i \in S$ , the area of the largest intersection over

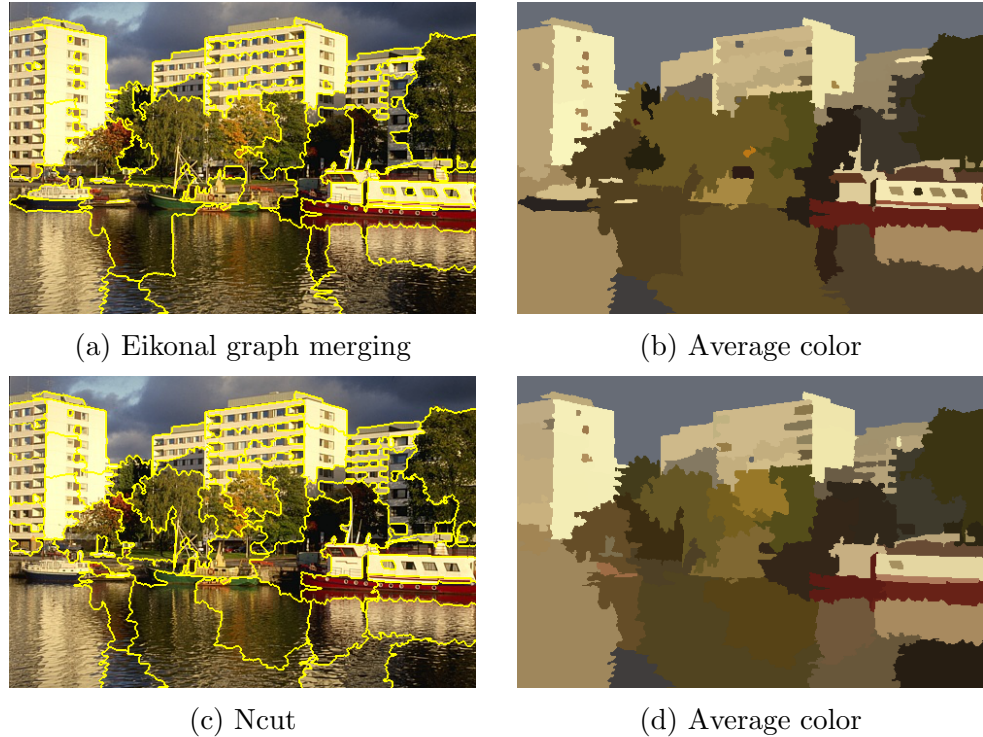


Figure 3.3: Segmentation results obtained with the Eikonal and normalized cut algorithms. The boundary recall are 0.64 and 0.63, respectively and the boundary precision are 0.33 and 0.29. The final partition comprises 70 segments [Chang, 2019].

union with the corresponding ground truth segment  $s_j$ . The calculation is weighted by the number of pixels within segment  $s_i$  and normalized by the total number of pixels in the image. The maximum possible value 1 can be achieved when  $S$  is identical with  $S_g$ .

The results obtained with our merging approach are provided in Tab. 3.1. We display one example of obtained segmentation in Fig. 3.3. Overall, we can note that the results obtained with the Eikonal equation on graphs are better than the ones obtained with the normalized cut. In particular, the Eikonal based approach brings significant improvement over the normalized cut algorithm with respect to the boundary precision and to the segmentation covering metrics. In our experiment, we opted for the second stopping criterion for the Eikonal algorithm, which consists in specifying a probabil-

ity threshold  $t$  and in iterating between the last two steps of the algorithm until no cluster contains weights higher than  $t$ . A drawback of this approach is that it makes it difficult to control the number of segments obtained at the end of the procedure. Hence, to facilitate the comparison between the Eikonal and Ncut approaches, for each image, we computed the normalized cut segmentation with the same number of segments as the one yielded by the Eikonal algorithm.

	Eikonal	NCut
Boundary recall	$0.76 \pm 0.09$	$0.74 \pm 0.08$
Boundary precision	$0.36 \pm 0.12$	$0.31 \pm 0.11$
Seg. covering	$0.32 \pm 0.12$	$0.23 \pm 0.09$
Number of segments	$66 \pm 10$	$63 \pm 9$

Table 3.1: Results of the Eikonal and of the normalized cut algorithm on the test images of the BSD.

It is interesting to discuss in greater detail the stopping criterion used for Eikonal algorithm, in particular the choice of the threshold  $t$ . This threshold can indeed be fixed in an adaptative manner depending on the set of weights as observed on the adjacency graph. In our experiments, we followed the following procedure to select the threshold value:

1. Sort the edges increasingly according to their weight.
2. Arbitrarily select a proportion of edges considered to be actual contours, and set the corresponding weight as threshold.

Another interesting thing to notice is that in spite of the refinement step, the obtained segmentation depends on the initial choice of germs. Due to the initial random selection of germs, certain areas of the image may become artificially over-segmented. To address this issue and minimize the impact of the initial seed selection, a straightforward post-processing operation can be performed at the conclusion of the algorithm. This operation involves extracting the highest merging probability observed at the boundaries between adjacent regions, thereby establishing a dissimilarity measure between these regions. Subsequently, the pairs of regions are sorted in ascending order based on their dissimilarity values. As the algorithm progresses, pairs of adjacent regions are evaluated, and if their dissimilarity falls below a specified

threshold for the refinement step, they are merged together. It is important to note that each region can only be merged once during this process to prevent the creation of adjacency graph regions with edges exceeding the threshold weight. By implementing this post-processing step, the number of clustered regions can be effectively reduced, while the overall quality of the segmentation is only minimally affected. This post-processing was applied in our experiment, which explains why the number of segments obtained with the Eikonal based algorithm and the normalized cut are slightly different in Tab. 3.1.

### 3.2.4 Conclusion

In this chapter, we presented a novel algorithm that performs region merging on the superpixel segmentation of an image. This algorithm is based upon a region adjacency graph representation of the superpixel partition. Each edge in the graph corresponds to a pair of adjacent superpixels and carries a weight accounting for the dissimilarity between these superpixels. The algorithm uses a generalization of the Eikonal equation to the framework of graphs to perform the graph clustering, an idea originally introduced by [Buyssens et al., 2014c]. During Kaiwen Chang’s PhD thesis, our main contribution was to propose to learn the weights of the graph based on annotated data. We evaluated the performance of our Eikonal-based approach by comparing it to a classical graph clustering algorithm, namely the normalized cut [Shi and Malik, 2000]. Our results demonstrated improvements over the classical algorithm, particularly in terms of segmentation covering and boundary precision metrics.

The initial goal of the algorithm was to process images from experiments in materials science. For these images, it is difficult to obtain annotated training data, and therefore it is crucial to develop segmentation algorithms requiring a low number of data to be trained. So far, our merging algorithm has only been applied to perform the segmentation of natural images taken from the Berkeley Segmentation Dataset. Hence, an obvious short term perspective of the work presented in this chapter would be to evaluate it on images obtained during physics experiments. We expect these images to be more homogeneous in terms of content than natural images, so that they might require a lower amount of training example to be segmented using a supervised approach.

# Bibliography

- Radhakrishna Achanta and Sabine Susstrunk. Superpixels and Polygons Using Simple Non-iterative Clustering. In *2017 IEEE Conference on Computer Vision and Pattern Recognition (CVPR)*, pages 4895–4904, Honolulu, HI, July 2017. IEEE. ISBN 978-1-5386-0457-1.
- Radhakrishna Achanta, Appu Shaji, Kevin Smith, Aurelien Lucchi, Pascal Fua, and Sabine Süsstrunk. Slic superpixels compared to state-of-the-art superpixel methods. *IEEE transactions on pattern analysis and machine intelligence*, 34(11):2274–2282, 2012.
- H. Altendorf and D. Jeulin. Random-walk-based stochastic modeling of three-dimensional fiber systems. *Physical Review E*, 83(4):041804, 2011.
- O. Amsellem, K. Madi, F. Borit, D. Jeulin, V. Guipont, M. Jeandin, E. Boller, and F. Pauchet. Two-dimensional (2d) and three-dimensional (3d) analyses of plasma-sprayed alumina microstructures for finite-element simulation of young’s modulus. *Journal of Materials Science*, 43(12):4091–4098, 2008.
- Christophe Andrieu, Nando De Freitas, Arnaud Doucet, and Michael I Jordan. An introduction to mcmc for machine learning. *Machine learning*, 50:5–43, 2003.
- Pablo Arbelaez, Michael Maire, Charless Fowlkes, and Jitendra Malik. Contour detection and hierarchical image segmentation. *IEEE Trans. Pattern Anal. Mach. Intell.*, 33(5):898–916, May 2011.
- M. Avrami. Kinetics of phase change. I. general theory. *The Journal of Chemical Physics*, 7(12):1103–1112, 1939.

- F. Baccelli and B. Blaszczyzyn. *Stochastic Geometry and Wireless Networks: Volume 1: THEORY*, volume 1. Now Publishers Inc, 2009.
- S. Beauvais, V. Guipont, M. Jeandin, D. Jeulin, A. Robisson, and R. Saenger. Study of the porosity in plasma-sprayed alumina through an innovative three-dimensional simulation of the coating buildup. *Metallurgical and Materials Transactions A*, 39(11):2711–2724, 2008.
- S. Beucher and Ch. Lantuéjoul. Use of watersheds in contour detection. In *International workshop on image processing, real-time edge and motion detection*, 1979.
- Serge Beucher and Fernand Meyer. The morphological approach to segmentation: the watershed transformation. *Optical Engineering-New York-Marcel Dekker Incorporated-*, 34:433–433, 1992.
- Vincent Bortolussi, Bruno Figliuzzi, François Willot, Matthieu Faessel, and Michel Jeandin. Morphological modeling of cold spray coatings. *Image Analysis & Stereology*, 37(2):145–158, 2018.
- Vincent Bortolussi, Bruno Figliuzzi, François Willot, Matthieu Faessel, and Michel Jeandin. Electrical conductivity of metal–polymer cold spray composite coatings onto carbon fiber-reinforced polymer. *Journal of Thermal Spray Technology*, 29:642–656, 2020.
- Pierre Buyssens, Isabelle Gardin, and Su Ruan. Eikonal based region growing for superpixels generation: Application to semi-supervised real time organ segmentation in CT images. *IRBM*, 35(1):20–26, December 2014a.
- Pierre Buyssens, Isabelle Gardin, Su Ruan, and Abderrahim Elmoataz. Eikonal-based region growing for efficient clustering. *Image and Vision Computing*, 32(12):1045–1054, December 2014b. ISSN 0262-8856.
- Pierre Buyssens, Matthieu Toutain, Abderrahim Elmoataz, and Olivier Lézoray. Eikonal-based vertices growing and iterative seeding for efficient graph-based segmentation. In *IEEE International Conference on Image Processing (ICIP 2014)*, page 5 pp., Paris, France, October 2014c.
- V. Capasso. *Mathematical Modelling for Polymer Processing: Polymerization, Crystallization, Manufacturing*, volume 2. Springer, 2003.

Pierre Cettour-Janet, Clément Cazorla, Vaïa Machairas, Quentin Delannoy, Nathalie Bednarek, François Rousseau, Etienne Decencière, and Nicolas Passat. Watervoxels. *Image Processing On Line IPOL*, 9:317–328, 2019.

Kaiwen Chang. *Machine learning for image segmentation*. PhD thesis, Université Paris sciences et lettres, 2019.

Kaiwen Chang and Bruno Figliuzzi. Fast marching based superpixels generation. In *Mathematical Morphology and Its Applications to Signal and Image Processing: 14th International Symposium, ISMM 2019, Saarbrücken, Germany, July 8-10, 2019, Proceedings 14*, pages 350–361. Springer, 2019.

Kaiwen Chang and Bruno Figliuzzi. Fast marching based superpixels. *Mathematical Morphology-Theory and Applications*, 4(1):127–142, 2020.

S. N. Chiu, D. Stoyan, W. S. Kendall, and J. Mecke. *Stochastic geometry and its applications*. John Wiley & Sons, 2013.

Dorin Comaniciu and Peter Meer. Mean shift: A robust approach toward feature space analysis. *IEEE Transactions on pattern analysis and machine intelligence*, 24(5):603–619, 2002.

Eva Dejnozková and Petr Dokládal. A parallel algorithm for solving the eikonal equation. In *2003 IEEE International Conference on Acoustics, Speech, and Signal Processing, 2003. Proceedings.(ICASSP'03)., volume 3*, pages III–325. IEEE, 2003.

F. Delloro, M. Faessel, H. Proudhon, D. Jeulin, M. Jeandin, E. Meillot, and L. Bianchi. A morphological approach to the modeling of the cold spray process. In *ITSC 2014*, pages 221–226. DVS, 2014.

Matthieu Faessel and Dominique Jeulin. 3d multiscale vectorial simulations of random models. In *International Congress of Stereology*, 2011.

Pedro F Felzenszwalb and Daniel P Huttenlocher. Efficient graph-based image segmentation. *International journal of computer vision*, 59(2):167–181, 2004.

Bruno Figliuzzi. Eikonal-based models of random tessellations. *Image Analysis & Stereology*, 38(1):15–23, 2019.

- Bruno Figliuzzi, WHR Chan, CR Buie, and JL Moran. Nonlinear electrophoresis in the presence of dielectric decrement. *Physical Review E*, 94(2):023115, 2016.
- Bruno Figliuzzi, Kaiwen Chang, and Matthieu Faessel. Hierarchical segmentation based upon multi-resolution approximations and the watershed transform. In *International Symposium on Mathematical Morphology and Its Applications to Signal and Image Processing*, pages 185–195. Springer, 2017.
- Bruno Figliuzzi, Antoine Montaux-Lambert, François Willot, Grégoire Naudin, Pierre Dupuis, Bernard Querleux, and Etienne Huguet. A bayesian approach to morphological models characterization. *Image Analysis & Stereology*, 40(3):171–180, 2021.
- Brian Fulkerson, Andrea Vedaldi, and Stefano Soatto. Class segmentation and object localization with superpixel neighborhoods. In *Computer Vision, 2009 IEEE 12th International Conference on*, pages 670–677. IEEE, 2009.
- E. N. Gilbert. Random subdivisions of space into crystals. *The Annals of mathematical statistics*, pages 958–972, 1962.
- Rémi Giraud, Vinh-Thong Ta, Nicolas Papadakis, and Yannick Berthoumieu. Texture-aware superpixel segmentation. In *2019 IEEE International Conference on Image Processing (ICIP)*, pages 1465–1469. IEEE, 2019.
- P. Hall. *Introduction to the theory of coverage processes*, volume 188. Wiley New York, 1988.
- H Hermann. Stochastic models of heterogeneous materials. In *Materials science forum*. Trans Tech Publications, 1991.
- Anil K Jain and Farshid Farrokhnia. Unsupervised texture segmentation using gabor filters. *Pattern recognition*, 24(12):1167–1186, 1991.
- A. Jean, D. Jeulin, S. Forest, S. Cantournet, and F. N’Guyen. A multiscale microstructure model of carbon black distribution in rubber. *Journal of microscopy*, 241(3):243–260, 2011.

- D. Jeulin. Morphology and effective properties of multi-scale random sets: A review. *Comptes Rendus Mécanique*, 340(4):219–229, 2012.
- D. Jeulin and M. Moreaud. Percolation of multi-scale fiber aggregates. In *S4G, 6th International Conference Stereology, Spatial Statistics and Stochastic Geometry. Prague*, pages 26–29, 2006.
- D. Jeulin, P. Monnaie, and F. Péronnet. Gypsum morphological analysis and modeling. *Cement and Concrete Composites*, 23(2):299–311, 2001.
- Dominique Jeulin. *Morphological models of random structures*, volume 447. Springer, 2021a.
- Dominique Jeulin. *Morphological models of random structures*. Springer, 2021b.
- W. A. Johnson and R. F. Mehl. Reaction kinetics in processes of nucleation and growth. *Trans. Aime*, 135(8):396–415, 1939.
- Alex Levinstein, Adrian Stere, Kiriakos N Kutulakos, David J Fleet, Sven J Dickinson, and Kaleem Siddiqi. Turbopixels: Fast superpixels using geometric flows. *IEEE transactions on pattern analysis and machine intelligence*, 31(12):2290–2297, 2009.
- Zhengqin Li and Jiansheng Chen. Superpixel segmentation using Linear Spectral Clustering. In *2015 IEEE Conference on Computer Vision and Pattern Recognition (CVPR)*, pages 1356–1363, June 2015.
- André Liebscher and Claudia Redenbach. Statistical analysis of the local strut thickness of open cell foams. *Image Analysis & Stereology*, 32(1):1–12, 2013.
- Vaïa Machairas, Matthieu Faessel, David Cárdenas-Peña, Théodore Chabardes, Thomas Walter, and Etienne Decencière. Waterpixels. *IEEE Transactions on Image Processing*, 24(11):3707–3716, 2015.
- Jitendra Malik, Serge Belongie, Thomas Leung, and Jianbo Shi. Contour and texture analysis for image segmentation. *International journal of computer vision*, 43(1):7–27, 2001.

- Ravi Malladi, James A Sethian, and Baba C Vemuri. Shape modeling with front propagation: A level set approach. *IEEE transactions on pattern analysis and machine intelligence*, 17(2):158–175, 1995.
- David Martin, Charless Fowlkes, Doron Tal, and Jitendra Malik. A database of human segmented natural images and its application to evaluating segmentation algorithms and measuring ecological statistics. In *Proceedings Eighth IEEE International Conference on Computer Vision. ICCV 2001*, volume 2, pages 416–423. IEEE, 2001.
- G. Matheron. *Random sets and integral geometry*, volume 1. Wiley New York, 1975.
- J. Mecke. Palm methods for stationary random mosaics. *Combinatorial principles in stochastic geometry*, pages 124–132, 1980.
- J. Mecke. Inequalities for the anisotropic poisson polytope. *Advances in applied probability*, pages 56–62, 1995.
- Fernand Meyer and Serge Beucher. Morphological segmentation. *Journal of visual communication and image representation*, 1(1):21–46, 1990.
- R. E. Miles. The random division of space. *Advances in applied probability*, pages 243–266, 1972.
- R. E. Miles. Estimating aggregate and overall characteristics from thick sections by transmission microscopy. *Journal of Microscopy*, 107(3):227–233, 1976.
- I. S. Molchanov. Statistics of the boolean model: from the estimation of means to the estimation of distributions. *Advances in applied probability*, pages 63–86, 1995.
- J. Møller. Random tessellations in  $\mathbb{R}^d$ . *Advances in Applied Probability*, pages 37–73, 1989.
- J. Møller. Random johnson-mehl tessellations. *Advances in applied probability*, pages 814–844, 1992.
- Jesper Møller. *Lectures on random Voronoi tessellations*. Springer, 1994.

- Maxime Moreaud, Dominique Jeulin, Vincent Morard, and Renaud Revel. Tem image analysis and modelling: application to boehmite nanoparticles. *Journal of microscopy*, 245(2):186–199, 2012.
- Joachim Ohser and Katja Schladitz. *3D images of materials structures: processing and analysis*. John Wiley & Sons, 2009.
- Ch. Peyrega, D. Jeulin, Ch. Delisée, and J. Malvestio. 3d morphological modelling of a random fibrous network. *Image Analysis & Stereology*, 28(3):129–141, 2011.
- J.-L. Quenech, M. Coster, J.-L. Chermant, and D. Jeulin. Study of the liquid-phase sintering process by probabilistic models: Application to the coarsening of WC-Co cermets. *Journal of Microscopy*, 168(1):3–14, 1992.
- Claudia Redenbach. Microstructure models for cellular materials. *Computational Materials Science*, 44(4):1397–1407, 2009.
- Claudia Redenbach and Irene Vecchio. Statistical analysis and stochastic modelling of fibre composites. *Composites Science and Technology*, 71(2):107–112, 2011.
- Christian P Robert, George Casella, and George Casella. *Monte Carlo statistical methods*, volume 2. Springer, 1999.
- L. A. Santaló. Integral geometry and geometric probability. 1976.
- Alexander Schick, Mika Fischer, and Rainer Stiefelhagen. Measuring and evaluating the compactness of superpixels. In *Proceedings of the 21st international conference on pattern recognition (ICPR2012)*, pages 930–934. IEEE, 2012.
- R. Schneider and W. Weil. *Stochastic and integral geometry*. Springer, 2008.
- J. Serra. *Image analysis and mathematical morphology*. Academic press, 1982.
- James A Sethian. A fast marching level set method for monotonically advancing fronts. *Proceedings of the National Academy of Sciences*, 93(4):1591–1595, 1996.

- James A Sethian. Fast marching methods. *SIAM review*, 41(2):199–235, 1999.
- Jianbo Shi and Jitendra Malik. Normalized cuts and image segmentation. *IEEE Transactions on pattern analysis and machine intelligence*, 22(8):888–905, 2000.
- David Stutz, Alexander Hermans, and Bastian Leibe. Superpixels: An evaluation of the state-of-the-art. *Computer Vision and Image Understanding*, 166:1–27, 2018.
- S. Torquato. *Random heterogeneous materials: microstructure and macroscopic properties*, volume 16. Springer, 2002.
- John E Vargas-Muñoz, Ananda S Chowdhury, Eduardo B Alexandre, Felipe L Galvão, Paulo A Vechiatto Miranda, and Alexandre X Falcão. An iterative spanning forest framework for superpixel segmentation. *IEEE Transactions on Image Processing*, 28(7):3477–3489, 2019.
- Luc Vincent and Pierre Soille. Watersheds in digital spaces: an efficient algorithm based on immersion simulations. *IEEE Transactions on Pattern Analysis & Machine Intelligence*, 13(06):583–598, 1991.
- Haisheng Wang, Andrea Pietrasanta, Dominique Jeulin, François Willot, Matthieu Faessel, Loïc Sorbier, and Maxime Moreaud. Modelling mesoporous alumina microstructure with 3d random models of platelets. *Journal of microscopy*, 260(3):287–301, 2015.
- Haisheng Wang, François Willot, Maxime Moreaud, Mickaël Rivallan, Loïc Sorbier, and Dominique Jeulin. Numerical simulation of hindered diffusion in  $\gamma$ -alumina catalyst supports. *Oil & Gas Science and Technology–Revue d'IFP Energies nouvelles*, 72(2):8, 2017.
- Haisheng Wang, Dominique Jeulin, François Willot, Loïc Sorbier, and Maxime Moreaud. Modelling of the microstructure of mesoporous alumina constrained by morphological simulation of nitrogen porosimetry. *Colloids and Surfaces A: Physicochemical and Engineering Aspects*, 553:378–396, 2018.
- W. Weil and J. A. Wieacker. Densities for stationary random sets and point processes. *Advances in applied probability*, pages 324–346, 1984.

C Lawrence Zitnick and Sing Bing Kang. Stereo for image-based rendering using image over-segmentation. *International Journal of Computer Vision*, 75(1):49–65, 2007.